UNIVERSITY OF CALIFORNIA, SAN DIEGO

Crustal and Uppermost Mantle Structure beneath the Western United States from USArray Regional Phase Analysis

A dissertation submitted in partial satisfaction of the
requirements for the degree
Doctor of Philosophy

in

Earth Sciences

by

Janine Sylvia Buehler

Committee in charge:

Peter M. Shearer, Chair
Luciana Astiz
William Coles
Bruce Cornuelle
Yuri Fialko
T. Guy Masters

2013

The dissertation of Janine Sylvia Buehler is approved, and it is acceptable in quality and form for publication on microfilm and electronically:

_____

_____

_____

_____

_____

_____
Chair

University of California, San Diego

2013

TABLE OF CONTENTS

LIST OF FIGURES

LIST OF TABLES

ACKNOWLEDGEMENTS

My deepest debt is to my advisor, Peter Shearer, who has always been supportive and encouraging, who let me work independently but guided me back on track whenever I got lost in details, who taught me that simple is often better than complicated, and who understands the need to escape to the mountains every so often.

I am also grateful for the support and interest of my committee: Luciana Astiz, Bill Coles, Bruce Cornuelle, Yuri Fialko, and Guy Masters. I would like to especially thank Yuri for advising me in my first quarter at IGPP, and Luciana, for her friendship and contagious enthusiasm, all her help with the antelope system, and the many Thanksgiving dinners.

A huge thanks to Frank Vernon and his team at the Array Network Facility for making data access a breeze.

Thank you, my fellow first year students, for your camaraderie and for your broad advice on topics ranging from science to the American way of life: Andy Barbour, Xiaowei Chen, Brendan Crowell, Scott DeWolf, Ashlee Henig, and Xiaopeng Tong. I am especially thankful for the friendships of Ashlee and Xiaowei. Thank you, Ashlee, for proofreading documents, for improving my English language skills, for remembering things I would chronically forget, and for continually inviting me even though I am often not the most social. Many thanks, Xiaowei, for your enthusiasm no matter what, for your help with fortran coding, and for introducing me to the traditions of China.

Over the last few years I had the privilege to share my office with Valerie Sahakian and Samer Naif, two great officemates! Valerie is the best companion and training-partner one could wish for, always enthusiastic no matter how crazy the plan... even if the plan involves running for three hours at 5am or offwidth climbing! I will never forget our trip to Catalina Island to run a Marathon on my 30th birthday. Thank you! I also owe many thanks to Samer, whose unconventional (but fruitful!) approaches to science and relaxation have been quite inspiring, and who, most importantly, introduced me to the no-knead bread. I've been baking it ever since.

It is almost impossible to express my gratitude for the never-ending support and encouragement from my parents, Silvia and Beat Buehler, and my sister Michelle. I am also very thankful for the friendship of Doris Randa, even if most of the time there is an ocean between us. Big thanks to Jake and Charlie for making sure, every day, that I get up at a reasonable time, and for teaching me that it does not take much to be happy

(a couple of boxes and some love). My sincere appreciation to Led Zeppelin for making enough good music for six years of mainly desk work. Finally, thank you, Daniel, for not only exploring the valleys and crests of the High Sierra with me, but also the highs and lows, and everything in between, of life.

Chapter 2, in full, is a reprint of the material as it appears in Buehler, J. S. and P. M. Shearer, Pn tomography of the western United States using USArray, Journal of Geophysical Research: Solid Earth, 115(B9), 2010. Chapter 3, in full, is a reprint of the material as it appears in Buehler, J. S. and P. M. Shearer, Localized imaging of the uppermost mantle with USArray Pn data, Journal of Geophysical Research: Solid Earth, 117(B9), 2012. Chapter 4, in full, is in revision for publication in Geophysical Research Letters: Buehler, J. S. and P. M. Shearer, Sn propagation in the western United States from common mid-point stacks of USArray data, Geophysical Research Letters, in review, 2013. Chapter 5, in full, has been submitted for publication in Journal of Geophysical Research: Buehler, J. S. and P. M. Shearer, Anisotropy and Vp/Vs in the uppermost mantle beneath the western United States from joint analysis of Pn and Sn phases, Journal of Geophysical Research, submitted, 2013. The dissertation author was the primary investigator and author of these papers.

VITA

2013	Doctor of Philosophy in Earth Sciences, University of California, San Diego
2007-2013	Research Assistant, University of California, San Diego
2007	Master of Science in Earth Sciences, ETH Zuerich, Switzerland

PUBLICATIONS

Buehler, J. S. and Shearer, P. M. (2013), Anisotropy and Vp/Vs in the uppermost mantle beneath the western United States from joint analysis of Pn and Sn phases, *Journal of Geophysical Research: Solid Earth*, submitted.

Buehler, J. S. and Shearer, P. M. (2013), Sn propagation in the western United States from common mid-point stacks of USArray data, *Geophysical Research Letters*, in revision.

Buehler J. S. and Shearer, P. M. (2012), Localized imaging of the uppermost mantle with USArray Pn data, *Journal of Geophysical Research: Solid Earth*, 117(B09305).

Buehler J. S. and Shearer, P. M. (2010), Pn tomography of the western United States using USArray, *Journal of Geophysical Research: Solid Earth*, 115(B09315).

Buehler, J. S. (2007), Source-modeling of the 2003 Bam earthquake using multiple data sets, Master Thesis, ETH Zuerich.

ABSTRACT OF THE DISSERTATION

Crustal and Uppermost Mantle Structure beneath the Western United States from USArray Regional Phase Analysis

by

Janine Sylvia Buehler

Doctor of Philosophy in Earth Sciences

University of California, San Diego, 2013

Peter M. Shearer, Chair

The aim of this dissertation is to improve our understanding of the crust and uppermost mantle structure in the western United States, profiting from the wealth of regional phase data recorded at USArray stations. USArray, a transportable seismic array of ∼400 seismometers, has greatly increased seismic data coverage across the United States in the past few years, and allows imaging of the lithosphere of the North American continent with better resolution and new methods. The regional phases are often challenging to analyze, especially in a tectonically-active region like the western United States, because of their sensitivities to the heterogeneities of the crust and uppermost mantle. However, knowledge of the seismic structure of the lithosphere is not only essential in order to accurately image the velocity structure at greater depths, but also for constraining geodynamic models that reconstruct the tectonic evolution

of the continent, and hence the information that is carried by the regional phases is very valuable. The data set used in this study consists mostly of the regional seismic phases Pn and Sn, which propagate horizontally along the Moho in the mantle lid and constrain the seismic velocity structure at a confined depth. We applied traditional tomographic methods that profit from the improved ray coverage through USArray, but also employed array-based techniques that take advantage of the regular station spacing of the transportable array and don't depend on regularization. In addition, we used stacking methods to image the propagation efficiency of the Sn phase, which is often highly attenuated in tectonically active regions, on a regional scale. The results complement other seismic studies that average over greater depth intervals, such as surface- and body-wave tomographies and anisotropy analysis from shear-wave splitting, to provide information on temperature, composition, and tectonic processes at depth. Comparisons between Pn azimuthal anisotropy and fast polarization direction from shear wave splitting suggest significant vertical changes in anisotropy in several regions of the upper mantle beneath the western United States. Sn can in theory further constrain the nature of anisotropy in the mantle lid. However, we have so far been unable to resolve shear-wave splitting directly in the Sn waveforms as the phase is often attenuated and difficult to detect. Still, we obtained evidence for Sn propagation in several regions of the western United States such as the central Great Basin and the northeastern part of the Colorado Plateau. We found that there are enough quality Sn picks for joint Pn-Sn tomography and identified prominent Vp/Vs anomalies, such as large high Vp/Vs regions — typically associated with partial melt — below the Snake River Plain and the Colorado Plateau.

Chapter 1

Introduction

The goal of seismology is to study the interior of the Earth, and to continue where the geologist stops; it has in modern seismographs a sort of binoculars that enables us to look into the largest of depths.

Andrija Mohorovičić

Andrija Mohorovičić discovered the crust-mantle boundary more than a century ago by analyzing seismograms of the Kupa Valley earthquake of October 8, 1909. Ninety years later, plans for USArray, a dense network of transportable seismic stations and part of the appropriately named *Earthscope* project (http://www.earthscope.org, last accessed July 2013) were finalized for deployment beginning in early 2004. One of the major aims of *Earthscope* is to improve our knowledge of the seismic structure of the lithosphere and mantle below North America in order to gain a better understanding of the tectonic history of the continent.

USArray was just getting into full swing when I started my doctoral studies in 2007. All of the over 400 transportable stations were deployed in the western United States, and the westernmost stations were set to roll on and be deployed at the eastern margin of the array footprint (Figure 1.1). USArray has ∼70 km station spacing, and a station typically occupies a site for about two years, before it is moved from the westernmost to the easternmost margin of the station footprint in leapfrog fashion. It was expected that the first stations would reach the east coast by 2013 (and they did). The transportable array not only provides a tremendous amount of data, but the improved instrumentation also allows for the development of innovative processing methods that

can address some of the shortcomings of traditional methods. By 2007, there was already a wealth of data accumulated from the past three years, and geophysicists were in high spirits about the prospect of obtaining better-resolved images of the North American lithosphere and upper mantle. This made for a great opportunity, as in subsequent years many researchers would produce and publish seismic models from various data sets and methods with different strengths and weaknesses, which facilitated detailed comparisons of the seismic structure of the crust and mantle.

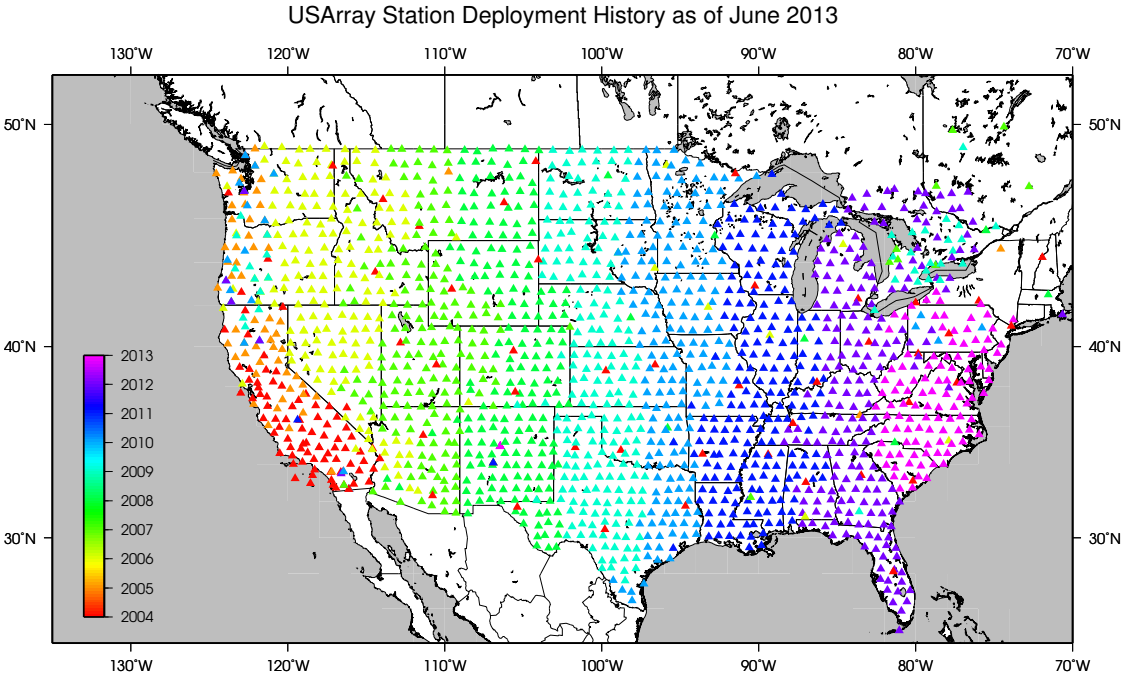

Figure 1.1: USArray station (triangles) deployment history.

The North American continent has a tectonically active and complex western margin as a result of past and present subduction of oceanic lithosphere under the North American plate. This includes past subduction of the Farallon slab, until the approaching spreading ridge from the west was pulled into the subduction zone, establishing a transform regime between the North American and Pacific plate along the coast of California ∼30 Ma years ago (e.g., *Atwater* [1970]), and ongoing subduction of the Juan de Fuca Plate under the North American Plate in the north at the Cascadia subduction zone (Figure 1.2). During the subduction of the Farallon Plate, the Sierra Nevada batholith was formed below the volcanic arc roughly 150 to 80 million years ago (e.g., *Ducea* [2001]). It is generally believed that subsequent flattening of the subduction angle caused the

mountain building further inland during the Laramide orogeny (e.g., *Humphreys* [2009]). The Colorado Plateau, located in the southwest United States, has been puzzling to scientists for decades because of its high elevation but undeformed crust, despite the fact that its neighboring provinces went through periods of extensive deformation. The Basin and Range province is situated between the Colorado Plateau and Sierra Nevada range, and is characterized by an extensional tectonic regime and north-south trending mountain ranges and valleys. The cause of the extension is still under debate; explanations include mantle upwellings as a result of the past subduction at the western margin (e.g., *Liu and Shen* [1998]). The northern Basin and Range borders on the Snake River Plain, a large tectonic graben with smooth topography. The eastern part of the Snake River Plain is parallel to the west-southwest motion of the North American plate, and is marked by sequential caldera-forming eruptions while the plate moved over the Yellowstone hotspot. The Yellowstone caldera, located at the eastern end of the Snake River Plain, marks the current location of the Yellowstone hotspot.

Present day topography, surface geology, and geophysical measurements all provide clues for tectonic evolution and processes at depth. However, our understanding of the tectonic history of the Earth has been much improved by tomographic images of the present-day seismic velocity structure at depth. These images can act as data, among other constraints, such as present day plate motion and topography, for geodynamicists to model tectonic evolution (*Liu et al.* [2008]). Interpretation of seismic tomography maps is often challenging, however, not only because seismic velocities depend on a number of factors, including temperature, composition, and the presence of melt or water (e.g., *Goes et al.* [2000], *Perry et al.* [2006]), but also because the various seismic data sets have different sensitivities and resolution, both vertical and lateral. In addition, crustal variations often have strong effects on teleseismic body waves, which can introduce errors if they are not accounted for in upper mantle studies (e.g., *Waldhauser et al.* [2002]). It is therefore of interest to have accurate seismic models of the crust and mantle lid from regional phase data, which are confined in depth and complement surface-wave and teleseismic body-wave analysis.

USArray provides a wealth of regional seismic phases from earthquakes and quarry blasts, which allow imaging of crust and upper-mantle structure in detail and with a leap in resolution in regions outside of areas with small and local station arrays, such as California. Regional phases include crustal refractions and reflections, but also the

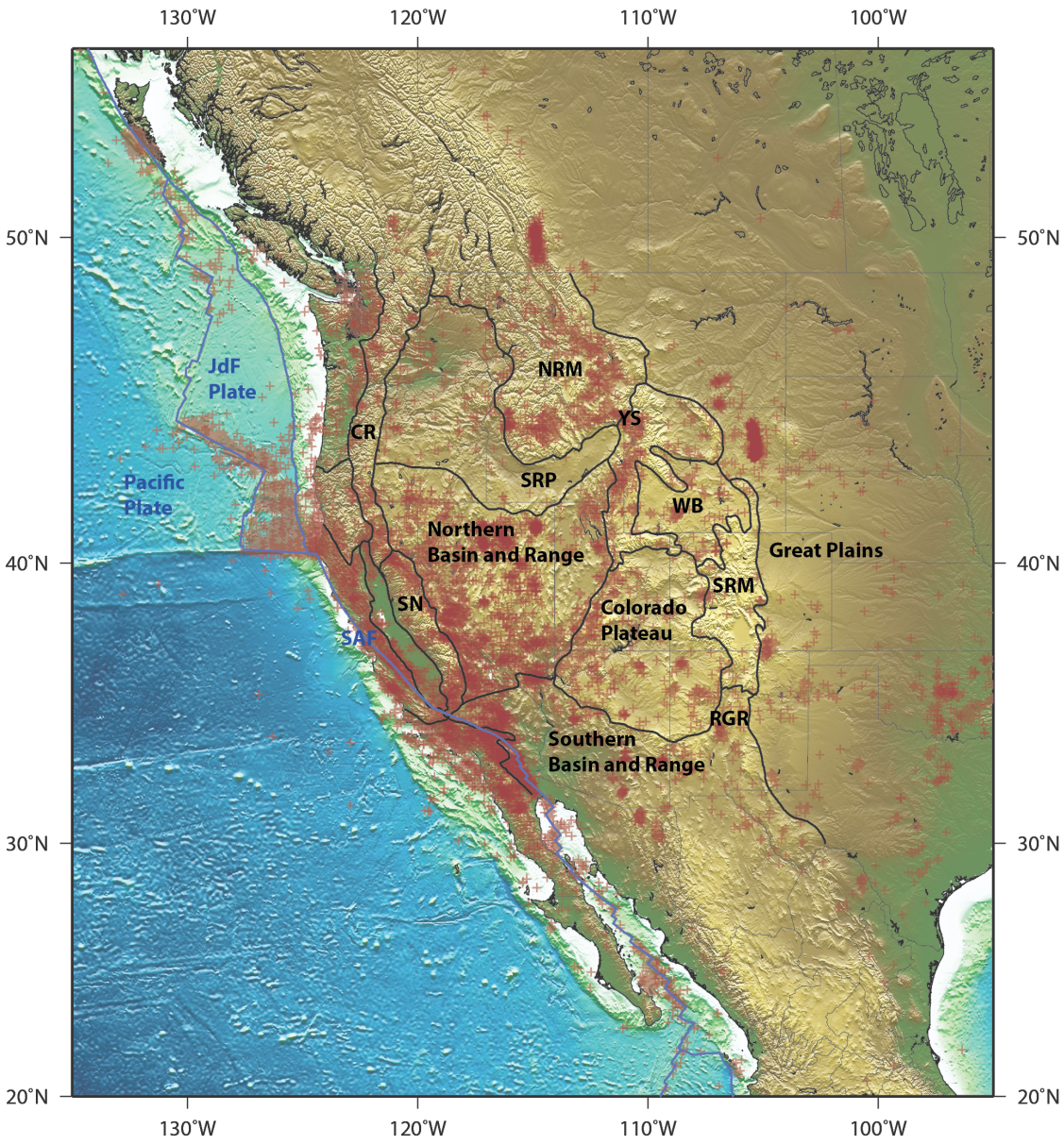

Figure 1.2: Topographic map of the western United States with some of the physiographic provinces indicated by black lines and names. The abbreviations are in place for the Cascade Range (CR), Sierra Nevada (SN), Mojave (M), Snake River Plain (SRP), Northern Rocky Mountains (NRM), Yellow Stone (YS), Wyoming Basin (WB), Southern Rocky Mountains (SRM), and Rio Grande Rift (RGR). The Plate boundaries are indicated with blue lines, and the abbreviations in blue are in place for the Juan de Fuca (JdF) plate and the San Andreas fault (SAF). The events and quarry blasts in the regions are marked with red pluses.

refracted waves that travel along the Mohorovičić–discontinuity, usually abbreviated as

Moho. The seismic velocities increase sharply at the Moho because of the change from crustal material, consisting of a variety of rocks, to mantle material, mainly composed of dense peridotites. These Moho-refracted waves, which propagate in the faster uppermost mantle material, are generally identified as Pn and Sn, and are the first-arriving P- and S-waves at regional distances beyond about ∼200 km, depending on crustal thickness and the velocity structure. Since they travel horizontally in the uppermost mantle, they provide a large amount of information about the seismic structure within a very confined depth. The vertical limitation of regional phase tomography can be turned into an advantage if the results are compared to models with poorer vertical resolution because they provide effective depth constraints. It is therefore of interest to compare Pn and Sn velocity maps to tomography results from teleseismic body-wave and surface-wave data to assess the vertical extent and variability of the seismic anomalies.

The upper-mantle peridotites, whose dominant mineral is olivine, are seismically anisotropic. Seismic anisotropy manifests itself in seismic velocities that vary with direction of propagation. This can, for example, be achieved simply by layering of different isotropic materials for sufficiently large wavelengths. Such anisotropy by layering is often observed in the crust. However, in the mantle anisotropy is believed to be mostly caused by lattice-preferred alignment of olivine crystals (e.g. *Christensen* [1984], *Maupin and Park* [2007]). Observations show that olivine in plastically deformed aggregates tends to align its a-axis parallel to the flow line (e.g., *Babuska and Cara* [1991]), therefore anisotropy in sub-lithospheric mantle and in sub-crustal lithosphere under oceans is generally associated with mantle flow. The anisotropy observations of the continental mantle-lid are often not straightforward to interpret because of complex tectonic evolution. Still, knowledge of the anisotropic signal of the lithosphere is important, as the most popular methods used to infer mantle anisotropic structure, such as the splitting of SKS phases or surface-wave measurements, average over large depth intervals. In order to infer that an anisotropic pattern from such measurements is indeed caused by the mantle flow, as it is generally believed to be the case for the strikingly cylindrical SKS fast polarization directions in the western United States, one needs to know the contribution to the signal from the lithosphere. The Pn and Sn phases can provide information on anisotropy in the mantle lid, and differences between Pn or Sn fast axis and SKS fast polarization directions suggest a mantle origin of the latter signal. In addition, knowing the depth extent of anisotropy allows for comparisons with model predictions from the

flow velocity fields and lithospheric strain fields of geodynamic models.

The outline of my dissertation is as follows: In Chapter 2 we performed traditional Pn tomography of the western United States based on a previous study by *Hearn* [1996]. USArray provides a significant increase in data, and we could image the seismic velocity structure and anisotropy just below the Moho with better resolution. We found that the Pn fast axes indicate anisotropy that is different from that inferred from SKS fast polarization directions, which suggests that the latter is caused by sub-lithospheric anisotropy in the upper mantle. We then used the same Pn data set for the study in Chapter 3, but applied array methods that solve for the velocity and azimuth of the incoming wavefronts at local sub-arrays. These methods have the advantage that they don't rely on regularization as applied in regular travel-time tomography, and potentially reveal the amplitude of the seismic anomalies with greater accuracy. Next we focused on the Sn phase. Since a previous study found that Sn does not propagate in the majority of the western United States (*Beghoul et al.* [1993]) and we had trouble accurately picking the Sn arrivals in many seismograms, we first applied a common mid-point stacking analysis to identify the highly attenuating regions in the uppermost mantle below the western United States. The results of this study are presented in Chapter 4. Finally, in Chapter 5 we combined the Pn and Sn data sets for a joint analysis. The resulting P-to-S velocity ratio maps provide further insight into the nature of the seismic anomalies, since P- and S-wave generally have different sensitivities to the parameters that influence seismic velocities. Since Pn and Sn waves also have a crustal leg, we obtained additional constraints on crustal thickness and velocity structure.

References

Atwater, T. (1970), Implications of plate tectonics for the Cenozoic tectonic evolution of western North America, *Geological Society of America Bulletin*, *81*(12), 3513–3536.

Babuska, V., and M. Cara (1991), *Seismic anisotropy in the Earth*, vol. 10, Springer.

Beghoul, N., M. Barazangi, and B. L. Isacks (1993), Lithospheric structure of Tibet and western North America: Mechanisms of uplift and a comparative study, *J. Geophys. Res.*, *98*(B2), 1997–2016.

Christensen, N. I. (1984), The magnitude, symmetry and origin of upper mantle anisotropy based on fabric analyses of ultramafic tectonites, *Geophysical Journal Of The Royal Astronomical Society*, *76*(1), 89–111.

Ducea, M. (2001), The California arc: Thick granitic batholiths, eclogitic residues, lithospheric-scale thrusting, and magmatic flare-ups, *GSA today*, *11*(11), 4–10.

Goes, S., R. Govers, and P. Vacher (2000), Shallow mantle temperatures under Europe from P and S wave tomography, *J. Geophys. Res.*, *105*(B5), 11,153–11,169.

Hearn, T. M. (1996), Anisotropic Pn tomography in the western United States, *Journal Of Geophysical Research-Solid Earth*, *101*(B4), 8403–8414.

Humphreys, E. (2009), Relation of flat subduction to magmatism and deformation in the western United States, *Backbone of the Americas: Shallow subduction, plateau uplift, and ridge and terrane collision*, *204*, 85.

Liu, L., S. Spasojevic, and M. Gurnis (2008), Reconstructing Farallon Plate Subduction Beneath North America Back to the Late Cretaceous, *Science*, *322*(5903), 934–938, doi:10.1126/science.1162921.

Liu, M., and Y. Shen (1998), Sierra Nevada uplift: A ductile link to mantle upwelling under the Basin and Range province, *Geology*, *26*(4), 299–302.

Maupin, V., and J. Park (2007), Theory and observations–wave propagation in anisotropic media, *Seismology and the Structure of the Earth. Treatise on Geophysics*, *1*, 289–321.

Perry, H. K. C., C. Jaupart, J. C. Mareschal, and N. M. Shapiro (2006), Upper mantle velocity-temperature conversion and composition determined from seismic refraction and heat flow, *Journal of Geophysical Research-Part B-Solid Earth*, p. 14 pp.

Waldhauser, F., R. Lippitsch, E. Kissling, and J. Ansorge (2002), High–resolution teleseismic tomography of upper–mantle structure using an a priori three–dimensional crustal model, *Geophysical Journal International*, *150*(2), 403–414.

Chapter 2

Pn tomography of the western United States using USArray

USArray has now provided several years of high-quality seismic data and improved ray coverage for much of the western United States, which will enable increased resolution for studies of the lithospheric and deeper structure of the North American continent. Here we analyze Pn arrival times from the transportable stations of USArray to resolve crustal thickness and uppermost-mantle structure. We use 123,008 Pn picks from April 2004 to October 2009 as measured by the Array Network Facility (ANF) at epicentral distances from 180 to 1450 km. These picks are derived from 778 stations at ∼70 km spacing and 7903 earthquakes and quarry blasts. Applying the classic time-term method, we use a regularized least-squares inversion to estimate crustal thickness variations and image velocity perturbations in the uppermost mantle just below the Moho. We also consider upper-mantle anisotropy and describe the velocity perturbations with a $\cos 2\phi$ azimuthal variation. Our crustal thickness map generally agrees with receiver function results from other researchers but differs in some details. We obtain an average upper-mantle velocity of 7.93 km/s, with higher velocities beneath eastern Washington and northern Idaho, and lower velocities near the California-Mexico border, the Sierra Nevada, the northern coastal California region, and the greater Yellowstone area. We observe large anisotropic anomalies in southern California as well as in the Snake River Plain area. These results should complement other seismic studies (e.g., body and surface-wave tomography, shear-wave splitting, etc.) to provide information about composition, temperature, and tectonic processes in the western United States.

2.1 Introduction

Seismic tomography has the potential to provide detailed images of Earth structure, but is often limited by the coverage of the available seismic data. The USArray with its very dense and almost uniformly spaced stations has greatly improved tomographic resolution for much of the western United States. Prior to the installation of USArray in 2004, ray coverage was only dense in areas with regional seismic networks, as in California where many instruments are deployed along the San Andreas fault and various other seismogenic zones, whereas ray density was greatly reduced and non-uniform outside these areas. Many studies of Moho depth variations or upper-mantle seismic velocities focused therefore on local areas with high station densities, as for example southern California [e.g. *Hearn*, 1984; *Zhu and Kanamori*, 2000].

Pn tomography reveals information about the seismic velocities and anisotropy in the uppermost mantle as well as crustal thickness. Because of the large contrast in seismic velocities between the lower crust and the upper mantle and the shallow velocity gradient in the upper mantle, Pn tomographic velocity perturbation images show results for a very confined depth in the uppermost mantle, complementing surface-wave or other body-wave tomographies that average anomalies over larger depth intervals. Lateral variations in Pn velocities can be associated with temperature differences in the upper mantle, as well as compositional differences [e.g., *Goes and van der Lee*, 2002; *Perry et al.*, 2006].

The crustal structure of the the western United States is complex due to the very active tectonic regime. Crustal thickness and mantle anisotropy are fundamental in understanding tectonic history [*Savage and Silver*, 1993; *Silver*, 1996; *Zandt et al.*, 2004]. Therefore, isotropic as well as anisotropic velocity perturbations in the uppermost mantle below the western United States have been of interest and several Pn studies have been published [*Beghoul and Barazangi*, 1990; *Hearn et al.*, 1991; *Hearn*, 1996]. Alternative methods have also been applied to obtain information on crustal thickness and velocity structures in the upper mantle, which will provide points of comparison to our Pn results. Crustal thickness estimates have been obtained from surface waveform fitting [*Das and Nolet*, 1998], receiver function analysis [*Lewis et al.*, 2000; *Zhu and Kanamori*, 2000; *Yan and Clayton*, 2007; *Gashawbeza et al.*, 2008], and gravity data [*Mooney and Weaver*, 1989]. Anisotropy in the upper mantle has mostly been studied with shear wave splitting [*Polet and Kanamori*, 2002; *Currie et al.*, 2004; *West et al.*,

2009]. In addition, improved seismic instrumentation has led to the development of new methods to extract information about the structure of the crust and uppermost mantle, for example using ambient noise tomography [*Yang et al.*, 2008; *Lin et al.*, 2009].

This study is similiar in approach to *Hearn* [1996], who performed anisotropic Pn tomography for the western United States, but benefits from a much more extensive data set. We determine both isotropic and anisotropic velocity perturbations in the uppermost mantle as well as crustal thickness using the densely spaced USArray stations. We start with several data processing steps to avoid using falsely identified Pn arrivals, and then use the Pn times to invert for velocity perturbations and crustal thickness. We also assess model resolution using various synthetic data sets. Finally, we discuss our results and compare them to other studies available in this area. Our results provide well-resolved Pn tomographic images that complement other seismic studies.

2.2 Data

In this study we use first-arrival picks provided by the USArray Network Facility (*ANF* [2009]). USArray consists of 400 transportable broadband seismometers, which are gradually crossing the United States, occupying sites for about two years on a 70-km grid. We use 778 station locations from -124.6° E to -100.1° E and from 29.5° N to 49.1° N, and events from -130° E to -100° E and from 25° N to 55° N (Figure 2.1a). In total we have 611,817 P-wave arrivals (128,328 of which are labelled Pn) with epicentral distances smaller than 2000 km recorded between April 2004 and October 2009 (Figure 2.1b).

Pn arrivals

In theory, Pn is the head wave that travels along the Moho within the uppermost mantle layer with an average velocity of about 8 km/s. However, in practice the complexity of the very heterogeneous crustal layer and the presence of velocity gradients beneath the Moho often make it difficult to distinguish the shallow turning P-wave arrivals from the refracted Pn-wave arrivals. Therefore, for certain picks the Pn label may not be correct, and we apply several processing steps to provide more reliable Pn picks. First we eliminate all the picks that are clearly not first arrivals. Next, we proceed in an iterative way similar to *Hearn et al.* [1991] and apply a number of constraints to the data: (1) epicentral distance between 180 km and 1450 km, (2) maximum hypocenter depth of 35 km, (3) maximum residual of 6 s after a straight line fit, (4) every event recorded by at

least 5 stations, and (5) every station recorded Pn picks from at least 5 events. We limit the maximum distance to 1450 km since the residuals of the initial model form a straight line up to this distance on a residual-distance plot (Figure 2.1e), but start to curve at longer ranges. After the iterative windowing procedure, the final data set consists of 123,008 Pn picks (65,299 with label Pn) from 7903 events (Figure 2.1c). The group of early arrivals seen in the plot results mainly from offshore events (Figure 2.1a,d) because of a thinner crust and/or higher velocities.

Ray density is the highest in California because of its many seismically active areas. Lower ray coverage is observed in parts of the Basin and Range area and the Columbia River Plateau as well as east of -114°E (Figure 2.2a). Good azimuthal coverage for a large part of the western United States allows us to resolve azimuthal anisotropy (Figure 2.2b).

2.3 Method

One-dimensional modelling

To obtain an initial estimate of the slowness in the uppermost mantle as well as crustal thickness variations we set up a linear least squares problem following *Hearn* [1984]. If there is no significant vertical velocity gradient below the Moho, the Pn travel time can be described with three terms:

$$t_{es} = \tau_e + \tau_s + \Delta_{es} S, \tag{2.1}$$

where Δ_{es} is the great circle distance between the source and the receiver, S is the slowness in the uppermost mantle, and τ_e and τ_s are the event and station time terms, respectively. Crustal thicknesses are usually estimated from the station time terms only because of the relatively large uncertainties in hypocenter depth and earthquake origin time, which are absorbed into the event time terms [*Hearn*, 1984]. In the presence of a significant vertical velocity gradient in the uppermost mantle, additional terms would be needed to account for the fact that the arrivals are actually turning waves below the Moho [*Zhao*, 1993; *Phillips et al.*, 2007].

The time term method of equation 2.1 achieves much better fits to our data than a simple straight line fit and can account for the travel-time differences between the offshore and continental earthquakes. The straight line fit gives a mean velocity of

8.09 km/s and a large mean squared error of 2.5 s^2. By using equation 2.1, the event time term corrects for the thinner oceanic crust and the mean squared error is reduced to 0.42 s^2. A straight line fit to just the continental earthquakes reveals about the same mean velocity of 7.93 km/s as the one-dimensional time term estimation using all the earthquakes.

Two-dimensional modeling

To include isotropic velocity perturbations as well as anisotropy, a two-dimensional grid is applied along the Moho and for each cell an isotropic as well as an anisotropic perturbation is taken into account [*Hearn*, 1996]. The Pn travel time residuals can then be described as:

$$\delta t_{es} = \delta\tau_e + \delta\tau_s + \Sigma\Delta_{esk}(\delta S_k + A_k \cos 2\phi_{esk} + B_k \sin 2\phi_{esk}), \tag{2.2}$$

where Δ_{esk} is the distance the ray travels in the cell k, A_k and B_k are the anisotropic parameters for cell k, and ϕ is the back azimuth. We do not take the entire station-receiver distance into account, but only the distance the ray actually travels along the uppermost mantle. The horizontal offsets between the mantle piercing points and station locations are a function of Pn velocity, crustal velocity, and Moho depth, none of which are known a priori. The station and event time correction terms absorb errors in mantle pierce point location estimates as well as uncertainties in event location and origin time. Note that we neglect any possible 4ϕ azimuthal variations because previous studies of mantle anisotropy and models of aligned olivine crystals have generally found the 2ϕ terms to dominate [e.g. *Raitt et al.*, 1969; *Christensen*, 1984]. We solve the resulting problem $d = Gm$ in a least squares sense, where d is the data, m is the model, and G contains the kernels from Equation 2.2. We simultaneously minimize the data misfit, model norm and model roughness:

$$\text{Minimize} \quad \|d - Gm\|^2 + \lambda_1\|m\|^2 + \lambda_2\|Lm\|^2, \tag{2.3}$$

where L is the finite difference approximation of the Laplacian and λ_1 and λ_2 are the regularization parameters.

USArray data modeling approach

We start with the time term method and a uniform Pn velocity (Equation 2.1). This problem has 8682 model parameters and is small enough to permit a noniterative

least squares inversion to solve for the slowness, station and event time terms. We apply no regularization to the time terms. Once we obtain a first-order estimate of the Moho topography and the mean upper-mantle velocity, we estimate the location of the mantle pierce points, assuming the ray obeys Snell's law and a constant crustal velocity of 6.3 km/s. To image velocity perturbations and anisotropy, we then apply a regularized least squares inversion (Equation 2.3) using a conjugate gradient least squares approach [e.g., *Aster et al.*, 2005] to the travel time residuals (Equation 2.2, with a cell size of 0.25° by 0.25°). We run these inversions for several different regularization parameters to obtain trade-off curves. We use separate parameters for the isotropic and the anisotropic regularization terms respectively as well as for smoothing and damping (four regularization parameters in total). In practice, we seem to obtain the best results in terms of error and resolution trade-off for roughly equal damping and smoothing for the anisotropic and isotropic parameters. The station and event corrections are neither damped nor smoothed.

2.4 Results

Synthetic Data Resolution Tests

To address the question of whether our ray coverage is sufficient for the methods applied, it would be ideal to apply a singular value decomposition and directly obtain resolution matrices [e.g., *Aster et al.*, 2005]. However, the large size of the problem makes it difficult to compute the generalized inverse. Therefore we use the classical checkerboard model approach to estimate the resolution and reliability of the inversion results.

We calculate synthetic travel times using the same station-event configuration as in the inversions with real data. We generate several synthetic data sets resulting from checkerboard perturbations with different sizes and amplitudes. The anomalies in Figure 2.3 are 2° by 2° (8 by 8 model cells) and have a mean slowness of 0.125 s/km. We compute synthetic travel times resulting from either isotropic or anisotropic velocity variations only, and also from combined isotropic and anisotropic perturbations. This procedure allows to assess the resolution of the specific model parameters as well as the leakage of isotropic into anisotropic perturbations and vice versa [*Hearn*, 1996, 1999].

Figure 2.3a shows the model obtained for synthetic travel times generated with isotropic perturbations only. The perturbations vary ±5% in adjacent cells. Random

noise with a standard deviation of 0.5 s is added. Figure 2.3b shows the leakage into anisotropic parameters, which is large at the corner of adjacent cells where the change in perturbations is the largest. This indicates that the anisotropic results may be less reliable in areas with sharp velocity contrasts. The amount of leakage depends on the choice of regularization parameters, here equal damping and smoothing is applied to all the parameters.

Figure 2.4a shows the model obtained for synthetic travel times with anisotropic perturbations only. The data are generated assuming perpendicular fast directions in adjacent cells on a two degree grid. Generally, the fast axis is well resolved. The amplitude of the leakage into isotropic perturbations is small and shows a random pattern (Figure 2.4b).

With the method described in the previous section (Equations 2.1 and 2.2), we obtain one delay time term per station. This term represents the average delay time over a cone defined by the ray incident angle and Moho depth. For this theory to be adequate, the Moho has to be fairly flat under a station. If the Moho topography has significant slopes, better accuracy would be obtained by allowing the station delay times to vary with azimuth. We tested the validity of the single time term assumption by generating a synthetic Moho topography and calculating synthetic travel times that consider the slopes in computing the mantle pierce points. To simplify the ray path calculations, we approximated the slope with a series of steps and assumed that the ray travels horizontally along the Moho in the vicinity of a station. The results show that crustal thicknesses can be resolved with reasonable accuracy using inversions that do not explicitly account for this effect. In addition, real data residual versus azimuth plots for USArray stations do not indicate significant slopes in the Moho topography. Finally, simple calculations of the effect of the inferred slopes reveal a negligible change in travel times if they are taken into account. Therefore the single station-term method seems to be justified.

USArray Data

Figure 2.5 shows the final model for the isotropic velocity perturbations resulting from the combined iso-anisotropic inversion (Equation 2.2). The mean squared residual resulting from this model is 0.34 s^2. The locations of the major anomalies correlate well with known active processes, as for example the large low velocity anomalies in the Snake River Plain leading to the Yellowstone hotspot. Similar to *Hearn et al.* [1991], the main

anomaly is not at the location of the Yellowstone caldera, but below the Snake River Plain. This could partly be because of the ray coverage gap at the current location of the caldera. In our image the lowest velocity occurs west of Hearn et al.'s main anomaly, in the area of the western Snake River Plain/Owyhee plateau. The amplitudes of the anomalies in the east might change with the advance of the transportable array since the synthetic test yields lower amplitudes close to the eastern model boundary where the data become more sparse.

In agreement with *Hearn et al.* [1991] and *Hearn* [1996], a large low velocity anomaly is also observed below the Sierra Nevada. The slow anomaly could either be caused by a mountain root or by warmer temperatures and partial melt beneath the mountain belt or a combination of both. The larger delay times in the Sierra seem to favor the mountain root theory. In southern California we obtain a large low velocity zone west of the Salton Sea similar to *Hearn* [1984] and *Sung and Jackson* [1992], surrounded by less pronounced high velocity perturbation areas.

There is a significant high velocity region in the north, spanning eastern Washington, northern Idaho and western Montana. This high velocity zone is bounded to the south by the low velocity region of the Snake River Plain but continues to the east with its highest velocities in southwestern Wyoming. High resolution three-dimensional P-wave tomography using USArray data shows that some of these fast anomalies can be observed to a depth of about 400 km [*Roth et al.*, 2008; *Burdick et al.*, 2008, 2009] and can be associated with the western edge of Precambrian North America.

The velocity variations obtained from a purely isotropic model (no azimuth dependent parameters included in the inversion) show similar patterns as the anomalies obtained from the combined inversion (Figure 2.6). The main difference is the higher amplitudes observed in Figure 2.6, however the locations of the anomalies are stable. The mean squared residual of this model is 0.36 s^2.

The Pn anisotropic modeling results generally show a quite complex image. We obtain large anisotropic anomalies in the Great Basin desert, off the coast of northern California as well as in southern California/northern Mexico (Figure 2.7). In central California, the fast axis is mostly fault-parallel, indicating that the anisotropy is caused by shearing along the plate boundary. Similar to *Hearn* [1996] we find that the fast axis is not parallel to the plate boundary in all of southern California, but that the fast direction orients east-west, especially in the Mojave Desert. *Hearn* [1996] discusses the possibility

of the north-south compression in southern California as the cause of the perpendicular east-west anisotropic direction.

We find a fairly homogeneous northeast fast axis in the northwestern Basin and Range, which then turns into a rotational feature in eastern Nevada. In the southern Basin and Range the fast direction orients southeast-northwest. Off coastal Oregon there is strong east-west anisotropy, which could be correlated with the subduction zone. However, large isotropic anomalies can also be observed in this area, which could indicate a modeling artifact since azimuthal coverage in these cells is limited.

The station terms account for the time it takes the ray to travel from the mantle pierce point to the receiver. Positive station time terms indicate a thicker crust, however there is a tradeoff between contributions from low velocity anomalies in the crust and deeper Moho depths. Nevertheless, the larger the delay is, the more likely it has some significant contributions from Moho depth deviations. We use an average crustal velocity of 6.3 km/s to estimate absolute Moho depths. Several large delays can be observed, i.e., in areas where a compensating root is expected, as in the Sierra Nevada as well as the Cascade Range (Figure 2.8). This is in agreement with the slow velocity anomalies observed below this entire mountain chain (Figure 2.5). The thickest crust is imaged in southern Wyoming, however in this part of the model the resolution is reduced.

In the northern Basin and Range province (Nevada and part of Utah) crustal thickness is reduced as expected in an extensional tectonic regime. The crust is also thinner below the coastal ranges of California and below much of southern California. The thinner crust in the southern Basin and Range is very distinct, with thicker crust indicated to the north below the Colorado Plateau. Similar crustal thicknesses can be observed from surface waveform fitting [*Das and Nolet*, 1998].

In addition to Pn studies, receiver function analyses are widely used to estimate crustal thickness. With receiver functions a crustal thickness estimate is obtained below every station considered, due to P to S wave conversions at the crust-mantle boundary. Many such studies exist, especially for the area of the Basin and Range and southern California [*Lewis et al.*, 2000; *Zhu and Kanamori*, 2000; *Yan and Clayton*, 2007]. *Gilbert and Sheehan* [2004] estimate crustal thickness across the Great Basin, Colorado Plateau, Rocky Mountain, and the great Plains Provinces. Similar to our results, *Gilbert and Sheehan* [2004] find that the crust thins in the Basin and Range. Their thinnest crust is confined to northern Nevada and northern Utah, but we also find crust with similar

thinness in central western Utah. Both the results of *Gilbert and Sheehan* [2004] and our station term results indicate thicker crust below the Rocky Mountains. However, they have their thickest crust in northwestern Colorado whereas our Pn study images its thickest crust in southern Wyoming.

Receiver functions from USArray (A. Levander, personal communication, 2009) agree with our station delays at large scale. The receiver function results show a somewhat greater average Moho depth of 38 km in the western United States compared to the average crustal thickness determined by the station terms (34 km). This discrepancy is likely caused by differences in the assumed crustal velocity structure used in each method to compute the Moho depths. With the time term method we solve for relative station terms, measure the intersect time of a straight line fit to data from continental earthquakes, and compute the mean Moho depth assuming an average crustal P-wave velocity of 6.3 km/s. However, using a crustal velocity of 6.58 km/s would increase our mean Moho depth estimate to 38 km, in agreement with the receiver function analysis. Further analysis will be required to determine which absolute Moho depth estimate is more accurate. Here we focus simply on comparing relative Moho depths. Using the Pn depths obtained using the higher crustal velocity, 65% of the receiver function thickness estimates are within ± 5 km of the Pn results and only 12% of the results have a larger difference then 10 km. Consistent with the Pn results, the USArray receiver function analyses show that the southern Basin and Range province has relatively thin crust versus thicker crust observed beneath the southwestern Colorado Plateau. In addition, the Pn and receiver function results both show thicker crust in the Sierra Nevada as well as the Cascade Range, and a thin crust in the eastern Great Basin. The main differences are that receiver functions show thinner crust in a wider band along most of the west coast and up to ∼20 km thicker crust in eastern Montana. The estimates in the east will likely become more accurate for USArray studies with the advance of the temporary stations.

2.5 Discussion and Conclusions

Many mantle velocity and crustal thickness studies in the western United States provide an opportunity to compare results. Because Pn is sensitive to only a small depth interval at the very top of the mantle, it provides an important constraint on other methods, which vertically average features in the upper mantle. With USArray, we expect to obtain more detailed Pn velocity maps than previous studies. Applying the data

selection process described in *Hearn* [1996] to our data set, USArray still provides more than twice the number of picks for the same area as previous studies, with improved ray coverage at varying angles, which is important to produce accurate azimuthal anisotropy maps.

Azimuthal anisotropy in the upper mantle can be estimated using several different data sets, such as surface waves and Pn and SKS arrivals. With shear wave splitting measurements, usually from the SKS phase, anisotropy below individual stations can be determined. Both shear wave splitting and surface wave results provide a vertically integrated measure of anisotropy in the upper mantle whereas the Pn results constrain the anisotropy in the uppermost mantle lid. Differences in anisotropy between shear wave splitting and Pn studies can therefore indicate vertical changes in anisotropy.

The most pronounced feature of recent USArray shear-wave splitting studies is the small splitting times in the central Great Basin, surrounded by fast polarization directions in a cylindrical pattern (*Liu* [2009]; *West et al.* [2009], Figure 2.9). In addition, new high resolution P-wave tomographic models using USArray of the same area reveal a near vertical cylindrical zone of increased P-wave velocities [*Roth et al.*, 2008; *West et al.*, 2009], ranging from a depth of about 75 km to at least 500 km. *Burdick et al.* [2008, 2009] use USArray P-wave arrivals combined with P-wave travel times from other sources, such as reprocessed ISC data, to constrain 3-D heterogeneity in the upper mantle beneath North America. *Burdick et al.* [2009] also observe a deep fast anomaly below central Nevada, but which only appears below about 200 km. The location of this high velocity anomaly coincides with the region of smallest splitting times. *West et al.* [2009] suggest that a lithospheric drip beneath the central Great Basin causes these seismic observations, i.e., that the downward flow generates a shift from azimuthal to radial anisotropy. This circular pattern of fast polarization directions centered in the eastern Great Basin has been noted before at lower resolution and alternate models were proposed to explain this feature; *Savage and Sheehan* [2000]'s preferred model consists of vertically upwelling asthenospheric material beneath the northern Great Basin in combination with lateral asthenospheric flow because of lithospheric drag parallel to the absolute plate motion. *Zandt and Humphreys* [2008] propose that a simple rollback of a narrow slab can predict this circular SKS pattern and argue that there is no evidence for an active plume beneath central Nevada; they suggest that the combination of westward slab rollback of the Gorda-Juan de Fuca slab and northward opening of the slab window promotes a

strong toroidal mantle flow.

The Pn tomography plot (Figure 2.7) also shows an area of almost no anisotropy in central Nevada, however of much less spacial extent than in the shear wave splitting. Pn results also suggest that the fast axis rotates around the anisotropy low, however this pattern is less smooth and distinct compared to the fast polarization direction of the vertically traveling shear waves. In contrast to the P-wave tomography [*West et al.*, 2009], Pn isotropic velocity anomalies indicate no significant fast structures in the central Great Basin (Figure 2.5). The imaged Pn anisotropy variations by *Hearn* [1996] show a similar low in the central Great Basin, but with strong northwest oriented anisotropy in the southeast.

Lin et al. [2009] apply a new surface wave tomographic method based on tracking wave fronts across the USArray using ambient noise recordings. Their 24 s period Rayleigh wave azimuthal anisotropy maps reveal similar fast directions as the Pn model. The extent of the low anisotropy area is also much smaller in the central Great Basin than for the shear wave splitting results, and, similar to our model, stronger northeast-southwest anisotropy can be observed in northwestern Nevada. All three methods agree on east-west fast directions north of the Great Basin. Similar to the Pn velocity perturbations, the 24 s Rayleigh isotropic phase speed shows a more diffuse low-velocity anomaly in the central Great Basin. The surface-wave and Pn anisotropy models are in better general agreement with each other than they are with the splitting results, which include sensitivity to anisotropy deeper in the mantle. These different results indicate that there is not a consistent vertically-coherent mechanism that generates anisotropy throughout the upper mantle. The less pronounced features of the Pn study suggest that the shear wave splitting observations result mostly from sub-lithospheric mantle flow although anisotropy in the lithosphere might contribute to the circular pattern.

North of the Great Basin and in the backarc of the Juan the Fuca subduction zone are the Columbia River Basalts, the High Lava Plains in Oregon, and the Yellowstone-Snake River Plain volcanic system. The eastern Snake River Plain is topographically depressed and its volcanism tracks approximately parallel to the motion of the North American plate. The Plain exhibits age progression in volcanism originating from northern Nevada and extending towards the current location of the Yellowstone caldera [*Christiansen et al.*, 2002].

Studies of shear wave splitting in the eastern Snake River Plain [e.g., *Schutt*

et al., 1998; *Waite et al.*, 2005] imply a relatively simple anisotropic structure. The fast directions (∼N60°E) are roughly parallel to the absolute plate motion and can be explained with asthenospheric flow. However, the fast directions rotate from ∼N60°E to ∼N100°E in the central Snake River Plain and then back to N70°E in the western Snake River Plain [*Walker et al.*, 2004]. These variations can not be explained with a simple asthenospheric flow model; instead they can be recognized as part of the rotation around the Great Basin. Following *Savage and Sheehan* [2000], *Walker et al.* [2004] propose a similar parabolic flow model which expands upon the simpler model by adding an upwelling effect in central Nevada.

Similar to the splitting results, the Pn fast axes from this study rotate from SW-NE in the western Snake River Plain to ESE-WNW directions in the central Snake River Plain. However the Pn fast axes do not rotate back in the eastern Snake River Plain except in the northeastermost part, but keep the same ESE-WNW to E-W orientation. A lower resolution Pn study by *Smith and Ekstrom* [1999] confirms mostly E-W orientation fast axes beneath the eastern Snake River Plain. This supports the assumption that the SKS fast polarization directions in the eastern Snake River Plain are caused by plate motion parallel asthenospheric flow and that the strain field in the uppermost mantle is dominated by local processes.

In addition to the varying angles, the delay times on the eastern Snake River Plain are significantly smaller (∼1 s) than along its flanks (∼1.8 s) which is not predicted by either of the flow models. To explain these shorter delay times, *Walker et al.* [2004] present three hypothesis, one of them being lower crustal flow away from the eastern Snake River Plain, which would suggest a lattice preferred orientation of olivine in the uppermost mantle with a NNW-SSE fast direction below the plain. This hypothesis is not supported by the Pn anisotropy results, as the fast axes are primarily east-west oriented. Alternate explanations include the presence of magma-filled lenses in the lithosphere and compositional segregation.

Adjacent to the volcano track of the Snake River Plain, and originating at the same time at the Owyhee Plateau ∼15 Ma years ago, is the volcanism of the High Lava Plains [*Christiansen et al.*, 2002]. Although the common place of origin seems to suggest a common source, the volcano track of the Snake River Plain is roughly parallel to the motion of the North American plate whereas the High Lava Plain volcanic track heads almost in a perpendicular direction. Our Pn fast axes are not parallel to the volcanic

High Lava Plain track, but rotate from SW-NE fast directions in southern Oregon to E-W fast axes in central Oregon before they rotate back to a more plate-motion-parallel direction.

A recent shear wave splitting study of the High Lava Plain region by *Long et al.* [2009] that uses data recorded by USArray stations as well as temporary experiments shows fast polarization directions of the SKS phase that are nearly uniform E-W aligned. Contrary to these shear wave splitting results, which show larger splitting delay times in the High Lava Plains (>1.5 s) than in the eastern Snake River Plain (∼1–1.5 s), we observe much less Pn anisotropy in southeastern Oregon (∼0.5%) than in southern Idaho (∼2.5%). Synthetic tests show that the amplitude of Pn anisotropy is generally not well resolved north of 42°N. However since the magnitude and fast directions of the Pn and SKS anisotropy differ in eastern Oregon, it is probable that the largest contributions to the observed splitting parameters originate below the uppermost mantle lid and are most likely associated with mantle flow. This is consistent with the unusually large delay times that are observed in the High Lava Plains, which are more reasonable to explain with asthenospheric flow than with a very large magnitude of anisotropy in the lithosphere [*Long et al.*, 2009].

Ray coverage is reduced beneath the southern Rocky Mountains and the Colorado Plateau and we will be able to make more accurate comparisons once USArray moves further east. At current resolution, we obtain a significant low velocity anomaly beneath Arizona, which includes the region beneath the southwestern Colorado Plateau. Recent USArray P-wave tomography results show a similar slow anomaly at 100 km depth [*Burdick et al.*, 2009]. Similar to a local Pn study [*Lastowka and Sheehan*, 2005], we also find reduced velocities beneath the Rio Grande Rift. SKS splitting results across the Rio Grande Rift and the Colorado Plateau show fast directions that are generally uniform and sub-parallel to the North American plate motion [e.g., *Gok et al.*, 2003]. In contrast, the Pn fast axes show a complex picture for most of the southern Rocky Mountain region but are not yet completely reliable.

The complex tectonic setting in California is shown in many seismic anisotropy studies that investigate upper mantle dynamics [*Hearn*, 1984; *Sung and Jackson*, 1992; *Polet and Kanamori*, 2002; *Davis*, 2003]. In California, we observe mostly San Andreas fault parallel anisotropy, which turns into a more east-west orientation in the Mojave Desert and northern Mexico. The orientations of the fast axes are generally similar to

the ones previously obtained by *Hearn* [1996] and correspond with the surface wave tomography results at large scale [*Lin et al.*, 2009].

Polet and Kanamori [2002] determine anisotropy beneath California from shear-wave splitting measurements. Similar to our Pn anisotropy results (Figure 2.7), they find northeast oriented fast directions in northern California, a more NW-SE fast direction in central California, and E-W anisotropy in the Mojave. *Polet and Kanamori* [2002] find variations in splitting parameters with polarization azimuth for stations in the greater San Francisco Bay Area and are able to model these observations with a two-layer anisotropy model, in which a thin layer with a fast direction parallel to the San Andreas fault is above a layer with an E-W fast polarization direction. In apparent agreement with this two-layer model, the Pn fast axes in central California are mainly fault parallel aligned whereas the fast SKS polarization directions are rotated towards an E-W direction.

In Oregon, our Pn results indicate mostly east-west fast directions, which then rotate to a more NE-SW orientation in Washington. Generally the Pn anisotropy is less reliable for the area north of the Great Basin, since the azimuthal coverage is worse. Except for the large anisotropic perturbations off the coast of Oregon, the Pn results suggest very little anisotropy in the forearc of the Cascadia subduction zone. We consider the large perturbations off the coast of northern California and Oregon likely to be an inversion artifact because of reduced azimuthal ray coverage in this area. In contrast, shear wave splitting suggests fast directions parallel to the subduction direction of the Juan de Fuca plate for a large part of the forearc of the Cascadia subduction zone with delay times larger than one second [*Currie et al.*, 2004]. In the backarc, the Pn as well as the shear wave anisotropy show similar fast directions parallel to the convergence of the Pacific and North American plates.

Although anisotropy cannot be resolved equally well in the northwestern United States, USArray provides a greatly improved data set with good station and event coverage. Synthetic tests show that anomalies as small as 1° by 1° can be resolved for much of the western United States. Currently California and the Basin and Range areas are best resolved, however, as the transportable array moves east, resolution will improve east of the Great Basin. The Pn inversion results show prominent features of crustal thickness and velocity perturbations, many of which are observed throughout the region from studies using different data sets. The Pn anisotropy results are complementary to shear-wave splitting, suggesting in several regions that the orientation of azimuthal

anisotropy changes with depth in the uppermost mantle.

Acknowledgments

We thank Luciana Astiz and the operators of the Array Network Facility for making their phase picks available, and Thomas Hearn and an anonymous reviewer for their constructive comments. This research was funded by grant EAR-0710881 from the National Science Foundation. Chapter 2, in full, is a reprint of the material as it appears in Buehler, J. S. and P. M. Shearer, Pn tomography of the western United States using USArray, Journal of Geophysical Research: Solid Earth, 115(B9), 2010. The dissertation author was the primary investigator and author of this paper.

References

ANF (2009), http://anf.ucsd.edu/tools/events/download.php, *last accessed October 2009*.

Aster, R., B. Borchers, and C. Thurber (2005), *Parameter Estimation and Inverse Problems*, Elsevier Academic Press.

Beghoul, N., and M. Barazangi (1990), Azimuthal anisotropy of velocity in the mantle lid beneath the Basin and Range province, *Nature*, *348*(6301), 536–538.

Burdick, S., et al. (2008), Upper Mantle Heterogeneity beneath North America from Travel Time Tomography with Global and USArray Transportable Array Data, *Seismological Research Letters*, *79*(3), 384–392.

Burdick, S., R. D. van der Hilst, F. L. Vernon, V. Martynov, T. Cox, J. Eakins, T. Mulder, L. Astiz, and G. L. Pavlis (2009), Model Update December 2008: Upper Mantle Heterogeneity beneath North America from P-wave Travel Time Tomography with Global and USArray Transportable Array Data, *Seismological Research Letters*, *80*(4), 638–645.

Christensen, N. I. (1984), The magnitude, symmetry and origin of upper mantle anisotropy based on fabric analyses of ultramafic tectonites, *Geophysical Journal Of The Royal Astronomical Society*, *76*(1), 89–111.

Christiansen, R. L., G. R. Foulger, and J. R. Evans (2002), Upper-mantle origin of the Yellowstone hotspot, *Geological Society Of America Bulletin*, *114*(10), 1245–1256.

Currie, C. A., J. F. Cassidy, R. D. Hyndman, and M. G. Bostock (2004), Shear wave anisotropy beneath the Cascadia subduction zone and western North American craton, *Geophysical Journal International*, *157*(1), 341–353.

Das, T., and G. Nolet (1998), Crustal thickness map of the western United States by partitioned waveform inversion, *Journal Of Geophysical Research-Solid Earth*, *103*(B12), 30,021–30,038.

Davis, P. M. (2003), Azimuthal variation in seismic anisotropy of the southern California uppermost mantle, *Journal Of Geophysical Research-Solid Earth*, *108*(B1).

Gashawbeza, E. M., S. L. Klemperer, C. K. Wilson, and E. L. Miller (2008), Nature of the crust beneath northwest Basin and Range province from teleseismic receiver function data, *Journal Of Geophysical Research-Solid Earth*, *113*(B10).

Gilbert, H. J., and A. F. Sheehan (2004), Images of crustal variations in the intermountain west, *Journal Of Geophysical Research-Solid Earth*, *109*(B3).

Goes, S., and S. van der Lee (2002), Thermal structure of the North American uppermost mantle inferred from seismic tomography, *Journal Of Geophysical Research-Solid Earth*, *107*(B3).

Gok, R., et al. (2003), Shear wave splitting and mantle flow beneath LA RISTRA, *Geophysical Research Letters*, *30*(12).

Hearn, T., N. Beghoul, and M. Barazangi (1991), Tomography of the Western United-States From Regional Arrival Times, *Journal Of Geophysical Research-Solid Earth*, *96*(B10), 16,369–16,381.

Hearn, T. M. (1984), Pn Travel Times in Southern California, *Journal Of Geophysical Research*, *89*(NB3), 1843–1855.

Hearn, T. M. (1996), Anisotropic Pn tomography in the western United States, *Journal Of Geophysical Research-Solid Earth*, *101*(B4), 8403–8414.

Hearn, T. M. (1999), Uppermost mantle velocities and anisotropy beneath Europe, *Journal Of Geophysical Research-Solid Earth*, *104*(B7), 15,123–15,139.

Lastowka, L. A., and A. F. Sheehan (2005), CDROM Interstation Pn Study Along the Rio Grande Rift, *The Rocky Mountain Region: An Evolving Lithosphere - Geophysical Monograph Series 154*, pp. 379–384.

Lewis, J. L., S. M. Day, H. Magistrale, J. Eakins, and F. Vernon (2000), Regional crustal thickness variations of the Peninsular Ranges, southern California, *Geology*, *28*(4), 303–306.

Lin, F. C., M. H. Ritzwoller, and R. Snieder (2009), Eikonal tomography: surface wave tomography by phase front tracking across a regional broad-band seismic array, *Geophysical Journal International*, *177*(3), 1091–1110.

Liu, K. H. (2009), NA-SWS-1.1: A uniform database of teleseismic shear wave splitting measurements for North America, *Geochem. Geophys. Geosyst.*, *10*.

Long, M. D., H. Gao, A. Klaus, L. S. Wagner, M. J. Fouch, D. E. James, and E. D. Humphreys (2009), Shear wave splitting and the pattern of mantle flow beneath eastern oregon, *Earth and Planetary Science Letters*, *288*, 359–369.

Mooney, W. D., and C. S. Weaver (1989), Regional crustal structure and tectonics of the Pacific Coastal States; California, Oregon, and Washington, *Geophysical Framework of the United States*, *172*, 129–162.

Perry, H. K. C., C. Jaupart, J. C. Mareschal, and N. M. Shapiro (2006), Upper mantle velocity-temperature conversion and composition determined from seismic refraction and heat flow, *Journal of Geophysical Research-Part B-Solid Earth*, p. 14 pp.

Phillips, W. S., M. L. Begnaud, C. A. Rowe, L. K. Steck, S. C. Myers, M. E. Pasyanos, and S. Ballard (2007), Accounting for lateral variations of the upper mantle gradient in Pn tomography studies, *Geophysical Research Letters*, *34*(14), L14,312.

Polet, J., and H. Kanamori (2002), Anisotropy beneath California: shear wave splitting measurements using a dense broadband array, *Geophysical Journal International*, *149*(2), 313–327.

Raitt, R. W., G. G. Shor, T. J. G. Francis, and G. B. Morris (1969), Anisotropy of Pacific upper mantle, *Journal Of Geophysical Research*, *74*(12), 3095–&.

Roth, J. B., M. J. Fouch, D. E. James, and R. W. Carlson (2008), Three-dimensional seismic velocity structure of the northwestern United States, *Geophysical Research Letters*, *35*(15).

Savage, M. K., and A. F. Sheehan (2000), Seismic anisotropy and mantle flow from the Great Basin to the Great Plains, western United States, *Journal Of Geophysical Research-Solid Earth*, *105*(B6), 13,715–13,734.

Savage, M. K., and P. G. Silver (1993), Mantle deformation and tectonics: Constraints from seismic anisotropy in the western United States, *Physics Of The Earth And Planetary Interiors*, *78*(3-4), 207–227.

Schutt, D., E. D. Humphreys, and K. Dueker (1998), Anisotropy of the Yellowstone hot spot wake, eastern Snake River Plain, Idaho, *Pure And Applied Geophysics*, *151*(2-4), 443–462.

Silver, P. G. (1996), Seismic anisotropy beneath the continents: Probing the depths of geology, *Annual Review Of Earth And Planetary Sciences*, *24*, 385–&.

Smith, G. P., and G. Ekstrom (1999), A global study of Pn anisotropy beneath continents, *Journal Of Geophysical Research-Solid Earth*, *104*(B1), 963–980.

Sung, L. Y., and D. D. Jackson (1992), Crustal and uppermost mantle structure under southern California, *Bulletin Of The Seismological Society Of America*, *82*(2), 934–961.

Waite, G. P., D. L. Schutt, and R. B. Smith (2005), Models of lithosphere and asthenosphere anisotropic structure of the Yellowstone hot spot from shear wave splitting, *Journal Of Geophysical Research-Solid Earth*, *110*(B11).

Walker, K. T., G. H. R. Bokelmann, and S. L. Klemperer (2004), Shear-wave splitting beneath the Snake River Plain suggests a mantle upwelling beneath eastern Nevada, USA, *Earth And Planetary Science Letters*, *222*(2), 529–542.

West, J. D., M. J. Fouch, J. B. Roth, and L. T. Elkins-Tanton (2009), Vertical mantle flow associated with a lithospheric drip beneath the Great Basin, *Nature Geoscience*, *2*(6), 439–444.

Yan, Z. M., and R. W. Clayton (2007), Regional mapping of the crustal structure in southern California from receiver functions, *Journal Of Geophysical Research-Solid Earth*, *112*.

Yang, Y. J., M. H. Ritzwoller, F. C. Lin, M. P. Moschetti, and N. M. Shapiro (2008), Structure of the crust and uppermost mantle beneath the western United States revealed by ambient noise and earthquake tomography, *Journal Of Geophysical Research-Solid Earth*, *113*(B12).

Zandt, G., and E. Humphreys (2008), Toroidal mantle flow through the western US slab window, *Geology*, *36*(4), 295–298.

Zandt, G., H. Gilbert, T. J. Owens, M. Ducea, J. Saleeby, and C. H. Jones (2004), Active foundering of a continental arc root beneath the southern Sierra Nevada in California, *Nature*, *431*(7004), 41–46.

Zhao, L. S. (1993), Lateral variations and azimuthal isotropy of Pn velocities beneath Basin and Range Province, *Journal Of Geophysical Research-Solid Earth*, *98*(B12), 22,109–22,122.

Zhu, L., and H. Kanamori (2000), Moho depth variation in southern California from teleseismic receiver functions, *Journal Of Geophysical Research*, *vol.105, no.B2*, 2969–80.

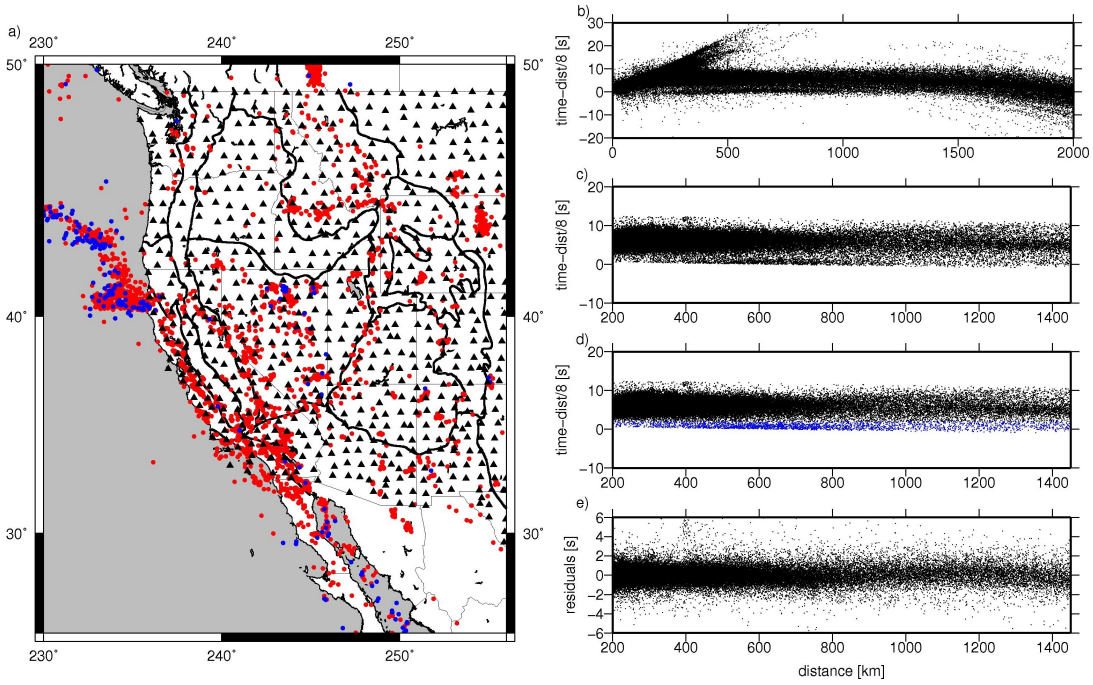

Figure 2.1: a) Events (red circles) and USArray stations (black triangles) used in this study. b) Time-distance plot of all available P-wave picks with an epicentral distance smaller than 2000 km. c) Picks left after the iterative windowing procedure. d) Blue circles show early arrivals, mostly from offshore events (see part a). e) Residuals after one-dimensional time term fit.

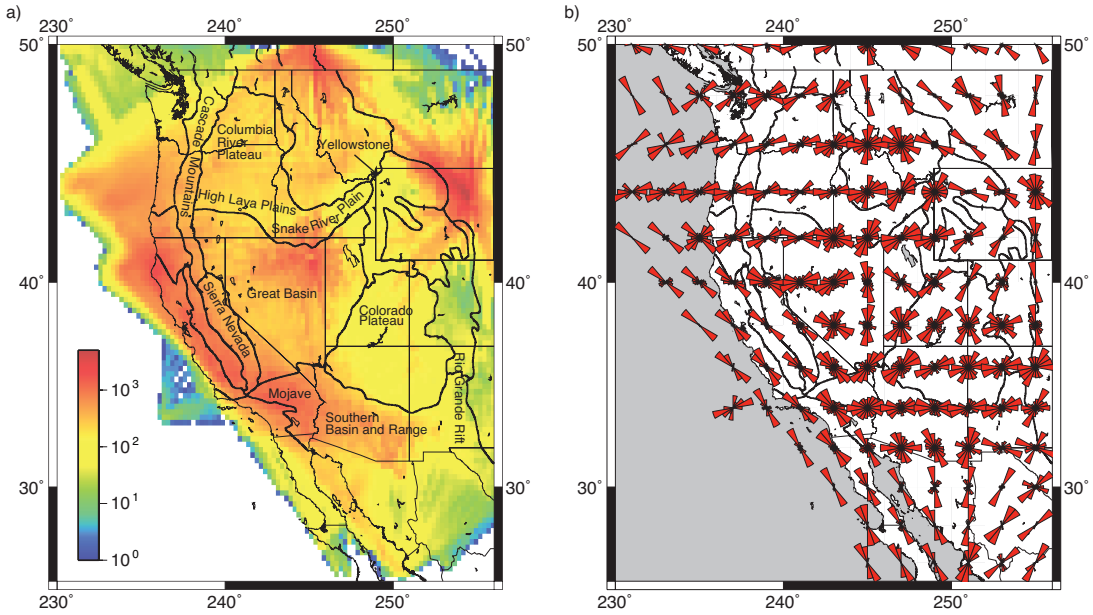

Figure 2.2: a) Ray count per cell. b) Azimuthal coverage, averaged over 64 cells (2° by 2°) in 20° bins in azimuth.

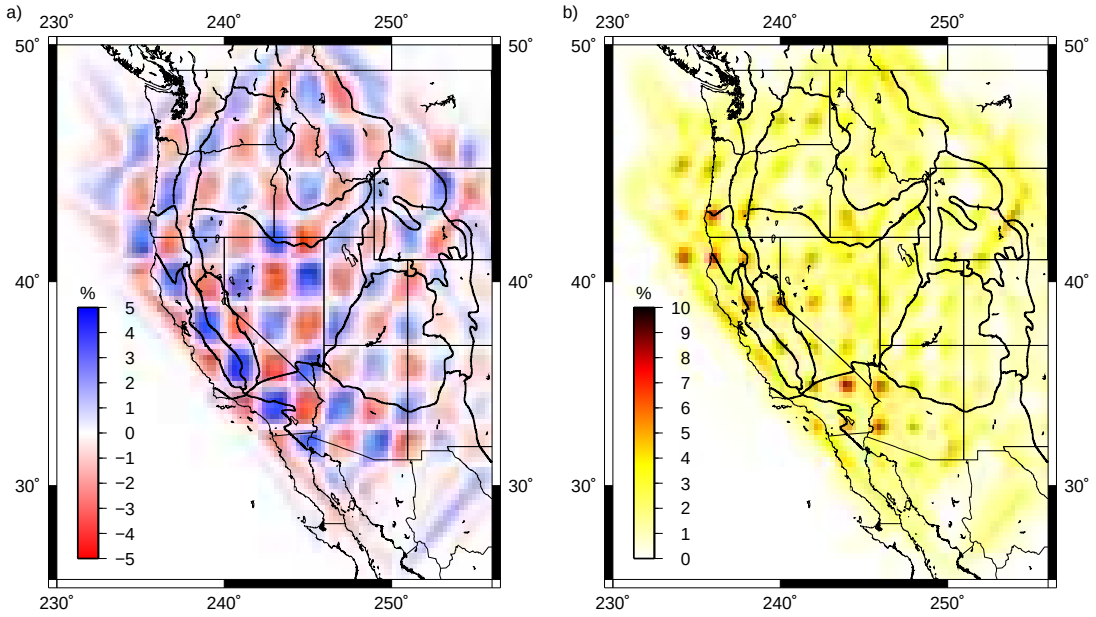

Figure 2.3: Checkerboard test: synthetic data are generated with ± 5% isotropic perturbations only. a) Recovered isotropic model. Red colors indicate recovered synthetic slow anomalies and blue colors represent recovered fast anomalies. b) Leakage into anisotropic model parameters.

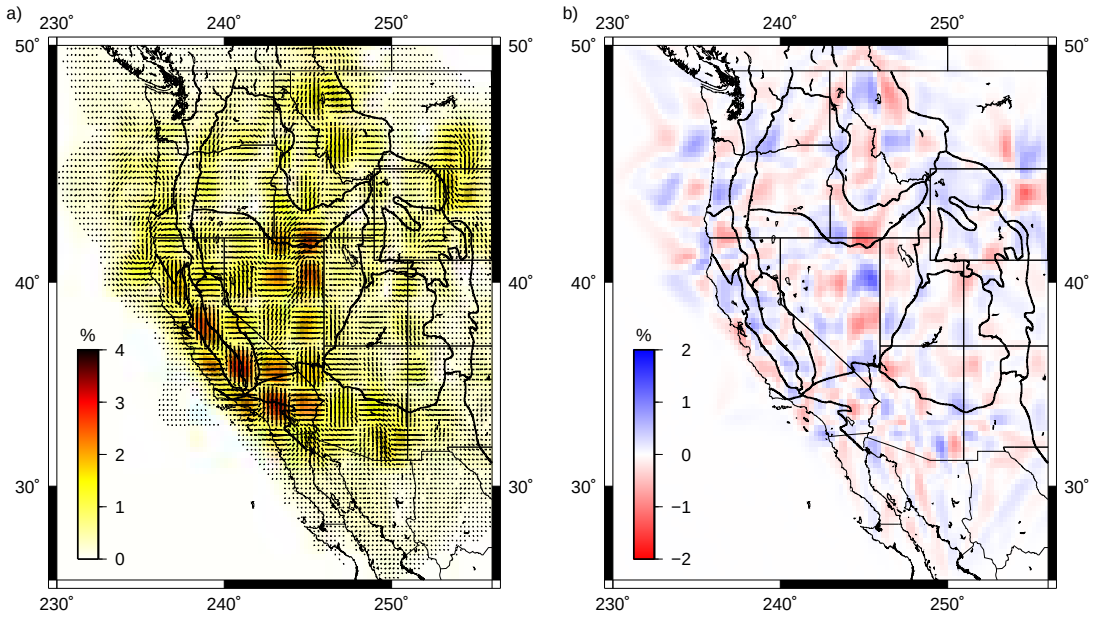

Figure 2.4: Checkerboard test: synthetic data are generated with 5% anisotropy only ($[V_{fast}\text{-}V_{slow}]/V_{iso}$=0.05). a) Recovered anisotropy model. b) Leakage into isotropic model parameters.

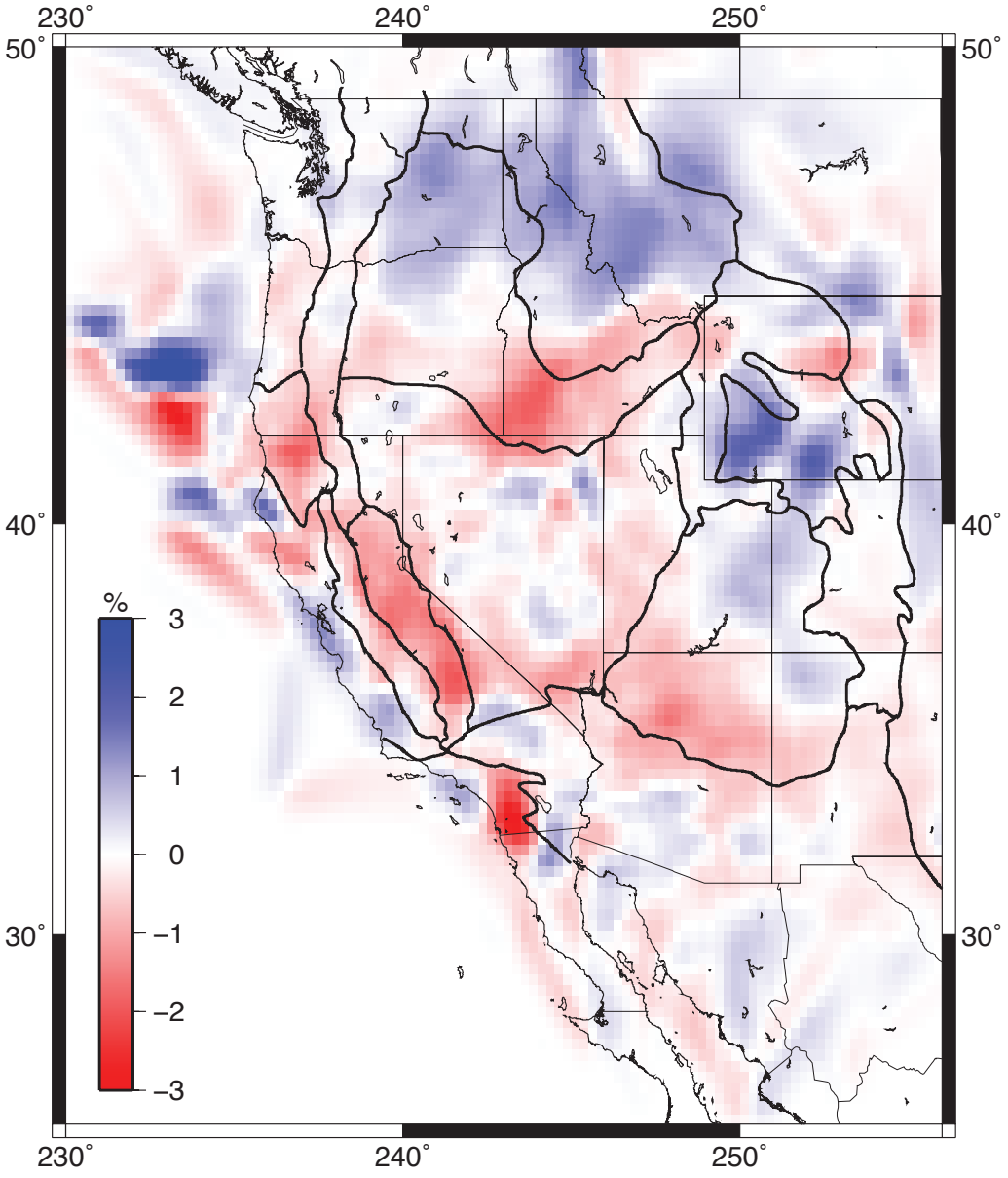

Figure 2.5: Isotropic velocity perturbations resulting from a simultaneous inversion for isotropic and anisotropic parameters. Red colors indicate areas of lower velocities and blue colors regions with higher velocities. The average velocity is 7.93 km/s.

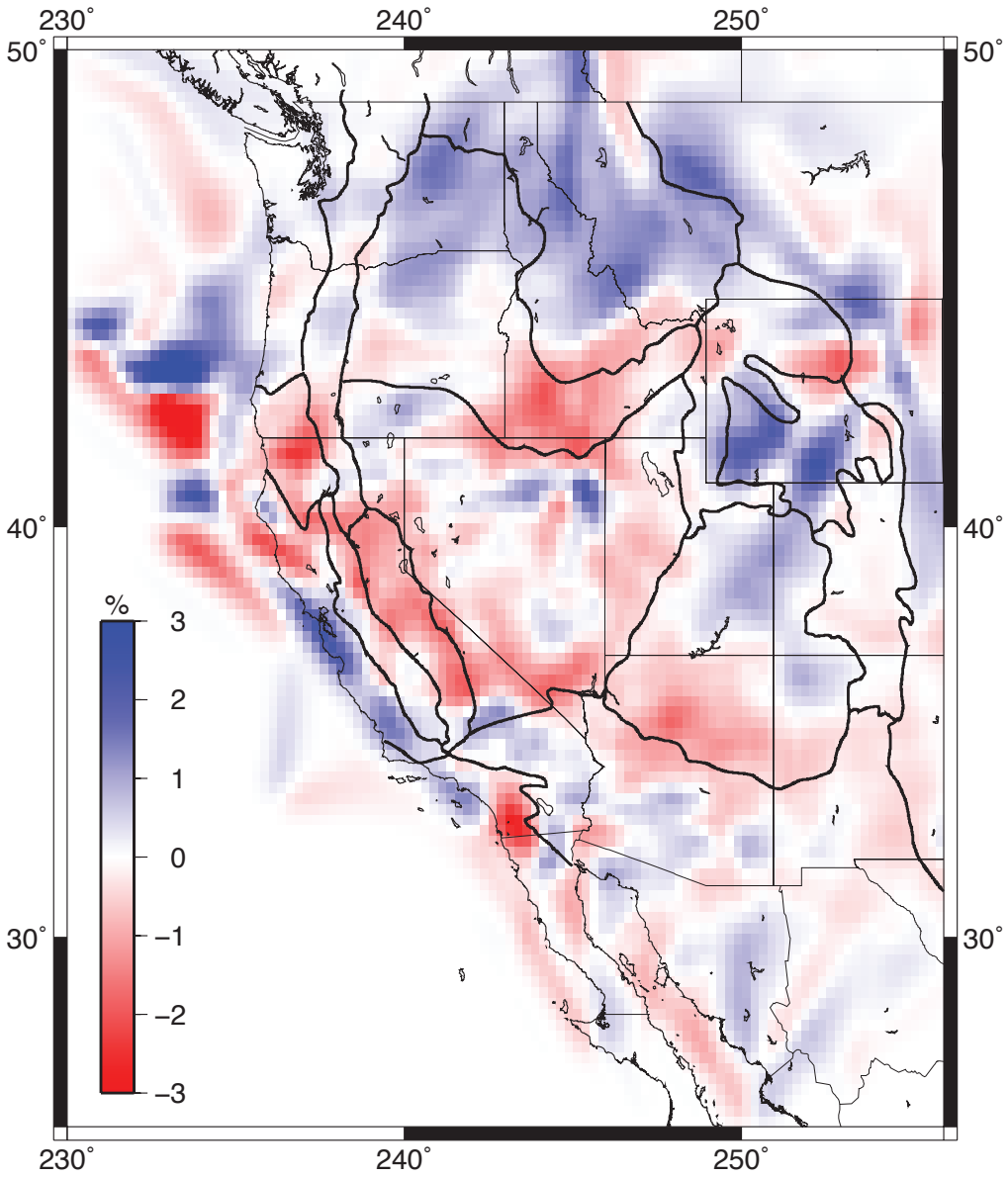

Figure 2.6: The velocity variations obtained from an isotropic model only (no azimuth dependent parameters included in the inversion).

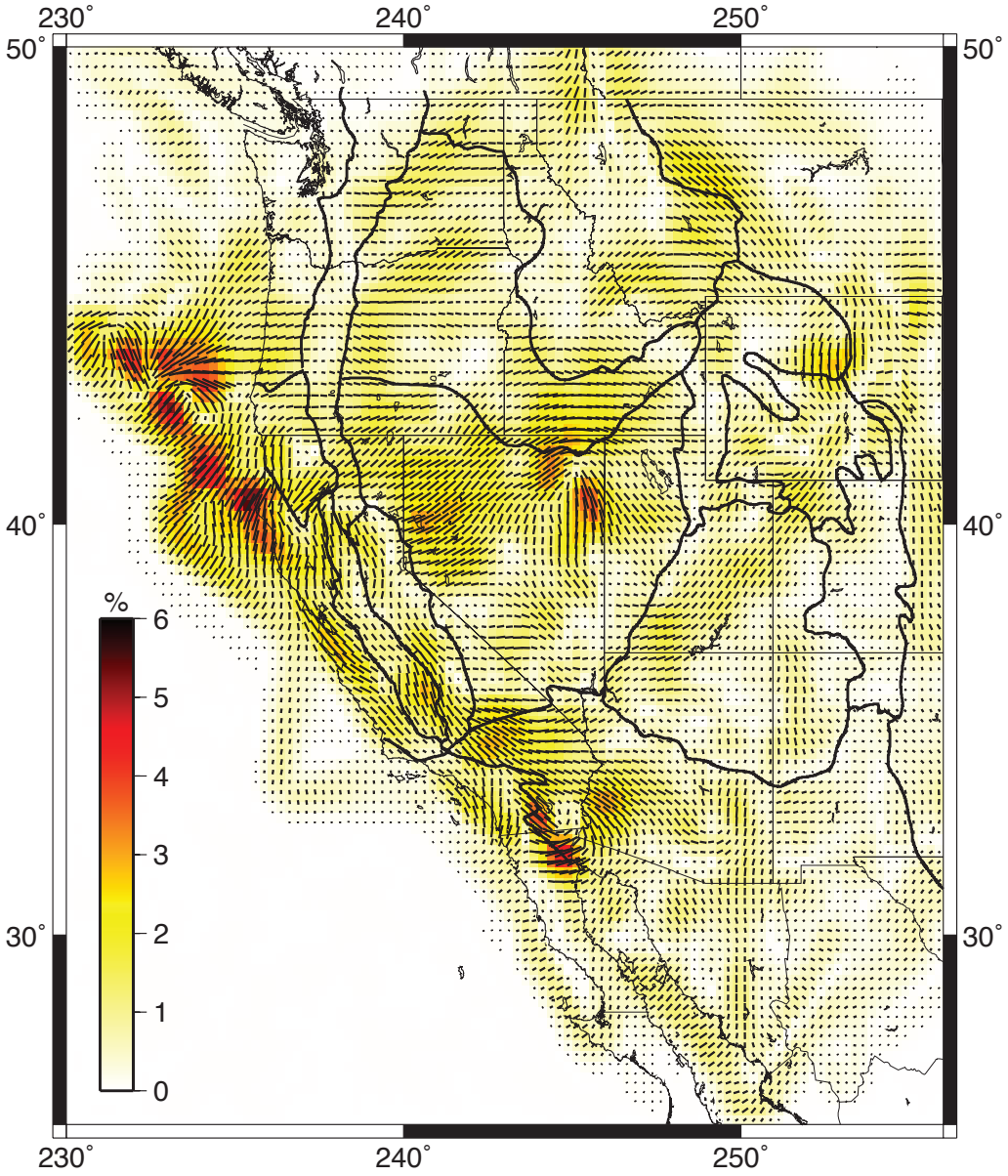

Figure 2.7: The azimuthal anisotropy model. The black lines indicate the Pn fast axis with the length of the line proportional to the strength of the anisotropy. The anisotropy strength is also colored by percent (see scale).

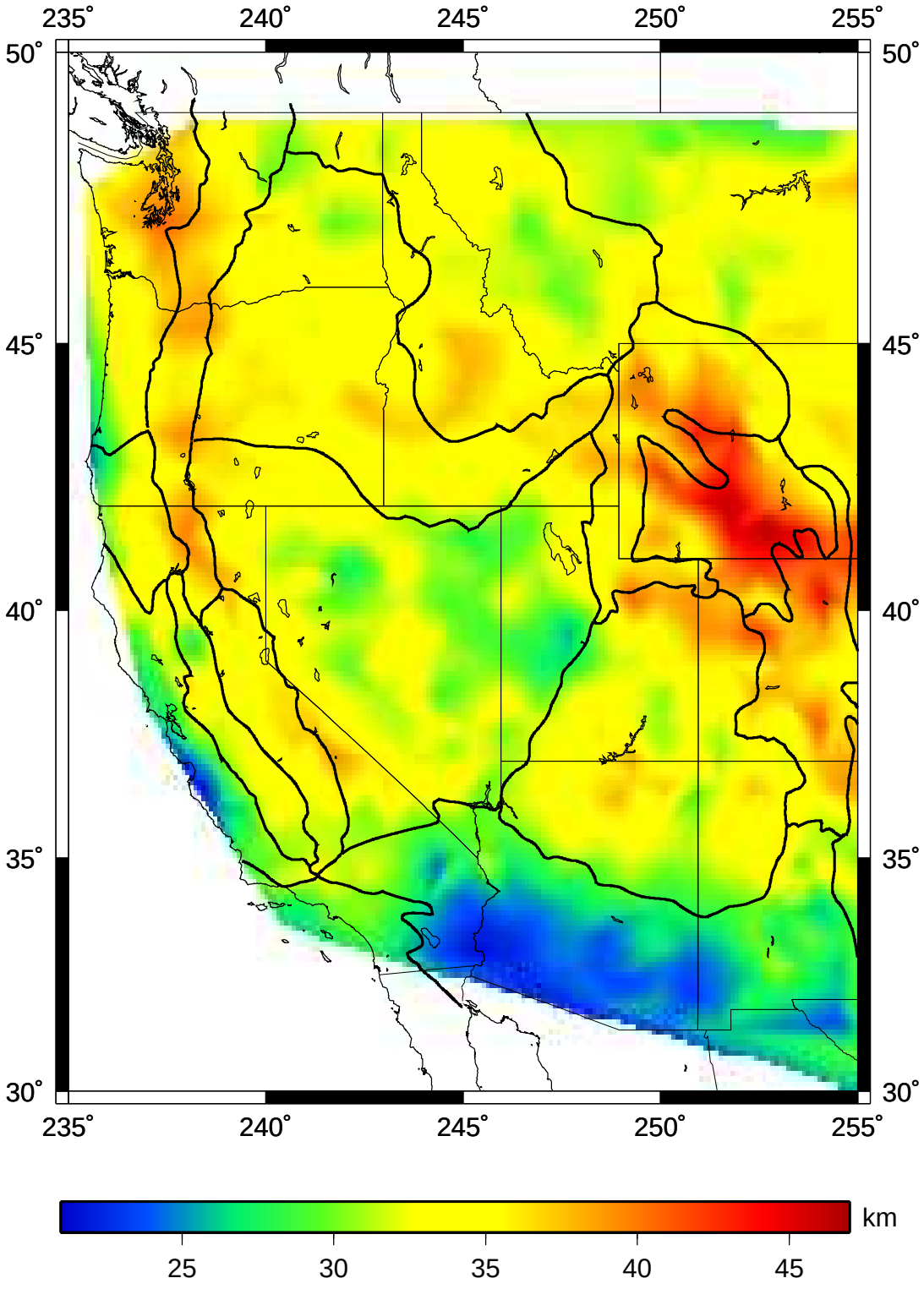

Figure 2.8: Crustal thickness estimates from station time terms. Crustal velocity is assumed to be constant at 6.3 km/s.

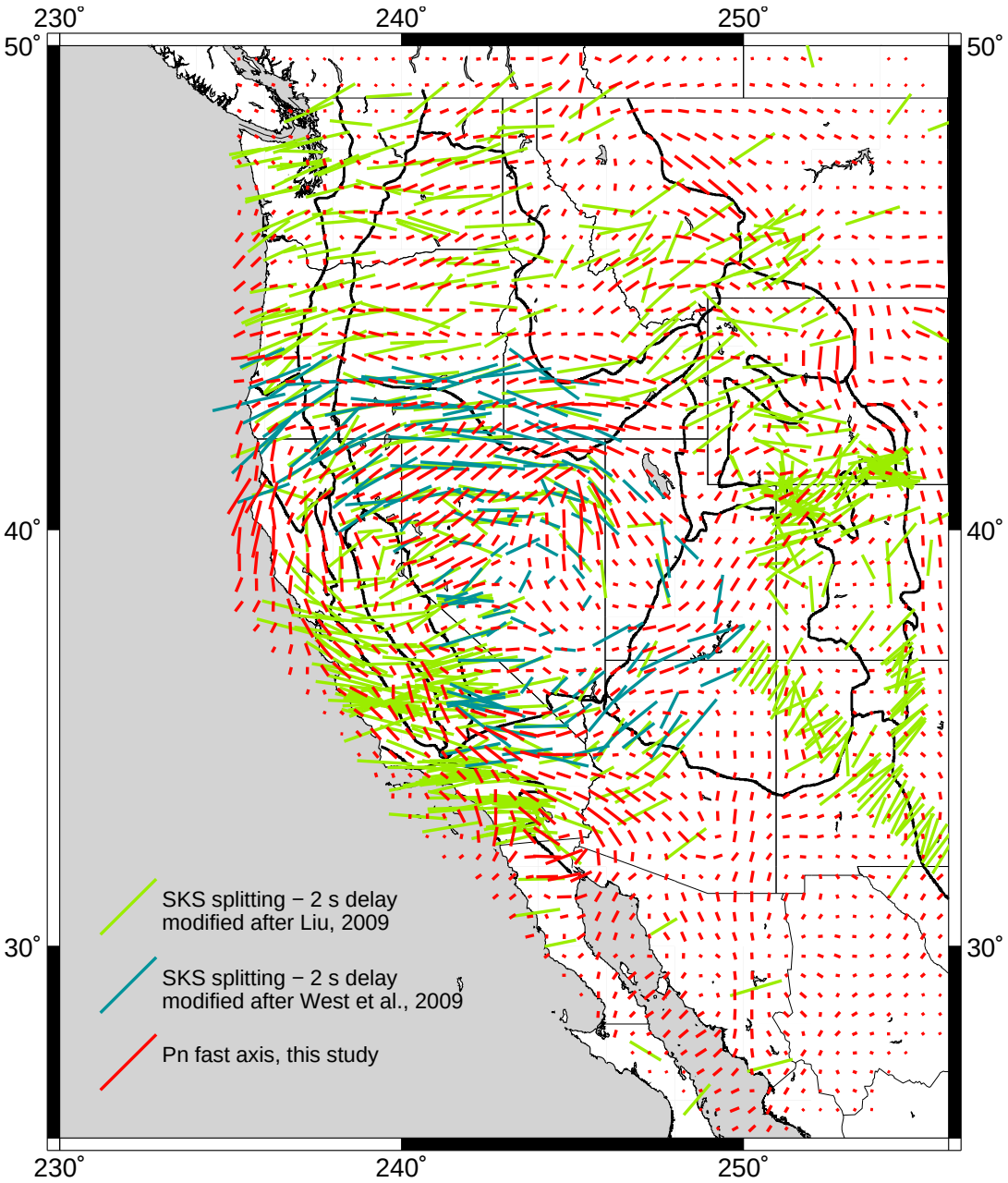

Figure 2.9: Comparison of shear wave splitting fast polarization directions (blue colors) and the Pn fast axis (red) in the western United States. The shear wave splitting results are modified after *Liu* [2009] and *West et al.* [2009].

Chapter 3

Localized Imaging of the uppermost Mantle with USArray Pn Data

USArray has now provided several years of high-quality seismic data and improved ray coverage for much of the western United States. This allows increased resolution for regional studies of the lithosphere and deeper structure of the North American continent. In this study, we use Pn phases in the USArray data set to solve for velocity structure in the uppermost mantle in the western United States. This article focuses on localized imaging techniques that complement traditional Pn tomography analysis. We apply waveform cross-correlation to obtain inter-station travel times between the closely and uniformly spaced USArray stations. This allows us to use traces without phase picks and reduces errors associated with the picking. We obtain differential times that can directly be used to fit locally for slowness and, depending on the approach, for the direction and curvature of the incoming wavefront. The various measurements of incoming wavefronts at different sub-arrays provide constraints on azimuthal variations in velocity. The traditional tomography approach and the local fitting method reveal similar large-scale features. No regularization is applied with the local method, and the resulting velocity maps reveal smaller-scale structures than the tomographic images.

3.1 Introduction

With the implementation of USArray, data coverage in regions without local seismic networks has been much improved, which has led to better resolved crust [e.g., *Moschetti et al.*, 2010] and mantle structure [e.g., *Burdick et al.*, 2008; *Schmandt and Humphreys*, 2010] beneath the western United States. However, even with greater data coverage, traditional tomography approaches usually require regularization due to uneven grid sampling and ray tracing is often simplified. Alternative methods for surface- and body-wave data that profit from the large USArray station network and complement traditional tomography techniques have been proposed, as for example local surface-wave tomography [e.g., *Lin et al.*, 2009; *Pollitz and Snoke*, 2010; *Lin and Ritzwoller*, 2011] or waveform based analysis [*Sun and Helmberger*, 2011].

Here we present a localized array approach to map regional velocity structure using horizontally traveling Pn waves. We focus mainly on the localization method, and the reader is referred to *Buehler and Shearer* [2010] for a discussion of the tectonic implications of our models. Because Pn is a Moho refracted wave that travels in the mantle lid, it provides constraints on seismic velocity and anisotropy within a very confined depth interval. These maps provide information on temperature and compositional variations in the upper mantle [e.g., *Goes and van der Lee*, 2002; *Perry et al.*, 2006]. Even with the dense USArray station coverage, traditional teleseismic body-wave tomography studies often do not have the vertical resolution to accurately map velocity structure in the uppermost mantle. Combining surface- and body-wave observations provides better depth resolution, and a recent USArray shear-wave study adds short-period surface-wave data to increase resolution in the shallowest part of the model [*Obrebski et al.*, 2011]. Moho refracted Pn waves provide additional information in the uppermost mantle, with the capacity to further constrain surface-wave or other body-wave tomographies that average anomalies over larger depth intervals.

We exploit the closely spaced transportable array stations to apply localized wavefront fitting techniques to Pn data to image regional velocity structures and anisotropy in the uppermost mantle below the western United States. These array-based methods provide velocity maps similar to traditional tomography, but have the potential to reveal anomalous regions with better resolution because they do not rely on regularization. These local approaches are fast and simple, can account for off-great-circle-path arrivals, and help validate traditional Pn tomography results.

Working with the Pn phase is challenging because the emergent character of the arrival makes accurate phase picking difficult. In section two we describe the data selection and the cross-correlation procedure we apply to improve the relative timing between stations. Using these times, we solve for the direction and apparent velocity of the incoming wavefronts using a local approach, as illustrated in section three. We use the apparent velocities to produce maps similar to traditional tomography. The directions of arrival are later used to investigate velocity changes with back-azimuth, which can be related to upper mantle anisotropy and Moho slope. In section four we show that traditional Pn travel time tomography produces images of large-scale velocity structure and fast anisotropy directions that largely agree with the local estimates.

3.2 Data Selection and Processing

The USArray Array Network Facility (ANF) analysts routinely pick first (and on a number of traces later) arrivals in the USArray data set. These picks are available for download through the ANF website ($http://anf.ucsd.edu/tools/events/download.php$, last accessed December 2011), and provide data that can be used directly in traditional travel-time tomography [e.g., *Buehler and Shearer*, 2010; *Burdick et al.*, 2008, 2010, 2012; *Steck et al.*, 2011].

Our goal is to improve the relative timing between the transportable array stations in an automated and objective procedure. Pn waveforms characteristically have weak amplitudes and/or emergent onsets. This makes waveform processing and precise timing challenging. Accurate inter-station differential times are important for local velocity measurements among nearby stations. To reduce timing errors and improve the consistency of the times, we cross-correlate the Pn waveforms of regional earthquakes. This has the further advantage of often providing times for waveforms with no analyst-assigned Pn picks. The inter-station differential times associated with the cross-correlation peaks can then be used to fit for the apparent slowness, azimuth, and curvature of the wavefront as it travels across a localized subset of the stations. In addition, we can use the differential times to realign the seismograms to obtain self-consistent data sets for traditional tomography [*Vandecar and Crosson*, 1990].

3.2.1 Stations and Events

Pn is a refracted ray traveling in the mantle lid just below the Moho, and arrives first at stations at regional distances. The cross-over distance, where the first arrivals change from Pg to Pn, depends on crustal thickness. Pn typically arrives first at stations with an epicentral distance of about 150 km and larger on continents. Here we use stations that are between 180 km and 1450 km from the epicenter for receivers west of longitude 110° W, and between 240 km and 1450 km for receivers east of 110° W. We make this division to accommodate the increased thickness of the crust east of the Great Basin in order to avoid erroneous picks and/or cross-correlation alignments on the usually higher-amplitude crustal phase Pg without eliminating too much data in the west. In addition we discard events with hypocenter depths larger than 30 km.

We collect all available ANF picks from May 2004 to August 2011 that satisfy the criteria above, recorded at stations west of 100° W. To identify the Pn picks we proceed similarly to *Hearn* [1996] and apply an iterative procedure to identify picks with a maximum residual of 6 s following a simple straight-line fit to time versus distance (requiring at least 10 picks per earthquake and 10 picks per station). There are ∼371,000 P picks currently in the ANF database at epicentral distances between 180 and 1450 km, of which ∼125,000 are labeled Pn. After the windowing procedure ∼161,000 picks remain. This group of arrivals is associated with 6348 earthquakes and quarry blasts.

For this set of events we download waveforms from the ANF with the Antelope database tools, including traces without an analyst pick. Figure 3.1 shows the resulting event and station locations. The stations are color coded by the number of months data from our time period was recorded at that receiver. We save the waveforms at 40 Hz sample rate (stations with lower sampling rates are re-sampled using spline interpolation) and associated meta-data in an event-based data archive for further processing.

3.2.2 Pn Waveform Cross-Correlation

Pn waveforms are challenging to cross-correlate reliably because they often have marginal signal-to-noise and are typically followed by the higher-amplitude Pg phase. It is important to initially align the waveforms well to avoid misidentifying Pg as Pn. Fortunately the ANF analyst picks provide good reference times for many of the seismograms. For seismograms without picks we apply an automatic picking algorithm based on a short-time-average to long-time-average ratio (STA/LTA) function [*Earle and*

Shearer, 1994]. This algorithm works well with emergent and low amplitude arrivals. We high-pass all the seismograms at 1 Hz for consistent automatic picking.

In some cases the autopicker may only trigger on the generally higher-amplitude crustal phase. To avoid late alignments on Pg, we restrict the search for picks to a predefined Pn time window. We calculate a mean slowness and intercept point with straight-line fits using ANF picks that are 'Pn' labeled. If an event is associated with at least 10 Pn picks, we calculate the theoretical arrival times for all the seismograms with a straight-line fit through the single-event data points. Otherwise we use the slope and intersection values calculated for the whole data set. We then use this average velocity $\pm$ 0.4 km/s to calculate the start and end times of the picking window. We require an STA/LTA value of at least 2.5 within the window in order for the pick to be recorded. Once the autopicker is applied to all the traces, we discard seismograms that have neither an analyst pick nor an automatic one in the defined Pn windows. Then we iterate again to remove events that are associated with less than ten picks, stations that record less than ten earthquakes, and arrivals with residuals larger than six seconds after a straight-line fit.

For each event, we then cross-correlate every trace with every other trace for all the n first arrival times of an event. This produces $n(n-1)/2$ cross-correlations per event. We experimented with different correlation window lengths and obtained satisfactory results with widths two to three times the length of the dominant period centered around the pick. The seismograms are bandpass filtered between 0.8 and 2.5 Hz prior to cross-correlation to eliminate microseisms and uncorrelated high-frequency noise. We find that in many cases we can prevent cycle skipping if we keep the maximum allowed time shift around one second. Figure 3.2 shows examples of cross-correlations of various qualities. Following some experimentation, we settled on a uniform cross-correlation window length of 2.5 seconds for all the traces, starting one second before the pick.

3.2.3 Waveform Re-Alignment

Differential times from cross-correlations for a set of receivers can directly be used for subsequent wavefront fitting. However, the relative travel-time measurements are almost never consistent with a single set of absolute times, i.e., $\tau_{12} + \tau_{23} \neq \tau_{13}$, where τ_{12} is the differential time between station one and two, etc. *Vandecar and Crosson* [1990] used the measured differential times τ_{ij} between stations in a linear system to solve for a

set of realigned absolute arrival times t for an event, minimizing the penalty function $F = \sum(\tau_{ij} - (t_i - t_j))^2$. This provides a self-consistent set of arrival times for every earthquake or quarry blast. The adjusted arrival times can be used both in traditional travel-time tomography and localization approaches. We proceed in similar fashion as *Vandecar and Crosson* [1990], but find that for the Pn differential times a robust regression method provides better results compared to ordinary least squares, due to occasional large errors in the differential times (e.g., cycle-skipping in the cross-correlation peaks). We applied the *robustfit* routine from MATLAB that implements the Iteratively Reweighted Least-Squares (IRLS) method.

To further reduce errors associated with cycle skips we adapted a procedure based on the approach by *Vandecar and Crosson* [1990]: First, the system of equations is solved with a data vector d that contains the inter-station time shifts associated with the peak of the correlation-function and the available picks. Next we find the data residuals > 0.25 s and test if any other shifts associated with peaks in the cross-correlation function with values higher than 0.6 provide a better fit. We exchange the elements in the data vector accordingly and proceed iteratively to obtain the final set of realigned arrival times (Figure 3.2).

We expect neighboring stations to have the same polarity and more similar waveform characteristics than receivers further apart. Hence the differential time observations are weighted according to inter-station distance, assigning a weight of 1 to all station pairs that are less than 250 km apart, and decaying weights with larger distances. We discard stations that correlate with a mean correlation coefficient of less than 0.6. This approach produces about 107,000 re-aligned picks (73,000 ANF picks and 34,000 auto-picks). The differential times obtained from cross-correlation and also the realigned traces can directly be used in the subsequent wavefront fitting analysis.

3.3 Localization

The closely spaced stations of USArray allow us to experiment with local array methods to regionally image velocity structure in the uppermost mantle. We use a variety of approaches based on local plane- and circular-wavefront fitting techniques [e.g., *Almendros et al.*, 1999; *Pezzo and Giudicepietro*, 2002] that we apply to station subsets of USArray. These local methods do not require the regularization (i.e., damping and smoothing) used to stabilize the typically ill-posed inversion problem of traditional

travel-time tomography, and thus should provide better lateral resolution and velocity anomaly amplitude retrieval.

The localization approach assumes that the Pn wavefront is locally coherent across station subarrays. If we knew the exact hypocenter location and assume that lateral velocity variations are very small, we could simply compute the great-circle-path between stations and events and use the differential times to solve directly for the apparent velocity of the passing wavefront. More likely, velocity variations between source and receiver will bend the ray paths, in which case more accurate results will be obtained by simultaneously solving for the direction and apparent velocity of the incoming wavefronts. Assuming a flat Moho and a uniform crust, the measured apparent velocity would still correspond to the true medium velocity in the uppermost mantle. Again, however, this is probably not a reasonable assumption, and just as in the case of traditional Pn tomography, station time terms should be applied to take into account the effects of crustal velocity and thickness variations. In addition, azimuthal anisotropy in the upper mantle may lead to varying velocity observations for events from different directions. For regions with good azimuthal coverage, we can estimate this anisotropy by fitting the azimuthal distribution of apparent velocities with $\cos 2\theta$ curves. In the sections that follow, we will start with simple wavefront fitting, and then add in the complexities of station terms, Moho slope estimates, and anisotropy.

3.3.1 Station Triangularization and Wavefront Fitting

The smallest array subset to estimate directions and velocities of incoming plane-waves contains three stations. To obtain an even mesh of station triangles, we apply a Delaunay triangularization to all the USArray station locations (Figure 3.3a). We then solve for the direction and apparent slowness of incoming plane wavefronts for each earthquake and station triangle directly using inter-station differential times. To estimate the parameters for a plane-wave, we solve $\tau_{ij} = \mathbf{p} \cdot \mathbf{x}_{ij}$, where τ_{ij} is the data vector with the differential times, $\mathbf{x}$ contains the station spacing in x and y (east and north), and $\mathbf{p}$ the horizontal slowness components.

Inter-station differential times can be directly obtained from the cross-correlations (section 3.2.2), or can be calculated from the set of realigned arrival times (section 3.2.3). The advantage of using realigned times is their self-consistency, and in ensuring that large timing errors in individual cross-correlation measurements (as for example

from cycle skipping) do not influence the wavefront fitting. In addition, the same set of realigned times can be used in traditional time-term tomography, which allows for detailed comparisons between the two methods. Alternatively, one can simply use the differential times from cross-correlation directly, and for good correlations these raw inter-station times may be the most exact. Hence we start with the raw differential times from cross-correlation (section 3.2.2), since this is the most straightforward approach to apply the localization method to a new dataset.

The aperture of a USArray station triangle (mean station separation of ∼70 km) spans ∼30 degrees for arrivals close to the cross-over distance of 180 km, and a plane-wave simplification is not valid for these arrivals. We begin by fitting for plane waves if the distance between the earthquake and triangle center is larger than 500 km, and for circular wavefronts using the catalog epicenter location for closer ranges (the wavefront looks approximately like a circle at the surface of the Earth as it sweeps across the array of stations. In this case $\mathbf{x}$ simply contains the differences in epicentral distance, and we solve for the apparent slowness). We use the set of three differential times only if the mean correlation coefficient is greater than 0.7. For each station triangle we obtain several velocity measurements from different earthquakes at various back-azimuths. Figure 3.3b shows the mean velocity for each tripartite array, plotted at the center of each triangle. No circle is plotted in triangles associated with fewer than five velocity measurements.

Because good cross-correlation results are not obtained for every station-event pair, a fixed triangularization will discard some data because usable traces are often scattered across subsets of the array. This creates the gaps seen in Figure 3.3 where some triangles do not show a measurement. To maximize usable data and to obtain a more continuous mesh of velocity measurements, we next apply the triangularization separately to all the recording stations of an earthquake, allowing the largest triangle leg to be 150 km. We then again solve for the incoming wavefronts for all the triangles whose differential times satisfy the minimum correlation criteria. We put a two-dimensional 0.25° x 0.25° grid over the model area to accommodate the results of the various triangularizations and we assign the measured velocity for a tripartite array to all the regular grid-points that lay within the triangle. The mantle piercing point of the head-wave is not located directly below the station triangle, but in practice we have found that this offset introduces little bias. Figure 3.4b) shows the mean value per grid-point after we solved for the velocity parameters of the triangle-event combinations.

To avoid errors from the plane-wave approximation and fixed hypocenter locations, we can account for the curvature of the wavefront [e.g., *Almendros et al.*, 1999]). Using the predetermined hypocenter locations in the catalog keeps the problem simple and linear. But ideally, as the hypocenter locations might be inaccurate or lateral velocity variations may cause the direction of the incoming plane wave to deviate from the great-circle path, we want to simultaneously solve for the curvature, apparent velocity, and azimuth of the passing wavefront. To take this into account, we solve for apparent slowness S and origin coordinates lat_o and lon_o of the non-linear equation $\tau_{ij} = S(\delta_i - \delta j)$ where δ_i is the great-circle distance between station and event.

Although we measure three differential times for each tripartite array, only two of them are independent. However, our problem now consists of three unknowns, generating an underdetermined system with non-unique solutions. To stabilize the approach, we search for a solution close to the reported catalog epicenter location. As described in the next section, we also experiment with larger station subsets. However, in general, these more complicated approaches provide very similar results to the simple combined plane- and spherical wavefront method (Figure 3.4c). Thus, it does not appear that epicentral errors or ray bending effects due to lateral velocity variations are very important in our local velocity estimates.

As mentioned in the starting paragraph of this section, another approach is to analyze the self-consistent realigned times obtained over all stations for each event (described in section 3.2.3), rather than the raw differential times from the cross-correlation. This is our preferred approach to compare maps from localization imaging to traditional travel-time tomography as the same data set can be used for both. In addition, for a generally low signal-to-noise data set, or for locations with only few arrivals, this likely provides the more accurate localization map since individual correlation measurement are error-prone. In this case, we use the three absolute times t_k of a station triangle to solve for the arrival time at the origin (center of the triangle) t_0, and the horizontal slowness components: $t_k = t_0 + \mathbf{p} \cdot \mathbf{x}_k$. This provides slightly smoother varying velocity maps (Figure 3.4d) compared to the ones with cross-correlated differential times but the difference is small and all the images show consistent velocity structure. We will later compare this image to that obtained using the same set of self-consistent times in traditional Pn tomography.

3.3.2 Larger Sub-Arrays and Station Time Terms

Here we experiment with using larger station subsets, which should provide more stable, albeit lower resolution, velocity estimates. Residuals of this now overdetermined system allow us to introduce station time terms as described in the next paragraph. To obtain station polygons, we first identify all triangles associated with each station. If a station is part of at least three triangles (i.e., sub-arrays of at least five stations), and the mean correlation coefficient for the differential times of this group of receivers is larger than 0.7, we proceed to fit for the incoming wavefront. The obtained slowness and azimuth information is assigned to all the grid points within the polygon spanned by the three or more triangles. Figure 3.5 shows the resulting mean measured apparent velocity at each location, which, as expected, resembles a smoothed version of Figure 3.4.

To this point we have not considered changes in station elevation or underlying crustal structure. Crustal velocity structure and crustal thickness differences below individual stations will contribute to the measured differential times. To account for delays introduced by these effects, we can include station time terms just as in the classic Pn time-term approach [*Hearn*, 1996]. We define the travel-time difference between two stations as $\tau_{ij} = S(\delta_i - \delta j) + (\xi_i - \xi_j)$, where ξ_i denote the station corrections and δ_i the great-circle distances. The station terms are initially set to zero. We then solve for the slowness of incoming wavefronts for all the events and sub-arrays, keeping track of the residuals after each fit $res_{ij} = \delta\xi_{ij} = \delta t_{ij} - S(\delta_i - \delta j)$, where res_{ij} represents the residual for the differential time between station i and event j. After one run through all the events, the residuals are put into a linear system to solve for individual station statics ξ using least squares by minimizing $F = \sum(\delta\xi_{ij} - (\xi_i - \xi_j))^2$. The mean station term is set to zero.

In subsequent iterations, the difference in station time terms is subtracted from the observed differential times, and wavefronts are fitted to the corrected τ_{ij}. After about ten iterations, the change in time terms is small enough to consider the system converged. For stability, we start with the fixed epicenter method, solve for the apparent slowness only, and iterate for the station terms. These station statics are then used as starting values for the more sophisticated method with more model parameters where the wavefront curvature is allowed to vary.

The station time terms and velocity estimates with corrected times are illustrated in Figure 3.6. Large station term values (e.g., stations in the Sierra Nevada) can reduce

the size of the associated velocity anomaly. Time terms in the Snake River Plain are close to zero, not influencing the mapped velocity structure. However, the station delays are large at receivers above the current location of the Yellowstone hotspot, and the mean apparent velocity is increased with the site-term corrected differential times.

3.3.3 Anisotropy and Moho Slope

Station terms can correct for mean crustal thickness variations beneath stations, but cannot account for the azimuthally-dependent time delays produced by a dipping Moho under a station or by azimuthal anisotropy in the uppermost mantle (Figure 3.7). Because Moho topography and mantle anisotropy vary across the western United States, it is important to consider these effects. We do this by fitting the azimuthal distribution of apparent velocities of triangles with good azimuthal coverage to the equation $Vapp = A + [B\sin\phi + C\cos\phi] + [D\sin 2\phi + E\cos 2\phi]$, where A is the isotropic velocity, the $\sin\phi$ and $\cos\phi$ terms approximate the effects of Moho slope, and the $\sin 2\phi$ and $\cos 2\phi$ terms describe the azimuthal anisotropy of Pn velocity. We do not include 4ϕ terms since observations and models of azimuthal anisotropy in the uppermost mantle have shown a dominant 2ϕ variation [*Raitt et al.*, 1969; *Christensen*, 1984].

For the curve fitting we again apply an iterative re-weighted least squares approach since the velocity measurements typically show large scatter. To obtain stable results, we only consider grid locations with good azimuthal event coverage, and require that the largest gap in direction of the arrival is smaller than 100°. For each grid point, we use the velocity and azimuth measurements stored at that point, as well as the estimates stored for the surrounding eight nodes. Figure 3.8 shows the estimated fast directions and magnitude of the anisotropy ($(V_{fast} - V_{slow})/V_{iso}$) and corresponding isotropic velocities for the triangle fits. Figure 3.9 shows the same parameters for the larger sub-arrays measurements with station-term-corrected differential times. For mapping clarity, we plot the average fast direction in 0.5 degree cells. We observe mostly fault-parallel Pn fast axes in central California, and fairly homogeneous northeast fast axes in the northwestern Basin and Range that rotate to north-south in eastern Nevada. Note how the inclusion of anisotropic parameters seems to show some of the velocity anomalies more clearly, as for example the south-west to north-east striking low velocity anomaly in eastern New Mexico, east of the Rio Grande Rift, near the axis of the Jemez Lineament [e.g., *Karlstrom and Humphreys*, 1998].

Moho topography can be calculated from the station time terms and compared to the localized slope estimates. We find that these results only agree in regions with likely large topography and good azimuthal coverage, as for example below the Sierra Nevada. However, changes in crustal velocity below a station can produce a similar signal as Moho slope. In the analysis for Figure 3.8, where we used station triangles, we did not include station time terms, but for Figure 3.9, with station pentagons, we solved for time terms prior to the curve fitting. In the first case, it is possible that Moho slope terms absorb delays introduced by varying crustal velocities. In the latter case, the time terms already partially account for changes in crustal thickness. It is difficult to resolve the trade-offs between the various parameters, and some experimentation with varying model complexity seems necessary.

3.4 Traditional Travel Time Tomography

For the localization approach, we typically require a minimum correlation coefficient for the differential times among the selected stations. Each measurement is carried out independently, therefore we just use all the available data that pass the cut-off. To use the globally adjusted times in traditional travel-time tomography, we ideally want a well-distributed subset of events to provide uniform data coverage over the study area. Uneven ray coverage can introduce artifacts into velocity maps, as for example smearing along prominent ray paths. To provide more uniform coverage, we apply a modified version of the composite event method of *Lin et al.* [2007], which has the further advantage of reducing the size of the inverse problem.

We first window the realigned picks to remove large outliers after straight-line fits and then remove any events that are recorded at fewer than ten stations. Next, we perform the following steps, following the general approach described in *Lin et al.* [2007]: We find the event with the most picks and keep track of the recording stations. We then find all the events within a radius R of this reference event (here we use $R = 20$ km), and sort these neighboring events in descending order by their number of picks. Because USArray stations do not stay in place but move approximately every two years, two events at the same location might be recorded by different sets of stations. For this reason, we check the number of newly activated stations for each subsequent event within radius R of the target event, starting with the second best recorded (by number of picks) earthquake within the group. We keep an event within the same radius if the arrival set

includes more than 30% new stations. Then we move on to the text target event and so on. Contrary to the composite event method of *Lin et al.* [2007] we do not average the arrival-time residuals, but try to select the best-recorded events in each region. The final set of events contains about 20% of the original earthquakes, but is much more geographically uniform (Figure 3.10).

Next, we invert these times following the tomographic approach of *Hearn* [1996] and further described in *Buehler and Shearer* [2010], which applies a modified time-term method to the large set of residuals. Using a two-dimensional grid along the Moho, the travel-time residuals are parameterized as $\delta t_{es} = \delta\tau_e + \delta\tau_s + \Sigma\Delta_{esk}(\delta S_k + A_k \cos 2\phi_{esk} + B_k \sin 2\phi_{esk})$, where Δ_{esk} is the distance the ray travels in the cell k, δS_k is the isotropic slowness perturbation in cell k, A_k and B_k are the anisotropic parameters for cell k, ϕ is the back azimuth, and $\delta\tau_e$ and $\delta\tau_s$ are the event and station time terms. As in the localization approach, we do not include any 4ϕ velocity variations. Here the event time term $\delta\tau_e$ absorbs not only the time the ray spends in the crust, but also errors in hypocenter locations and absolute timing (since we only have accurate relative times). Variance reduction is about 70% compared to a simple straight-line fit (uniform Pn velocity, no station or event terms), and 30% compared to a one-dimensional time-term tomography (uniform Pn velocity with station and event terms). We find that variance reduction is not much influenced by the use of the realigned times versus the raw analyst and auto-picker picks. Hence the cross-correlation likely does not improve the timing accuracy much for this particular generally low signal-to-noise data set (or the model parameterization is not good enough to capture these small time changes), even though the waveforms appear visually more aligned. Still, we prefer to work with the re-aligned times in the tomography, as this provides us with a consistent and completely objective data set.

The resulting isotropic velocity variations are shown in Figure 3.11 and largely agree with the locally imaged velocity structure, especially when comparing them with the localization maps from the larger sub-arrays. Prominent features include the distinct slow velocity anomalies below the Sierra Nevada and the Snake River Plain. The Yellowstone hotspot track is bounded to the north by a large positive velocity anomaly spanning eastern Washington, northern Idaho and western Montana. The localization and tomography provide consistent fast directions (Figure 3.12); the largest difference is observed in the magnitude of the anisotropy. Synthetic tests in *Buehler and Shearer*

[2010] showed that the anisotropy magnitude is generally less well retrieved than the fast axis with the traditional travel-time tomography. In California we consistently observe mostly fault-parallel Pn fast axes, indicating that the anisotropy is caused by shearing along the plate boundary. Both methods show a rotation of the fast axis around the great Basin, taking a sharp corner in northeastern Nevada at the southern edge of the Snake River Plain.

3.5 Discussion

Consistent large-scale features are seen in the localized images as well as the traditional Pn tomography. These include the slow Pn velocities below the Snake River Plain, the Sierra Nevada, and the western edge of the Colorado Plateau. As expected, the localization method produces more detailed images of the uppermost mantle velocity structure, especially when the fitting is performed with small triangular sub-arrays. For example, we observe velocities larger than 8 km/s just east of the Sierra Nevada in Figure 3.4, compared to the more muted changes in the tomography image (Figure 3.11). The localization images show overall higher-amplitude anomalies. It is likely that the travel-time tomography underestimates the amplitude of velocity structures because of damping in the inversion.

Plane and circular wave-front methods show very similar results, the small changes in individual measurements do not appear in maps with averaged velocities because of generally large scatter in the measured apparent velocities. We found that for many traces in our data set the Pn arrivals are hard to pick and cross-correlate due to their low signal-to-noise ratios. The inclusion of wavefront curvature may have a larger effect in different regions, perhaps in areas with more impulsive Pn arrivals that would lead to more accurate timing. The addition of terms that account for Moho topography and anisotropy have a larger influence on the mapped velocity anomalies. As expected, localization images resulting from larger sub-arrays that average over larger regions agree better with the smoothed traditional tomography images.

Consistent with the older Pn tomography study by *Hearn* [1996] and our newer version with realigned USArray data, the localization results show a large low-velocity region below the Snake River Plain, but the anomaly is strongest west of the current location of the Yellowstone hotspot. Contrary to new P-velocity map slices in the lithosphere [*Schmandt and Humphreys*, 2010; *Obrebski et al.*, 2011; *Tian and Zhao*, 2012],

the slow velocities are not concentrated around the hotspot location, but spread over the Snake River Plain. This is observed even in our localization maps from triangular sub-arrays. The traditional tomography approach shows an anomaly that fades somewhat toward the northeast. However this could be an artifact of reduced ray coverage below Yellowstone, or off-great-circle-path arrivals, as the localization maps show consistent slow velocities. It would be interesting to apply 2D ray tracing to model the deviations of the directions of the incoming wavefronts due to changes in velocity structure, information that could be compared to the ray angles obtained from the localization method and possibly also included to improve ray tracing in travel-time tomography, but we defer this to planned future work.

We observe consistent very low mean Pn velocities below the Sierra Nevada and azimuthal anisotropy with fault-parallel fast directions. As discussed in *Hearn* [1999], velocities much lower than 7.8 km/s may be associated with mantle material that contains a small amount of partial melt. Several factors, however, can influence the measured apparent velocities, for example an increased crustal thickness because of a mantle root, a dipping Moho, cross-correlation alignments on refractions from a shallower layer, multipathing, or a combination of these effects. It seems inevitable that there are trade-offs between the various parameters, and is is difficult to distinguish between geometrical, compositional, and thermal effects.

Jones et al. [1994] found slow Pn velocities (7.6–7.65 km/s) below the southern Sierra Nevada, and discuss the possibility of a two-layer structure that includes an additional refractor with a P-wave velocity greater than about 7.2 km/s. *Savage et al.* [1994] found further evidence for this intermediate layer. The subtraction of station delays from the differential times increases the apparent velocity below the Sierra Nevada in our maps (compare Figure 3.5 and Figure 3.6) to about 7.6 km/s as well. Station terms might not only absorb crustal velocity anomalies below stations, but also changes in crustal thickness. Both the delay terms from traditional tomography and the localization site terms are largest at stations located at the eastern border of the mountain range. Further analysis that could include Pn and Sn amplitude measurements to locally resolve attenuation structure (but working with these amplitudes is difficult, see *Bakir and Nowack* [2011] for the complex behavior of Pn amplitudes), as well as combined Pn/Sn travel time inversions to estimate Vp/Vs ratios, might help constrain material and temperature properties.

Localization anisotropy measurements largely agree with fast-direction estimates from traditional Pn tomography, in particular the mostly fault-parallel Pn fast axis in central California, indicating that the anisotropy is caused by shearing along the plate boundary. As discussed in greater detail in *Buehler and Shearer* [2010], these fast directions are complementary to fast polarization directions obtained in recent USArray shear-wave splitting studies [*Liu*, 2009; *West et al.*, 2009]. The SKS fast polarization direction show a distinct cylindrical pattern around small splitting times in the central Great Basin. In addition, USArray P-wave tomographic models show an almost vertical high velocity anomaly in the region with small splitting times [*Roth et al.*, 2008] ranging from a depth of about 75 km to at least 500 km that can be interpreted as a result of a lithospheric drip [*West et al.*, 2009]. Figure 3.8 and 3.9 of this study suggest low velocities in central Nevada in the uppermost mantle, bounding the vertical high velocity anomaly imaged by *Roth et al.* [2008]. Pn fast axes from both tomography and localization show a less distinct rotation, and anisotropy is stronger in northern than southern Nevada. This observation suggests that the orientation of azimuthal anisotropy changes in the upper mantle as shear-wave splitting measurements provide a vertically integrated measure of anisotropy in the upper mantle. We plan to apply similar methods to Sn-SV and Sn-SH to solve for radial and azimuthal anisotropic parameters. This would allow us to compare our observations to seismic anisotropy predicted by aligned olivine models that are believed to be the dominant cause of upper-mantle anisotropy.

In conclusion, we demonstrate an alternative method to traditional Pn travel-time tomography to regionally image uppermost-mantle velocity structure and anisotropy. The dense station network of USArray provides a chance to apply simple array tools to regional scale investigations. The localization approach does not depend on regularization, and therefore has the capacity to map velocity structure with increased resolution and with more reliable amplitudes. Our localization maps generally show stronger anomalies compared to travel-time tomography images, which is important to consider, for example, in mantle temperature calculations. Similar localized approaches can be applied to Sn, and critically or nearly critically refracted crustal phases. This analysis should provide a more complete picture of crust and uppermost mantle structure at well-defined depths.

Acknowledgments

We thank the USArray Array Network Facility for making their picking information available. Luciana Astiz assisted with many ANF database related questions. Many of the figures where produced with the GMT software (*Wessel and Smith* [1995]). We thank Tom Hearn and an anonymous referee for constructive reviews of this manuscript. This research was supported by grant EAR-0950391 from the National Science Foundation. Chapter 3, in full, is a reprint of the material as it appears in Buehler, J. S. and P. M. Shearer, Localized imaging of the uppermost mantle with USArray Pn data, Journal of Geophysical Research: Solid Earth, 117(B9), 2012. The dissertation author was the primary investigator and author of this paper.

References

Almendros, J., J. M. Ibanez, G. Alguacil, and E. Del Pezzo (1999), Array analysis using circular-wave-front geometry: An application to locate the nearby seismo-volcanic source, *Geophysical Journal International*, *136*(1), 159–170.

Bakir, A. C., and R. L. Nowack (2011), Modeling Seismic Attributes of Pn Waves using the Spectral-Element Method, *Pure and applied geophysics*, *169(9)*, 1539–.

Buehler, J. S., and P. M. Shearer (2010), Pn tomography of the western United States using USArray, *J. Geophys. Res.*, *115*(B9), B09,315–.

Burdick, S., et al. (2008), Upper Mantle Heterogeneity beneath North America from Travel Time Tomography with Global and USArray Transportable Array Data, *Seismological Research Letters*, *79*(3), 384–392.

Burdick, S., et al. (2010), Model Update January 2010: Upper Mantle Heterogeneity beneath North America from Traveltime Tomography with Global and USArray Transportable Array Data, *Seismological Research Letters*, *81*(5), 689–693.

Burdick, S., et al. (2012), Model Update March 2011: Upper Mantle Heterogeneity beneath North America from Traveltime Tomography with Global and USArray Transportable Array Data, *Seismological Research Letters*, *83*(1), 23–28.

Christensen, N. I. (1984), The magnitude, symmetry and origin of upper mantle anisotropy based on fabric analyses of ultramafic tectonites, *Geophysical Journal Of The Royal Astronomical Society*, *76*(1), 89–111.

Earle, P. S., and P. M. Shearer (1994), Characterization of global seismograms using an automatic-picking algorithm, *Bulletin of the Seismological Society of America*, *84*(2), 366–376.

Goes, S., and S. van der Lee (2002), Thermal structure of the North American uppermost mantle inferred from seismic tomography, *Journal Of Geophysical Research-Solid Earth*, *107*(B3).

Hearn, T. M. (1996), Anisotropic Pn tomography in the western United States, *Journal Of Geophysical Research-Solid Earth*, *101*(B4), 8403–8414.

Hearn, T. M. (1999), Uppermost mantle velocities and anisotropy beneath Europe, *Journal Of Geophysical Research-Solid Earth*, *104*(B7), 15,123–15,139.

Jones, C. H., H. Kanamori, and S. W. Roecker (1994), Missing roots and mantle and drips: Regional Pn and teleseismic arrival times in the southern Sierra Nevada and vicinity, California, *J. Geophys. Res.*, *99*(B3), 4567–4601.

Karlstrom, K. E., and E. D. Humphreys (1998), Persistent influence of Proterozoic accretionary boundaries in the tectonic evolution of southwestern North America, *Rocky Mountain Geology*, *33*(2), 161–179.

Lin, F.-C., and M. H. Ritzwoller (2011), Helmholtz surface wave tomography for isotropic and azimuthally anisotropic structure, *Geophysical Journal International*, *186*(3), 1104–1120.

Lin, F.-C., M. H. Ritzwoller, and R. Snieder (2009), Eikonal tomography: surface wave tomography by phase front tracking across a regional broad-band seismic array, *Geophysical Journal International*, *177*(3), 1091–1110.

Lin, G., P. M. Shearer, E. Hauksson, and C. H. Thurber (2007), A three-dimensional crustal seismic velocity model for southern California from a composite event method, *J. Geophys. Res.*, *112*(B11), B11,306–.

Liu, K. H. (2009), NA-SWS-1.1: A uniform database of teleseismic shear wave splitting measurements for North America, *Geochem. Geophys. Geosyst.*, *10*.

Moschetti, M. P., M. H. Ritzwoller, F.-C. Lin, and Y. Yang (2010), Crustal shear wave velocity structure of the western United States inferred from ambient seismic noise and earthquake data, *J. Geophys. Res.*, *115*(B10), B10,306–.

Obrebski, M., R. M. Allen, F. Pollitz, and S.-H. Hung (2011), Lithosphere-asthenosphere interaction beneath the western United States from the joint inversion of body-wave traveltimes and surface-wave phase velocities, *Geophysical Journal International*, *185*(2), 1003–1021.

Perry, H. K. C., C. Jaupart, J. . C. Mareschal, and N. M. Shapiro (2006), Upper mantle velocity-temperature conversion and composition determined from seismic refraction and heat flow, *Journal of Geophysical Research-Part B-Solid Earth*, p. 14 pp.

Pezzo, E. D., and F. Giudicepietro (2002), Plane wave fitting method for a plane, small aperture, short period seismic array: a MATHCAD program, *Comput. Geosci.*, *28*(1), 59–64.

Pollitz, F. F., and J. A. Snoke (2010), Rayleigh-wave phase-velocity maps and three-dimensional shear velocity structure of the western US from local non-plane surface wave tomography, *Geophysical Journal International*, *180*(3), 1153–1169.

Raitt, R. W., G. G. Shor, T. J. G. Francis, and G. B. Morris (1969), Anisotropy of Pacific upper mantle, *Journal Of Geophysical Research*, *74*(12), 3095–&.

Roth, J. B., M. J. Fouch, D. E. James, and R. W. Carlson (2008), Three-dimensional seismic velocity structure of the northwestern United States, *Geophysical Research Letters*, *35*(15).

Savage, M. K., L. Li, J. P. Eaton, C. H. Jones, and J. N. Brune (1994), Earthquake refraction profiles of the root of the Sierra Nevada, *Tectonics*, *13*(4), 803–817.

Schmandt, B., and E. Humphreys (2010), Complex subduction and small-scale convection revealed by body-wave tomography of the western United States upper mantle, *Earth and Planetary Science Letters*, *297*, 435–445.

Steck, L. K., M. L. Begnaud, S. Phillips, and R. Stead (2011), Tomography of crustal P and S travel times across the western United States, *Journal Of Geophysical Research-Solid Earth*, *116*, B11,304.

Sun, D. Y., and D. Helmberger (2011), Upper-mantle structures beneath USArray derived from waveform complexity, *Geophysical Journal International*, *184*(1), 416–438.

Tian, Y., and D. Zhao (2012), P-wave tomography of the western United States: Insight into the Yellowstone hotspot and the Juan de Fuca slab, *Physics of the Earth and Planetary Interiors*, *200–201*(0), 72–84, doi:10.1016/j.pepi.2012.04.004.

Vandecar, J. C., and R. S. Crosson (1990), Determination Of Teleseismic Relative Phase Arrival Times Using Multi-Channel Cross-Correlation And Least-Squares, *Bulletin Of The Seismological Society Of America*, *80*(1), 150–169.

Wessel, P., and W. H. F. Smith (1995), New version of the generic mapping tools, *Eos Trans. AGU*, *76*(33), 329–329.

West, J. D., M. J. Fouch, J. B. Roth, and L. T. Elkins-Tanton (2009), Vertical mantle flow associated with a lithospheric drip beneath the Great Basin, *Nature Geoscience*, *2*(6), 439–444.

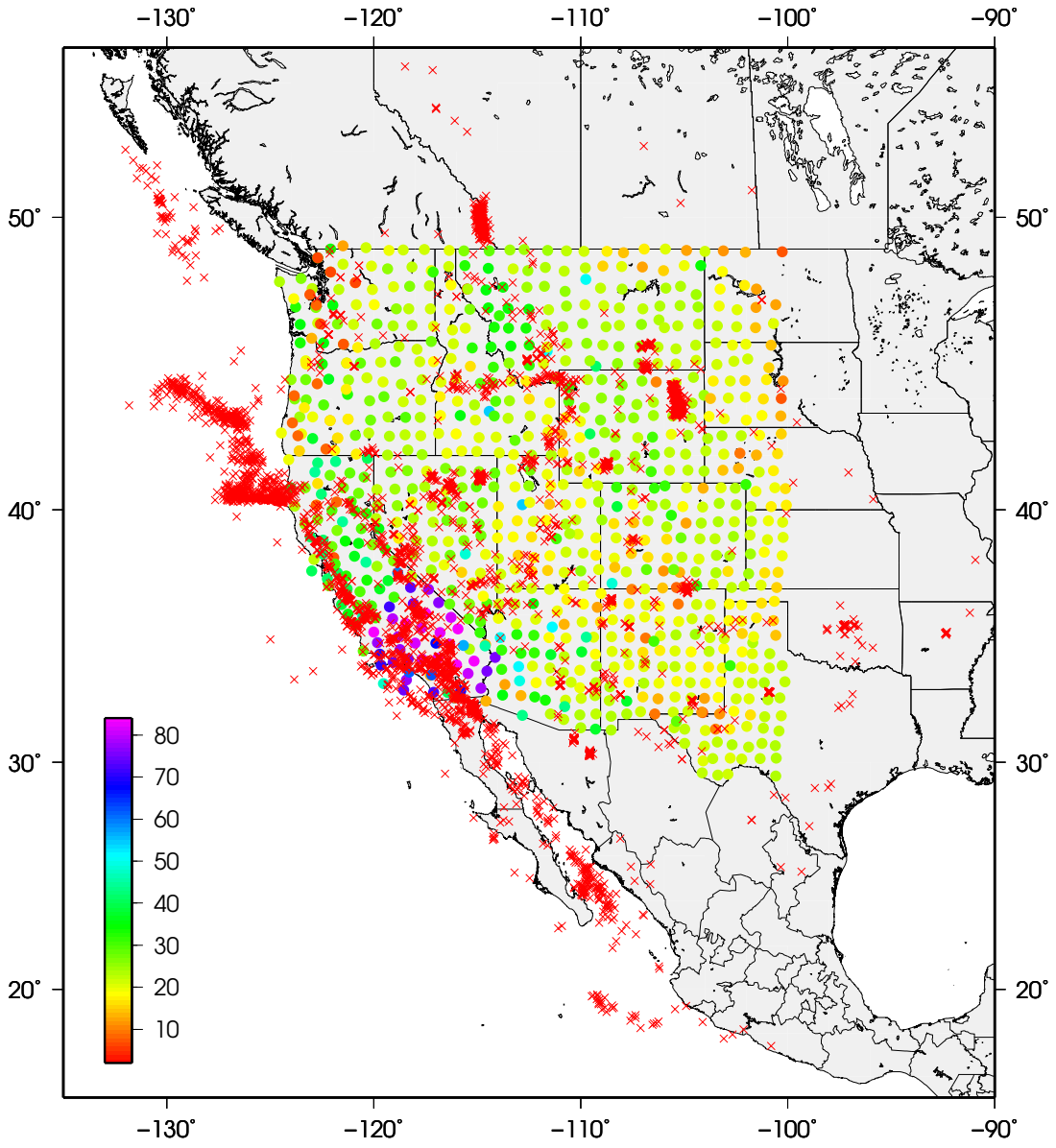

Figure 3.1: Overview map showing the study region, the final set of events (red crosses) used in the travel time tomography as well as the localization approach, and the station locations (colored circles). The stations are color coded by the number of months data from our time period was recorded at that receiver.

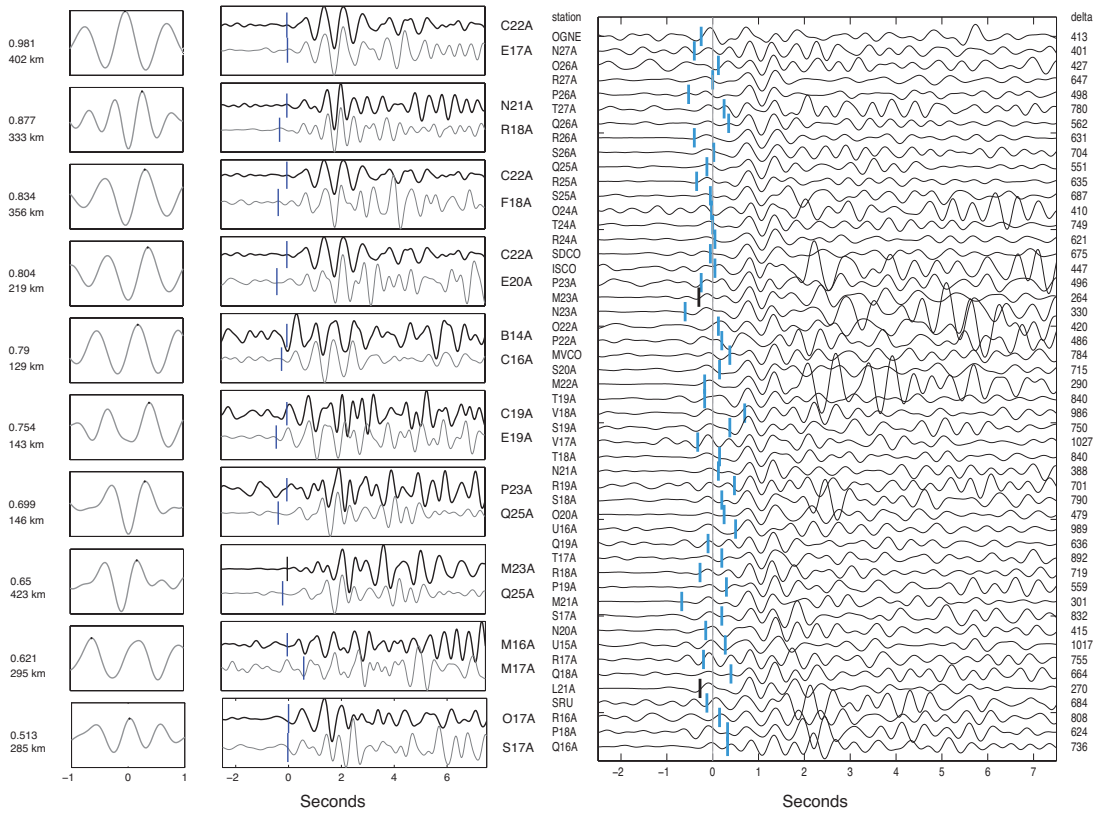

Figure 3.2: Sample cross-correlations. The left two columns contains the correlation functions and the corresponding cross-correlated and shifted seismograms. The correlation coefficients and inter-station distances are noted in the far left. The tick marks indicate the picks. The right column shows a selection of the realigned seismograms. The realigned times are obtained by fitting the measured differential times from cross-correlation. The amplitudes are scaled according to energy in the correlation window for better comparison. In this figure all but two of the picks are from the auto-picker (blue ticks).

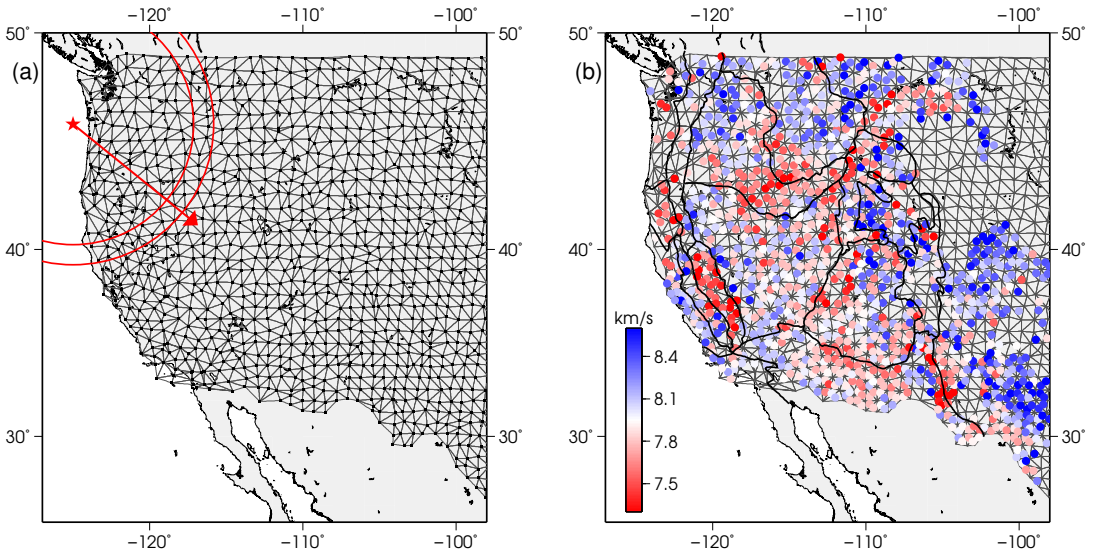

Figure 3.3: a) USArray stations divided into triangles with a Delaunay tesselation (black lines). At each triangle, we solve for the direction and velocity of incoming wavefronts. b) The colored circles shows the mean measured velocity at each triangle. For some triangles, there are not enough good differential times to obtain a velocity measurement, especially in regions east of 110° W. No circle is plotted in triangles with fewer than five velocity measurements.

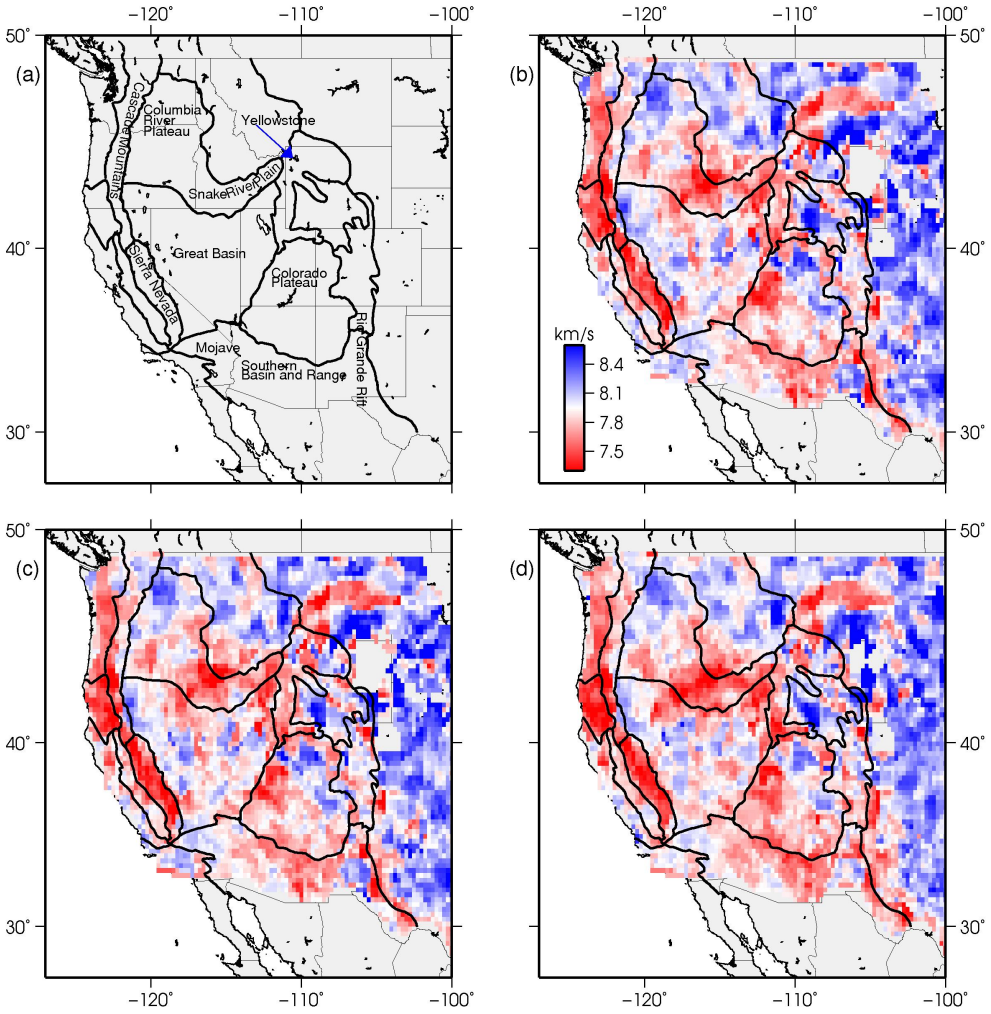

Figure 3.4: Localization approach with station triangles. Delaunay triangularization is applied separately to every event data set, and parameter estimates are stored in an underlying two-dimensional 0.25° x 0.25° grid. Plotted are the average values at each location. a) Overview map with geological provinces. b) Localization result assuming a planar wavefront, except at ranges smaller than 500 km where we fit a circular wavefront from a fixed epicenter. c) Accounting for curvature with circular wavefront fits. d) Same as c) but with self-consistent realigned relative arrival times.

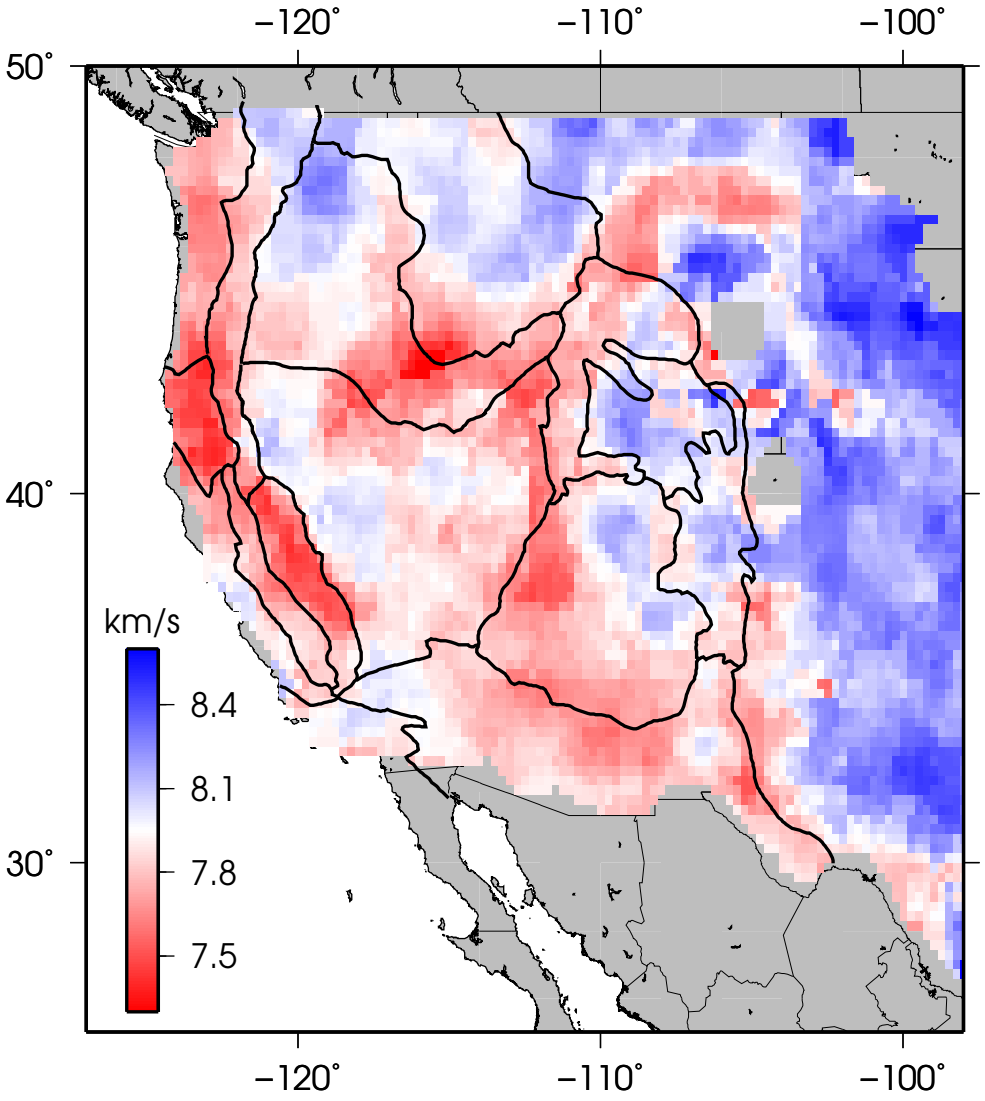

Figure 3.5: Local velocity estimates from larger sub-array polygons that contain at least three station triangles. This provides a smoother image with similar large-scale features as obtained with tripartite arrays.

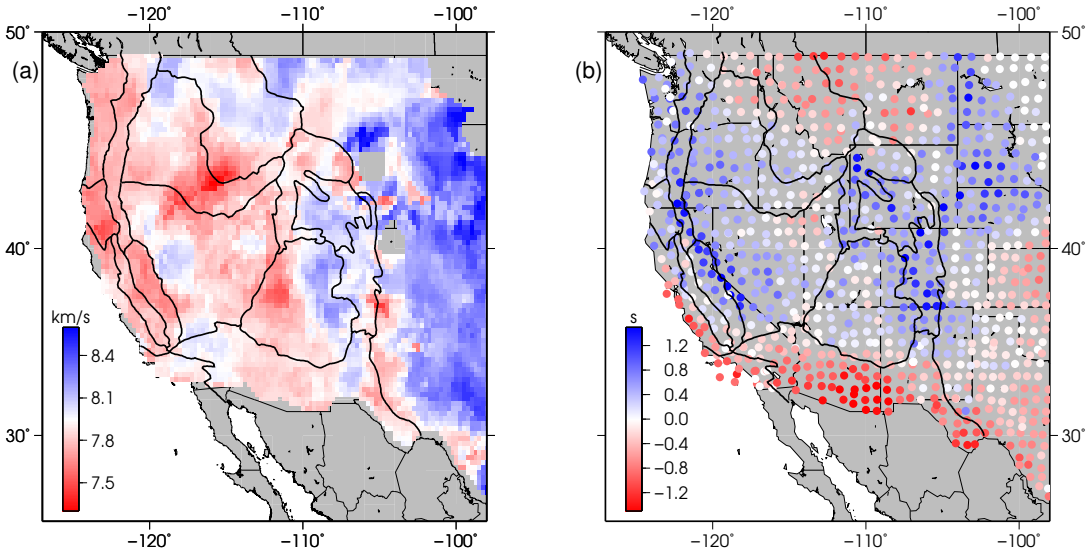

Figure 3.6: a) Local velocity estimates from larger sub-array polygons that contain at least three station triangles with differential times that are corrected for station delays. b) Station time terms in seconds. Station terms might absorb crustal velocity anomalies below stations and changes in crustal thickness. Compare these terms to the station time terms obtained from traditional Pn tomography (Figure 3.11b).

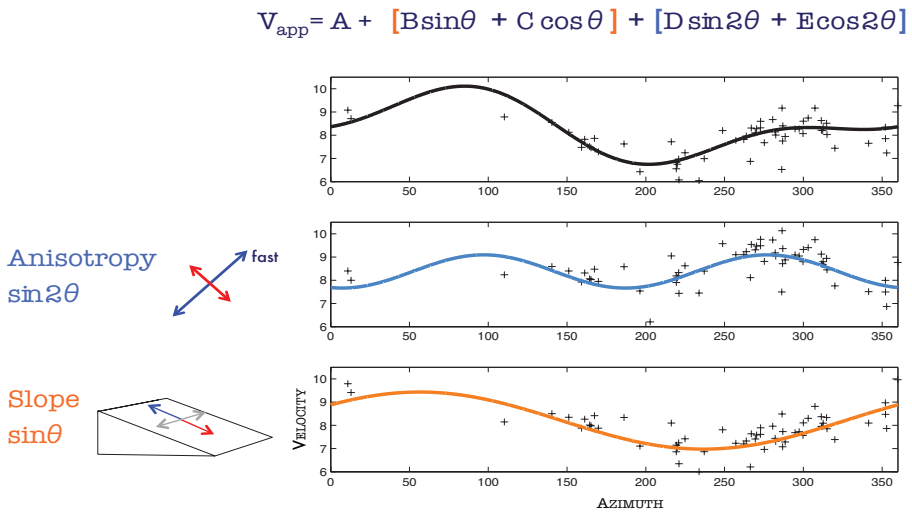

Figure 3.7: Example of using azimuthal velocity variations to solve for Moho slope and azimuthal anisotropy. Moho slope and anisotropy influence the observed apparent velocity. We fit curves described by the equation on the top to the measured velocity distribution with azimuth to take these effects into account.

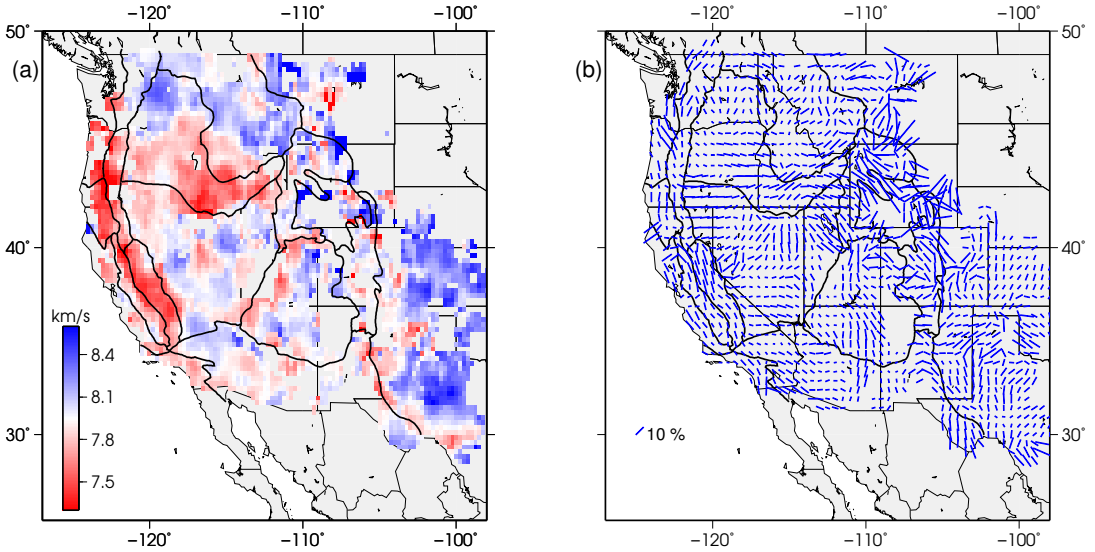

Figure 3.8: Moho slope and anisotropy influence the observed apparent velocity. We fit curves to the measured velocity distribution with azimuth to take these effects into account. a) The isotropic velocities after accounting for moho slope and anisotropy, and b) the fast directions and strength of anisotropy (scaling with line length). Velocities and azimuths are measured using triangular station subsets, and without the addition of station terms.

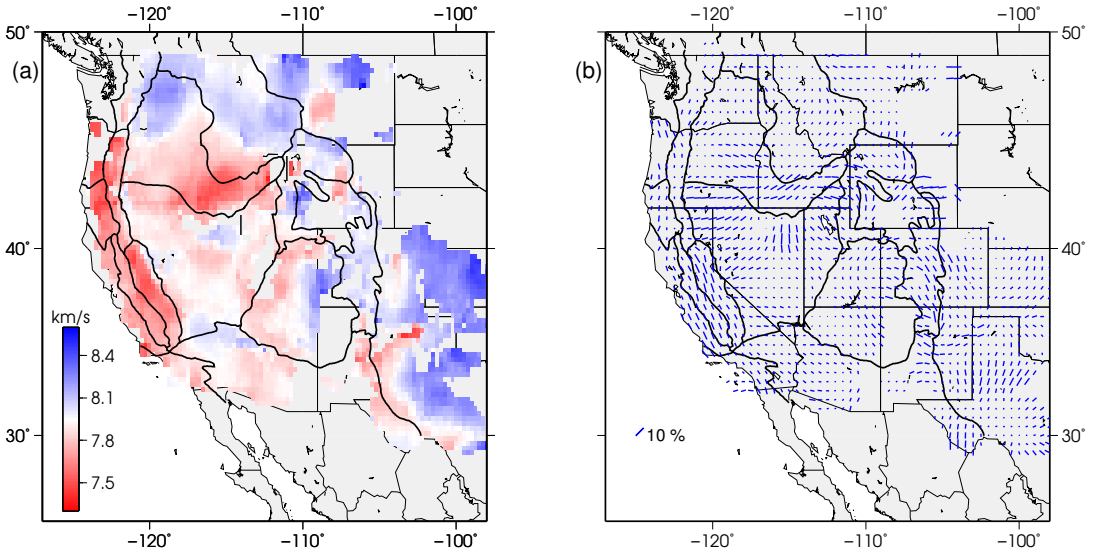

Figure 3.9: a) The isotropic velocities after accounting for moho slope and anisotropy, and b) the fast directions and strength of anisotropy (scaling with line length). Velocities and azimuths are measured using station pentagons with five or more receivers, and the differential times were corrected for station delays.

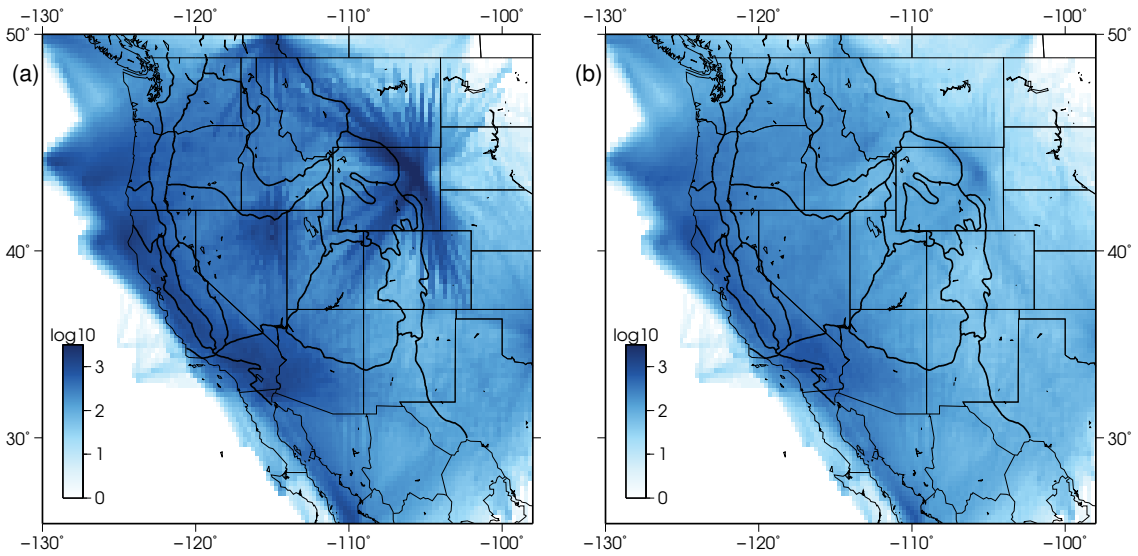

Figure 3.10: Ray count per cell for the traditional Pn tomography: a) with the whole data set and b) after removing data on much traveled paths.

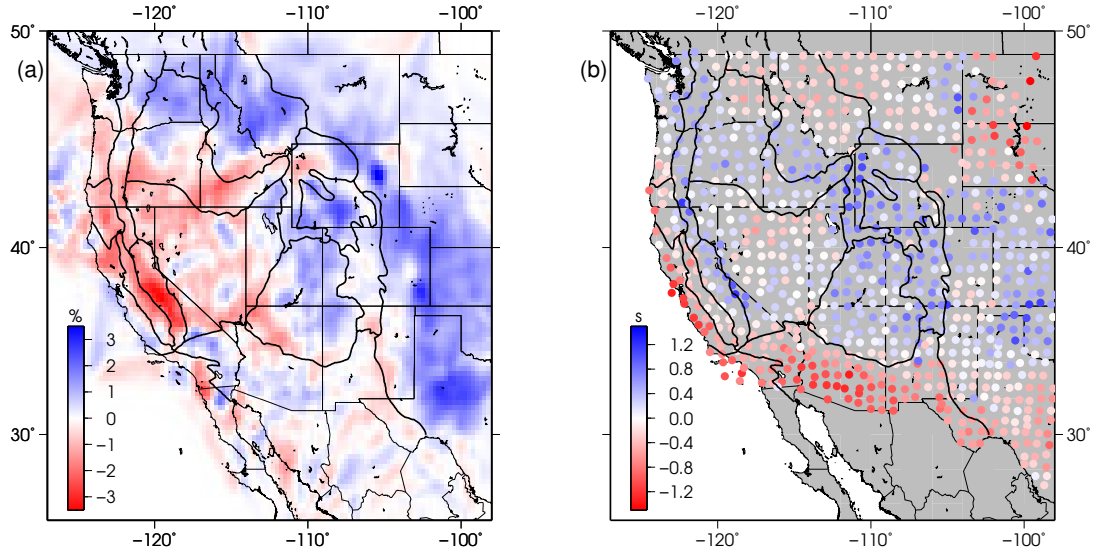

Figure 3.11: a) Isotropic velocities obtained from a two dimensional Pn travel time tomography using realigned picks. The average velocity is 7.91 km/s. b) Station time terms in seconds. The station terms should account for the time it takes the ray to travel from the mantle pierce point to the receiver. With the assumption of a crustal velocity, Moho depths can be estimated. Positive station terms indicate a thicker crust, negative terms a thinner crust.

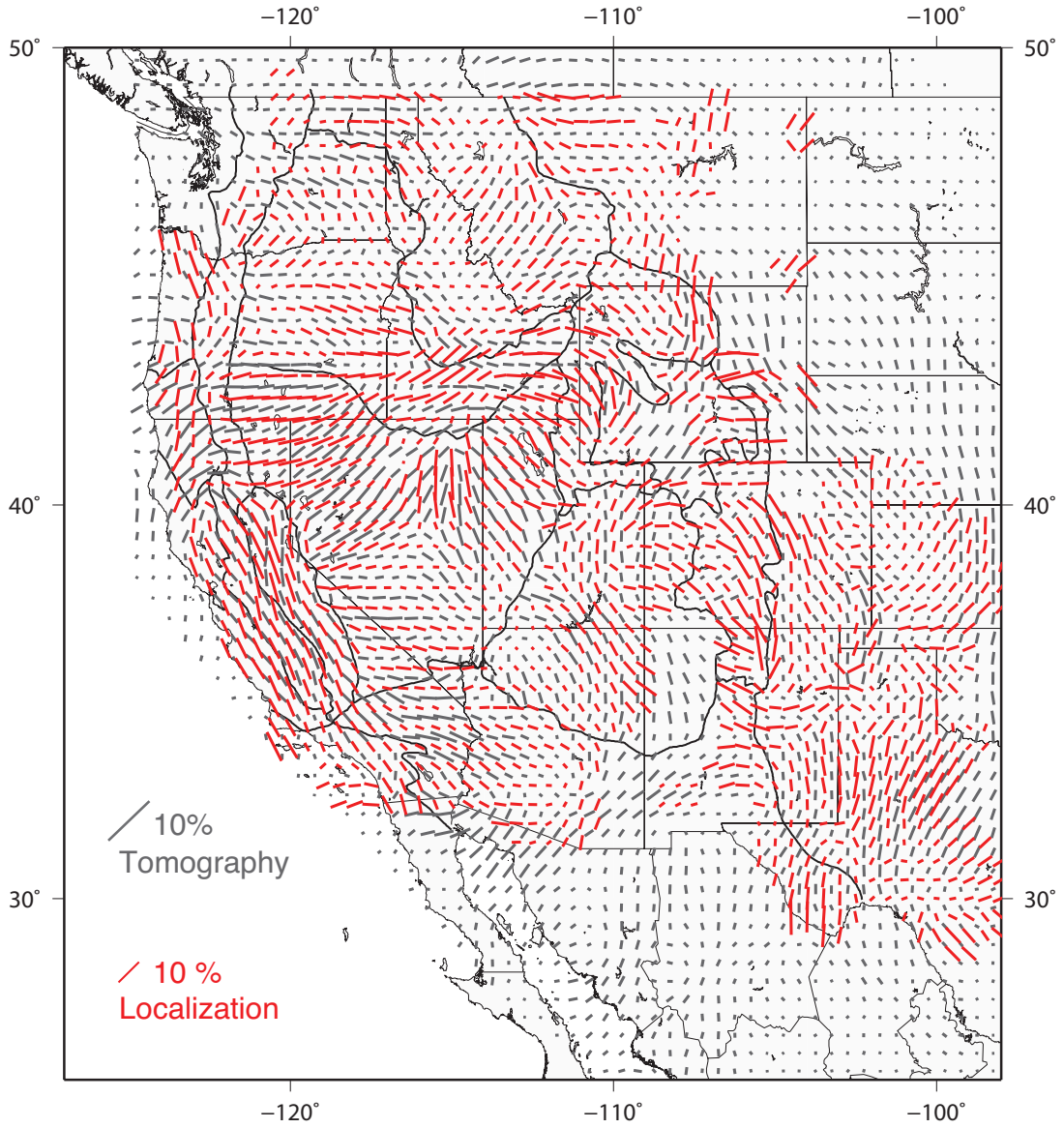

Figure 3.12: Pn fast axis obtained from localization with station pentagons (red) and traditional travel time tomography (gray). The traditional travel-time tomography results generally show weaker anisotropy. For visibility, the fast axes from the tomography are multiplied by a factor of two.

Chapter 4

Sn Propagation in the Western United States from Common Mid-Point Stacks of USArray Data

The regional seismic phase Sn propagates horizontally in the uppermost mantle and is sensitive to lateral variations in mantle lid thickness, temperature and melt. Sn is therefore often used as an indicator for physical properties of the lithosphere. It has previously been noticed that Sn is not observed at many stations in the western United States and Sn seems especially highly attenuated for paths across the Basin and Range. Here we apply stacking methods to USArray data to identify highly attenuating regions in the uppermost mantle and increase the spatial resolution of the Sn propagation image. We find evidence for Sn propagation at short ranges in the central Great Basin and the northeastern part of the Colorado Plateau, both regions where lithospheric stability and thickness is debated, and observe strong Sn attenuation around the perimeter of the central Great Basin.

4.1 Introduction

We investigate high-frequency propagation of the regional phase Sn in the western United States. Sn propagates horizontally in the uppermost mantle just below the Moho

and is often modeled as a head-wave. Sn has been used for velocity and attenuation studies focused on the uppermost mantle [e.g., *Diaz et al.*, 2013; *Goek et al.*, 2003; *Pei et al.*, 2007]. However, Sn has been observed to travel to teleseismic distances across oceanic paths, and is more broadly defined as a channel wave that travels in the mantle lid above the low-velocity zone of the upper mantle [*Molnar and Oliver*, 1969; *Stephens and Isacks*, 1977]. A waveguide can be formed if the shear-wave velocity increases with depth from the Moho to the top of the low-velocity zone. Several factors influence the propagation of Sn, among them the upper-mantle shear-wave velocity gradient [*Stephens and Isacks*, 1977], but also the thickness and thermal state of the lithosphere [*Beghoul et al.*, 1993]. Therefore, studies of Sn propagation can be used to help constrain regional tectonic models [e.g., *Barron and Priestley*, 2009; *Beghoul et al.*, 1993; *Calvert et al.*, 2000; *Ni and Barazangi*, 1983].

Starting with the USArray station deployment, great efforts have been made to investigate and image lithospheric structure below the western United States with various data sets and new methods to better understand the tectonic evolution of the continent. Tomographic images from body- and surface-wave data show very heterogeneous velocity structure in the upper mantle in the western United States [e.g., *Lin et al.*, 2011; *Obrebski et al.*, 2011; *Schmandt and Humphreys*, 2010]. Prominent local low-velocity anomalies imaged below the Snake River Plain and the southwestern Colorado Plateau likely reflect higher temperatures due to volcanism. Waves that travel horizontally in the uppermost mantle will be strongly affected by these lateral anomalies. Higher temperatures should also increase seismic attenuation, which will affect Sn more than the P-wave analogue, Pn, as S-wave mantle attenuation is observed to be stronger than P-wave attenuation. Generally, Sn traverses well through stable continental regions but is attenuated in more tectonically active regions, and *Beghoul et al.* [1993] concluded in their study on regional phase propagation that Sn does not propagate across the majority of the western United States. However, *Beghoul et al.* [1993] also did not observe Sn for paths that cross below the relatively stable Colorado Plateau (Figure 4.1).

In regions where the mantle lid is thin or missing, as for example through delamination processes that cause local upwelling of the asthenosphere, a process that may explain the elevation of the Colorado Plateau [e.g., *Levander et al.*, 2011], Sn will be strongly attenuated by the hotter material. Studies showed that the lithosphere is relatively thin for large portions of the western United States: *Goes and van der Lee*

[2002] estimated the lithosphere to be as thin as 50 km below the Basin and Range province. *Beghoul et al.* [1993] estimated the mantle lid thickness to be about 20–40 km below the same region (adding a 20–30 km thick crust to compare to lithospheric thickness), and found no evidence for Sn in seismograms for paths that cross the Great Basin. However, more recent tomographic studies that profit from the USArray station network show finer scale structure and possible drip features in the Great Basin that could locally increase lithospheric thickness [*West et al.*, 2009].

In this study we use the dense USArray transportable network to investigate the propagation of the Sn phase. Previous research showed that at large scales Sn is strongly attenuated in regions west of the Great Plains (*Beghoul et al.* [1993], Figure 4.1). However, we find that there are a number of Sn picks in the database of the Array Network Facility (ANF) for stations west of the Great Plains, and an initial time-term analysis with these picks showed that they are viable for tomography, as they produce similar large-scale features as Pn tomography maps. Many of these Sn picks have relatively short epicentral distances ($< 6^{\circ}$), suggesting that the regions of Sn blockage are similar in scale to the velocity structures observed in the upper mantle.

We apply stacking methods, similar to those employed locally in active-source studies, on a regional scale using both earthquakes and quarry blasts, and measure the Sn amplitudes of these stacks at various locations. This allows us to map overall Sn propagation efficiency over large regions and image highly attenuating regions, but without the need to inspect individual seismograms or the complications of formal attenuation modeling. We find evidence in our stacks for transmission of Sn below the northwestern portion of the Colorado Plateau, and in the center of the Great Basin, areas that coincide with regions of higher seismic velocities. As expected, we find Sn to be highly attenuated in the belt associated with recent volcanism and high heat-flow that surrounds the central portion of the Great Basin and includes the Cascades Back-Arc, the Snake River Plain, and the southwestern margin of the Colorado Plateau.

4.2 Methods

Sn is often emergent, buried by P-wave coda, and hard to see by eye in individual seismograms. Stacking methods can greatly enhance such weak arrivals [e.g., *Richards-Dinger and Shearer*, 1997]. Common mid-point stacks are typically applied in seismic reflection experiments, but a similar approach can be used with refracted arrivals to

obtain information on average seismic properties within a certain region [*Behm et al.*, 2007]. Here we stack seismograms that have the mid-point of their ray-paths within a common two-dimensional cell. We then measure Sn amplitudes in these stacks to investigate variations in propagation efficiency or blockage at the various locations of the common mid-point cells.

We downloaded waveforms from the ANF for about 8000 earthquakes and quarry blasts for broadband channels that have at least ten Pn or Sn picks remaining after applying a similar space-time windowing procedure to that described in *Buehler and Shearer* [2010]. The ray paths for the stacks span ranges from 1.8° to 12°. We did not remove the instrument response since all the USArray transportable array stations are equipped with very similar instruments. We rotate the raw horizontal velocity seismograms into radial and transverse components using the epicenter location provided by the ANF, and filter the waveforms between 0.8 and 4 Hz to remove microseisms and high-frequency noise.

We proceed in similar fashion to that described in *Behm et al.* [2007]: We shift an equal area square cell with a width of 1.6° in increments of 0.8° across the western United States. At each location, we find the event and station combinations that have their range mid-point within the window. Figure 4.2 shows an example for a common mid-point cell in the Great Basin. We stack all traces that satisfy this condition and that have a minimum signal to noise ratio of 2.5 for the first arriving Pn phase on the vertical component. Since we cannot expect waveform coherency for the earthquakes from various ranges and azimuths around the common mid-point cell we find that stacking the short-term-average to long-term-average (STA/LTA) function of the waveforms works well [*Astiz et al.*, 1996]. We use one and ten seconds for the short and long term windows, respectively. For stacking we use 0.25° for the range bin size, and 0.5 seconds for the time bins (see supplementary material).

Similar to *Behm et al.* [2007] we find that the traces collected in individual distance bins stack with greater coherency if we align the Sn arrivals by means of a reduction velocity. For each stack, we find the average uppermost mantle Pn velocity and crustal thickness from our tomography [*Buehler and Shearer*, 2010] within the common mid-point cell. From this information we estimate an average slowness and intercept time for Sn at that location, assuming constant crustal velocity and Vp/Vs in the uppermost mantle. We then adjust the timing of the seismograms according to these parameters, in

order for Sn to align at approximately zero time. We found that a more sophisticated approach with individual station and event time-terms does not increase coherency, and that the 0.5 second time bins are large enough to counteract small misalignments.

Working with STA/LTA functions of seismograms is convenient, as the process functions as automatic gain control and often nicely enhances the appearance of individual phases. However, the shape of the waveforms is not conserved, and STA/LTA functions might bias the results, as more impulsive arrivals could map into a higher amplitude in the stacks. Therefore we also produce common mid-point stacks using the envelope function of the seismograms for comparison (Figure 4.2b). We then use both, the STA/LTA and the envelope stacks, to measure the Sn amplitude. To properly capture the Sn signal strength we measure the rms amplitudes using a 10 s window that starts 4 s before the estimated Sn arrival-time for the bins between a range of 3.25° and 4°. At certain locations Sn appears stronger at greater ranges, so we therefore also shift the amplitude measuring window along the range axis in 0.25° increments and measure the maximum signal at any range between 3.25° and 8°. This reduces the localization and makes interpretation more difficult, but indicates the general visibility of Sn in a stack more clearly. Often Sn appears stronger at shorter ranges, but here we risk that the Sn phase amplitude is contaminated by energy of crustal Lg. However, since energy transfer between Sn and the crustal phase can occur, especially at continental margins [*Isacks and Stephens*, 1975] and possibly continental plateaus, we separately measure the rms amplitude of Lg using a similar window. We normalize both the measured Sn and Lg amplitudes with the rms amplitude of a window in the P-coda.

This simple waveform stacking approach is unable to return high resolution attenuation images as for example produced by *Phillips and Stead* [2008] for USArray Lg. Attenuation tomography for Sn is difficult since the phase is generally only well approximated as a head-wave that travels horizontally right below the Moho at short ranges [e.g., *Sereno*, 1989]. At longer ranges, Pn and Sn generally evolve into turning waves, and modelling them as pure head-waves with a horizontal uppermost mantle path introduces errors. The ranges over which this transition occurs depend on the velocity gradient in the mantle lid and on the crustal thickness [*Sereno*, 1989]. The type of head-wave that is observed up to teleseismic distances is typically described as a sum of whispering gallery or interference waves which travel in the mantle lid between the Moho and the low-velocity zone of the upper mantle [e.g., *Menke and Richards*, 1980].

Attenuation behavior of such waves is generally quite complicated and different from the behavior of pure head-waves, and the amplitudes will depend on the velocity gradient in the uppermost mantle [*Hill*, 1973; *Braile and Smith*, 1975]. Because of these complications we don't attempt to formally model the Sn attenuation, but try to determine the broad variations of the propagation efficiency. The method we apply allows us to process a large number of seismic observations from USArray, and improves the available model of Sn propagation efficiency in the western United States.

4.3 Results

Figure 4.3 displays the measured stack amplitudes and Figure 4.4 shows corresponding stacks for various locations for the transverse components. Images for the radial component are not displayed but look similar. The results from the STA/LTA and envelope stacks show similar features although the structures in the envelope map are less distinct (compare Figure 4.3a with 4.3c). This is to be expected as the STA/LTA filter is more sensitive to changes in the shape and amplitude of the signal. Note that strong P-arrivals are visible on the transverse component as a result of this filter sensitivity. Measuring amplitudes with just one range window at 3.25° and 4° seems to capture the characteristics of the stacks well, except for a few regions, as for example north of the Colorado Plateau, where Sn is visible more clearly at larger distances (Figure 4.3b).

Similar to observations of seismic velocities, the Sn amplitude structure is quite heterogeneous. As in *Rodgers et al.* [1997] the measured rms Sn amplitudes are typically lower in regions of low Pn velocities. We find the most distinctive zone without evidence for Sn propagation in the back-arc of the Cascade Range, a region with recent volcanism. Similarly, we do not observe Sn in stacks across the Snake River Plain and the current location of the Yellowstone hotspot, regions of low Pn velocities (Figure 4.3d, updated model from *Buehler and Shearer* [2010]) and very low shear velocities [*Schmandt and Humphreys*, 2010]. These observations could indicate zones of partial melt in the uppermost mantle. To the north of the Snake River Plain and Yellowstone the character of the stacks changes abruptly and Sn is clearly visible in the stacks. We also find clear Sn arrivals in the region of the Columbia Plateau, where recent receiver function analysis showed a local increase in the depth of the lithosphere-asthenosphere boundary [*Kumar et al.*, 2012].

We don't observe Sn in the transition zone between the Great Basin and the

Colorado Plateau. The Basin and Range province is associated with high heat flow [e.g., *Lachenbruch*, 1978] that is generally related to strong Sn attenuation [*Molnar and Oliver*, 1969]. Yet interestingly we see a region of Sn propagation in the center of the Great Basin, in the broad region of a previously imaged higher velocity body interpreted as a lithospheric drip [*West et al.*, 2009], and close to the low heat flow anomaly in south-central Nevada [*Lachenbruch*, 1978]. *West et al.* [2009] explain that the downwelling would locally increase the thickness of the lithosphere and potentially reduce its thickness around the periphery of the Great Basin. It is current understanding that the mantle lid of lithosphere needs to be sufficiently thick in order for Sn to propagate. However, at the relatively short epicentral distances over which we measure the amplitudes the phase should propagate near the top of the mantle similar to a pure head-wave. Still, the stacks show a clear Sn strand to a range of about six degrees (Figure 4.4, stack 3) before the phase fades, supporting the existence of a locally colder and possibly thicker lithosphere.

The previous study by *Beghoul et al.* [1993] showed that Sn does not propagate across the Colorado Plateau. They argued that the absence of Sn indicates a thin mantle lid since the Pn velocities below the central Colorado Plateau are relatively high, and therefore Sn attenuation is likely not caused by thermal effects. Their study used WWSSN stations and the ray paths were between 3 and 16 degrees. Since the station network was much sparser pre-USArray, many of the Sn paths analyzed traveled across the entire Colorado Plateau. In our study, we observe Sn at shorter ranges for some parts of the Colorado Plateau, and the strength of the amplitudes in the stacks change from the northeastern section to the southwestern part. Our stacks that sample the southwestern part of the Plateau do not show evidence for Sn, roughly for the same area as USArray uppermost mantle tomographies show low shear velocities. However, stacks from ray paths that mostly sample the northeastern part of the Colorado Plateau, generally associated with faster upper mantle velocities, show a low-energy Sn strand arriving slightly later than the time estimated from the Pn Moho depth model (Figure 4.4, stack 5). This suggests that Sn is strongly attenuated when it travels across the likely warmer western and southern margins of the Colorado Plateau, where [*Schmandt and Humphreys*, 2010] show very low shear velocities at 90 km depth, and that a thin lithosphere is not necessarily the primary reason for Sn attenuation. This is in agreement with recent mapping of the asthenosphere-lithosphere boundary (LAB) below the western United States with receiver functions [*Kumar et al.*, 2012; *Levander and Miller*, 2012],

that generally show a thicker lithosphere below the Colorado Plateau compared to the adjacent Basin and Range province. *Kumar et al.* [2012] find boundary depths up to 140 km below the Colorado Plateau. The estimates by *Levander and Miller* [2012] are lower at ∼90 km, but still significantly deeper compared to their measured LAB depth of ∼65 km below the Basin and Range. In addition, *Obrebski et al.* [2011] noted that their observation of high shear velocities might be consistent with a stable and relatively thick lithosphere for the northeastern part of the Colorado Plateau.

Compared to the heterogeneous picture of Sn attenuation, the amplitude of the crustal shear wave changes more gradually over the western United States (Figure 4.5). It is recognized that Lg does not traverse across oceanic crust [e.g., *Kennett and Furumura*, 2001], and we do not observe Sg or Lg in stacks at the western coast with contributions from mostly offshore earthquakes. *Phillips and Stead* [2008] also show strong Lg attenuation along the western margin. *Isacks and Stephens* [1975] describe the conversion of Sn to Lg at continental margins, and we observe that the Lg amplitude gradually increases away from the coast to a maximum in the central Great Basin around 115°W. But more detailed work would be needed to assess conversions of the phases. In addition, we don't find anomalous Lg amplitudes for the Colorado Plateau that would suggest any significant energy transfer from the uppermost mantle into the crust. Similar to *Phillips and Stead* [2008] we observe that Lg, in contrast to Sn, generally propagates well in the Snake River Plain.

4.4 Summary

We examine the propagation of Sn in the western United States. The dense USArray station coverage allows us to experiment with methods that are conventionally used in active-source studies at local scales. Common mid-point stacking analysis shows that Sn is highly attenuated across smaller and more localized regions than previously assumed, mostly where the paths cross the perimeter of the Great Basin. We find that the regions with high Sn attenuation correlate with volcanism and previously imaged low velocity anomalies in the uppermost mantle. These observations are in agreement with local zones of partially molten uppermost mantle material. We find Sn arrivals along the coast of California, Oregon and Washington, in the central Great Basin, in the northeastern part of the Colorado Plateau, and the Columbia Plateau. The structure of the Sn propagation efficiency below the Colorado Plateau is non-uniform, and the signal

strength increases from southwest to northeast. This is in agreement with a potentially intact and thicker lithosphere in the northeastern part of the Colorado Plateau, as previously suggested as an explanation for the higher body-wave velocities in this region, but more localized measurements are needed for more conclusive interpretations.

Acknowledgments

We thank Luciana Astiz for discussions and assistance with the Antelope system, and two anonymous reviewers for their constructive comments. This research was supported by grant EAR-0950391 from the National Science Foundation. Chapter 4, in full, is in revision for publication in Geophysical Research Letters: Buehler, J. S. and P. M. Shearer, Sn propagation in the western United States from common mid-point stacks of USArray data, Geophysical Research Letters, in review, 2013. The dissertation author was the primary investigator and author of this paper.

References

Astiz, L., P. Earle, and P. Shearer (1996), Global Stacking of Broadband Seismograms, *Seismological Research Letters*, *67*(4), 8–18, doi:10.1785/gssrl.67.4.8.

Barron, J., and K. Priestley (2009), Observations of frequency-dependent Sn propagation in Northern Tibet, *Geophysical Journal International*, *179*(1), 475–488.

Beghoul, N., M. Barazangi, and B. L. Isacks (1993), Lithospheric structure of Tibet and western North America: Mechanisms of uplift and a comparative study, *J. Geophys. Res.*, *98*(B2), 1997–2016.

Behm, M., E. BrÃijckl, W. Chwatal, and H. Thybo (2007), Application of stacking and inversion techniques to three-dimensional wide-angle reflection and refraction seismic data of the Eastern Alps, *Geophysical Journal International*, *170*(1), 275–298, doi: 10.1111/j.1365-246X.2007.03393.x.

Braile, L. W., and R. B. Smith (1975), Guide to the interpretation of crustal refraction profiles, *Geophysical Journal International*, *40*(2), 145–176.

Buehler, J. S., and P. M. Shearer (2010), Pn tomography of the western United States using USArray, *J. Geophys. Res.*, *115*(B9), B09,315–.

Calvert, A., E. Sandvol, D. Seber, M. Barazangi, F. Vidal, G. Alguacil, and N. Jabour (2000), Propagation of regional seismic phases (Lg and Sn) and Pn velocity structure along the Africa-Iberia plate boundary zone: tectonic implications, *Geophysical Journal International*, *142*(2), 384–408.

Diaz, J., A. Gil, and J. Gallart (2013), Uppermost mantle seismic velocity and anisotropy in the Euro-Mediterranean region from Pn and Sn tomography, *Geophysical Journal International*, *192*(1), 310–325, doi:10.1093/gji/ggs016.

Goek, R., E. Sandvol, N. TÃijrkelli, D. Seber, and M. Barazangi (2003), Sn attenuation in the Anatolian and Iranian plateau and surrounding regions, *Geophys. Res. Lett.*, *30*(24), 8042–.

Goes, S., and S. van der Lee (2002), Thermal structure of the North American uppermost mantle inferred from seismic tomography, *Journal Of Geophysical Research-Solid Earth*, *107*(B3).

Hill, D. P. (1973), Critically refracted waves in a spherically symmetric radially heterogeneous earth model, *Geophysical Journal International*, *34*(2), 149–177.

Isacks, B. L., and C. Stephens (1975), Conversion of Sn to Lg at a continental margin, *Bulletin of the Seismological Society of America*, *65*(1), 235–244.

Kennett, B. L. N., and T. Furumura (2001), Regional phases in continental and oceanic environments, *Geophysical Journal International*, *146*(2), 562–568, doi:10.1046/j.1365-246x.2001.01467.x.

Kumar, P., X. Yuan, R. Kind, and J. Mechie (2012), The lithosphere-asthenosphere boundary observed with USArray receiver functions, *Solid Earth*, *3*, 149–159.

Lachenbruch, A. (1978), Heat flow in the Basin and Range province and thermal effects of tectonic extension, *Pure and Applied Geophysics*, *117*(1-2), 34–50–.

Levander, A., and M. S. Miller (2012), Evolutionary aspects of lithosphere discontinuity structure in the western u.s., *Geochem. Geophys. Geosyst.*, *13*(7), Q0AK07–.

Levander, A., B. Schmandt, M. S. Miller, K. Liu, K. E. Karlstrom, R. S. Crow, C.-T. A. Lee, and E. D. Humphreys (2011), Continuing Colorado plateau uplift by delamination-style convective lithospheric downwelling, *Nature*, *472*(7344), 461–465.

Lin, F.-C., M. H. Ritzwoller, Y. Yang, M. P. Moschetti, and M. J. Fouch (2011), Complex and variable crustal and uppermost mantle seismic anisotropy in the western United States, *Nature Geosci*, *4*(1), 55–61.

Menke, W. H., and P. G. Richards (1980), Crust–mantle whispering gallery phases: A deterministic model of teleseismic pn wave propagation, *Journal of Geophysical Research: Solid Earth*, *85*(B10), 5416–5422.

Molnar, P., and J. Oliver (1969), Lateral variations of attenuation in the upper mantle and discontinuities in the lithosphere, *J. Geophys. Res.*, *74*(10), 2648–2682.

Ni, J., and M. Barazangi (1983), High-frequency seismic wave propagation beneath the Indian Shield, Himalayan Arc, Tibetan Plateau and surrounding regions: high uppermost mantle velocities and efficient Sn propagation beneath Tibet, *Geophysical Journal of the Royal Astronomical Society*, *72*(3), 665–689.

Obrebski, M., R. M. Allen, F. Pollitz, and S.-H. Hung (2011), Lithosphere-asthenosphere interaction beneath the western United States from the joint inversion of body-wave traveltimes and surface-wave phase velocities, *Geophysical Journal International*, *185*(2), 1003–1021.

Pei, S., J. Zhao, Y. Sun, Z. Xu, S. Wang, H. Liu, C. A. Rowe, M. N. ToksÃűz, and X. Gao (2007), Upper mantle seismic velocities and anisotropy in China determined through Pn and Sn tomography, *J. Geophys. Res.*, *112*(B5), B05,312–.

Phillips, W. S., and R. J. Stead (2008), Attenuation of Lg in the western US using the USArray, *Geophys. Res. Lett.*, *35*(7), L07,307–.

Richards-Dinger, K. B., and P. M. Shearer (1997), Estimating crustal thickness in southern California by stacking PmP arrivals, *J. Geophys. Res.*, *102*(B7), 15,211–15,224.

Rodgers, A. J., J. F. Ni, and T. M. Hearn (1997), Propagation characteristics of short-period Sn and Lg in the Middle East, *Bulletin of the Seismological Society of America*, *87*(2), 396–413.

Schmandt, B., and E. Humphreys (2010), Complex subduction and small-scale convection revealed by body-wave tomography of the western United States upper mantle, *Earth and Planetary Science Letters*, *297*, 435–445.

Sereno, T. J. (1989), Numerical modeling of Pn geometric spreading and empirically determined attenuation of Pn and Lg phases recorded in eastern Kazakhstan, *Tech. rep.*, Science Applications International Corporation.

Stephens, C., and B. L. Isacks (1977), Toward an understanding of Sn: Normal modes of love waves in an oceanic structure, *Bulletin of the Seismological Society of America*, *67*(1), 69–78.

West, J. D., M. J. Fouch, J. B. Roth, and L. T. Elkins-Tanton (2009), Vertical mantle flow associated with a lithospheric drip beneath the Great Basin, *Nature Geoscience*, *2*(6), 439–444.

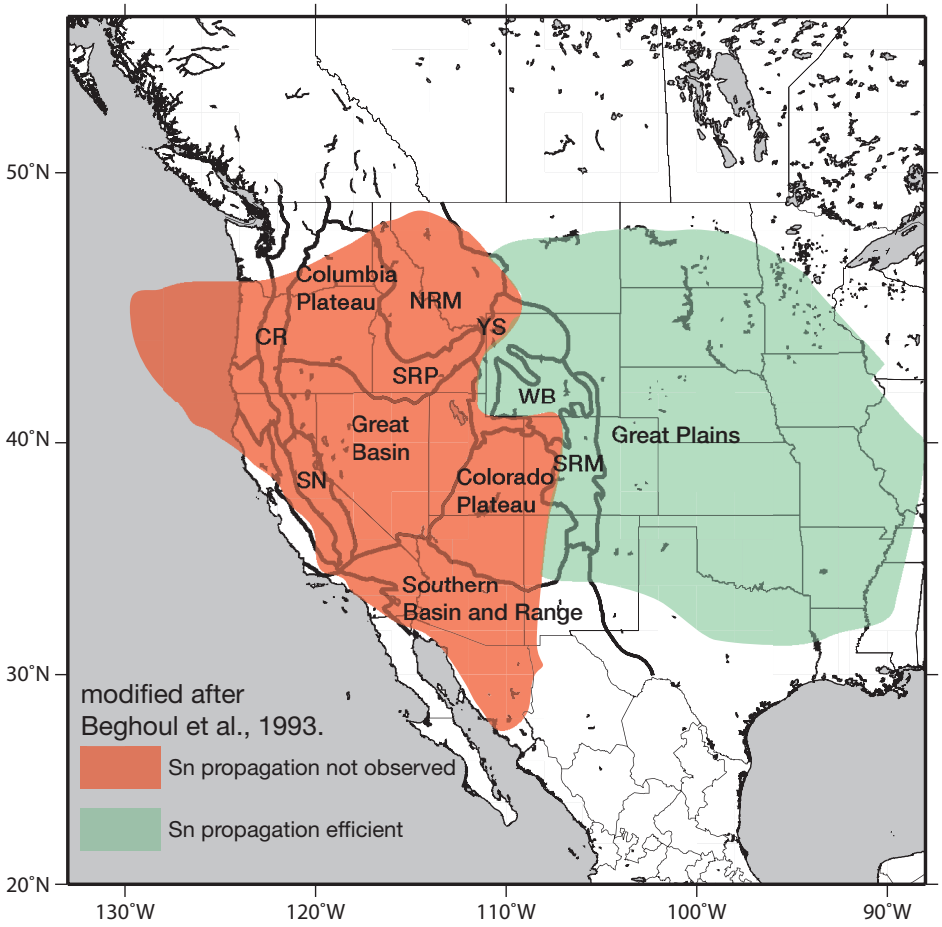

Figure 4.1: Map modified after *Beghoul et al.* [1993] showing that Sn is strongly attenuated for much of the western United States, but that clear Sn arrivals can be observed at stations in the Great Plains. The physiographic provinces are indicated by black lines and names. The abbreviations are in place for the Cascade Range (CR), Sierra Nevada (SN), Snake River Plain (SRP), Northern Rocky Mountains (NRM), Yellow Stone (YS), Wyoming Basin (WB), and Southern Rocky Mountains (SRM).

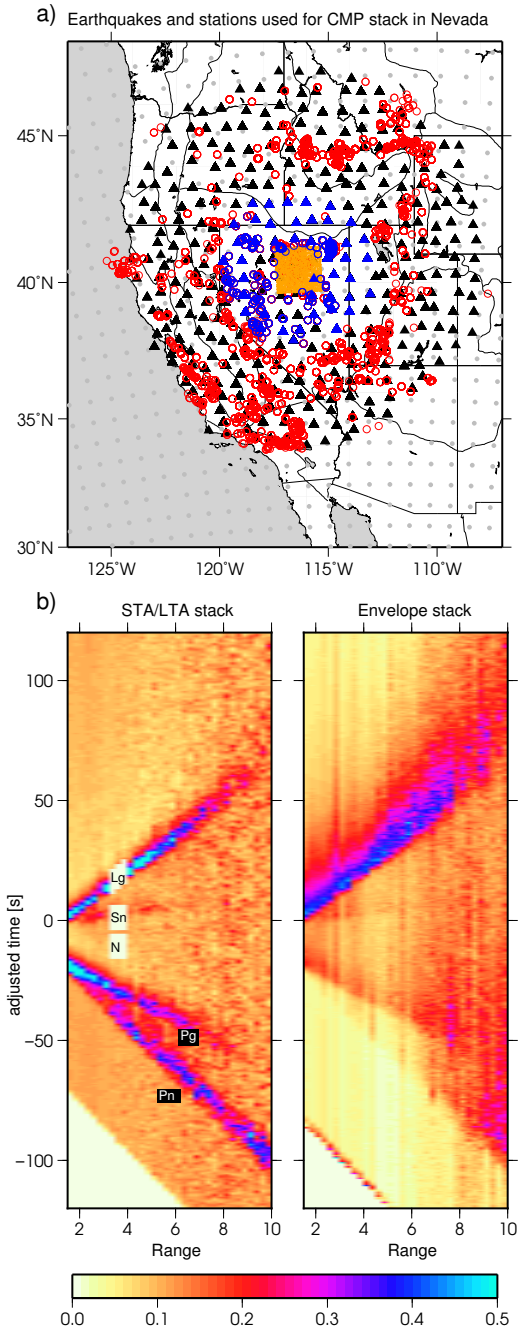

Figure 4.2: Common mid-point radial-component stack examples for a location in central Nevada. a) The stations (triangles), and events (circles) used to image wave propagation within the orange square. The blue triangles and circles indicate stations and events that contribute to the stack between a range of 3.25–4.0 degrees where we measure the amplitudes. b) STA/LTA and envelope stacks showing the characteristics of the regional phases for this region. The windows that we use to measure the Sn, Lg and noise amplitudes are indicated by the light yellow polygons. Individual traces of the stacks are normalized by their maximum amplitudes, and each range bin stack is normalized by the number of traces in that bin. The color scale is capped at 0.5 for visual enhancement of weaker phases.

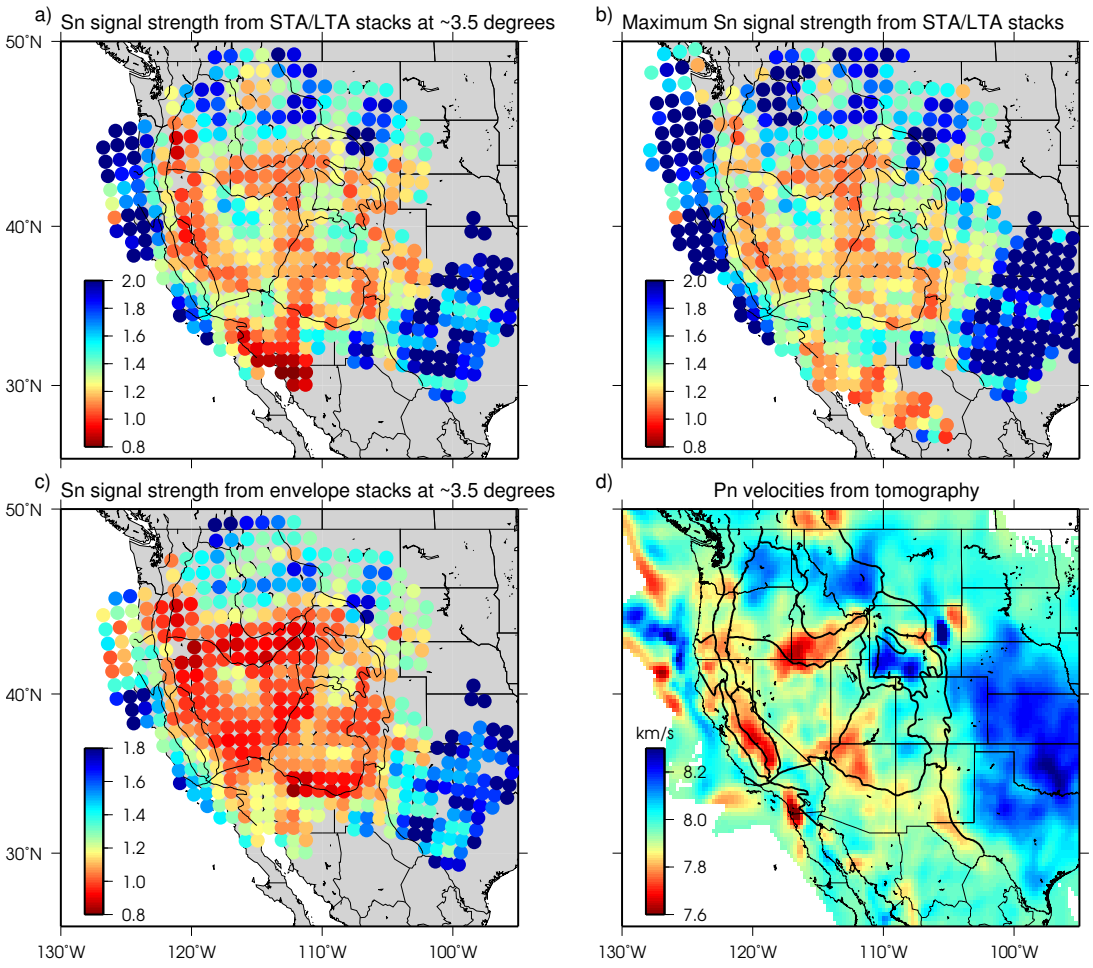

Figure 4.3: a) Measured Sn amplitudes at a range of 3.25 to 4 degrees in STA/LTA stacks normalized by the rms amplitude of the P-coda. Blue colors indicate regions of strong Sn signal, red colors show regions that greatly attenuate Sn. Regions without colored circles don't have enough data after processing. b) same as a), but the maximum amplitudes of all range windows are plotted. c) Measured Sn amplitudes at a range of 3.25 to 4 degrees in envelope stacks normalized by the rms amplitude of the P-coda. d) Pn velocities from tomography for comparison. Measured rms Sn amplitudes are typically lower in regions of low Pn velocities.

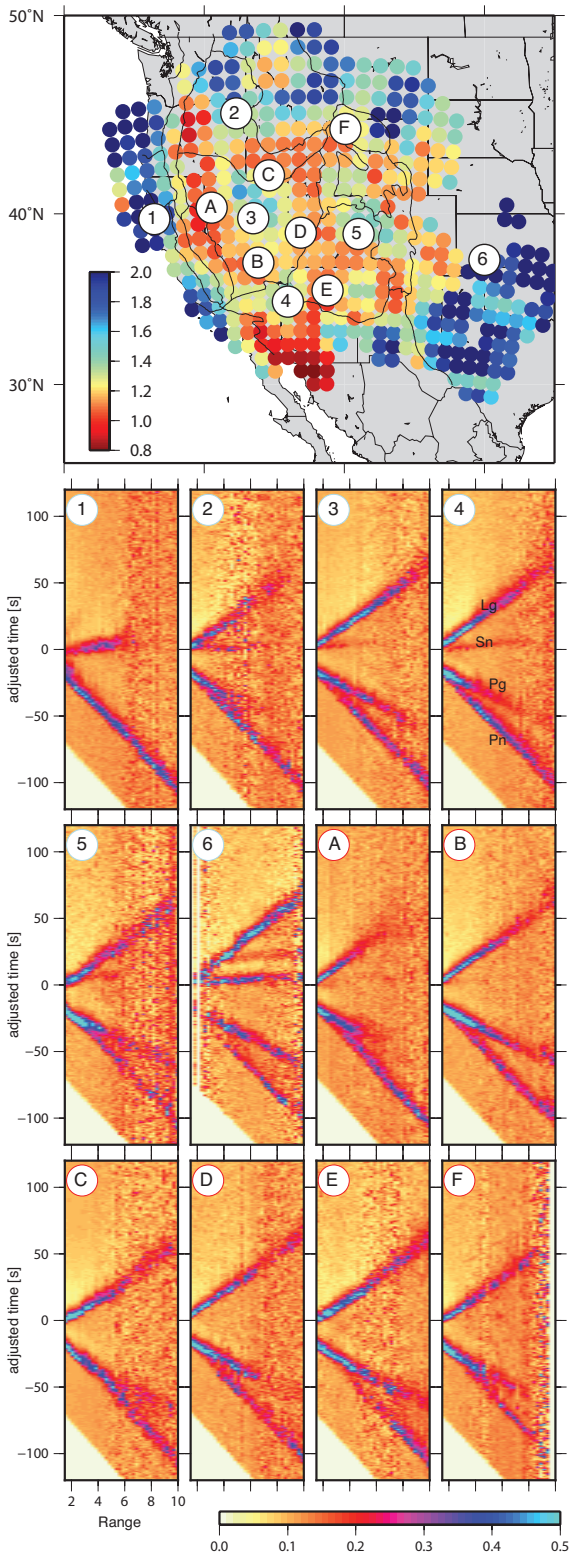

Figure 4.4: Images of individual STA/LTA common mid-point transverse-component stacks at various locations. Number or letter in the upper left corner of each stack corresponds to the number/letter in the map on the top. Stacks 1-6 show Sn, but Sn is attenuated in stacks A-F.

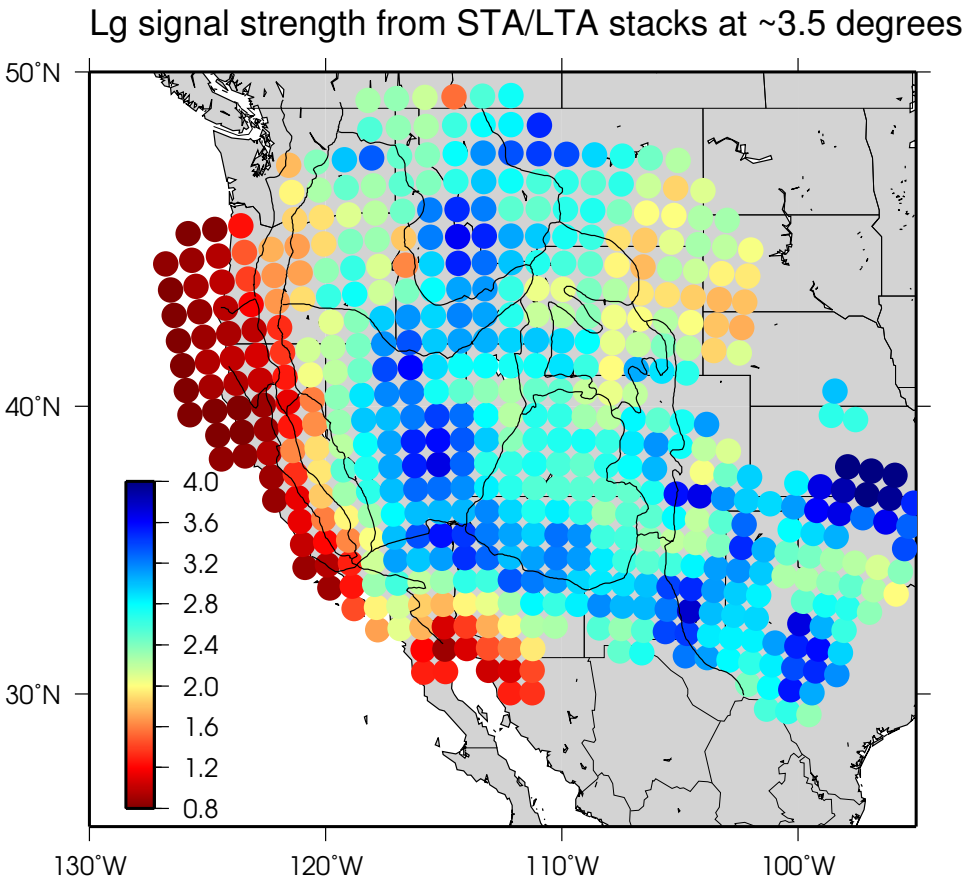

Figure 4.5: Measured Lg amplitudes in STA/LTA stacks normalized by the rms amplitude of the P-coda.

Supplementary Figures

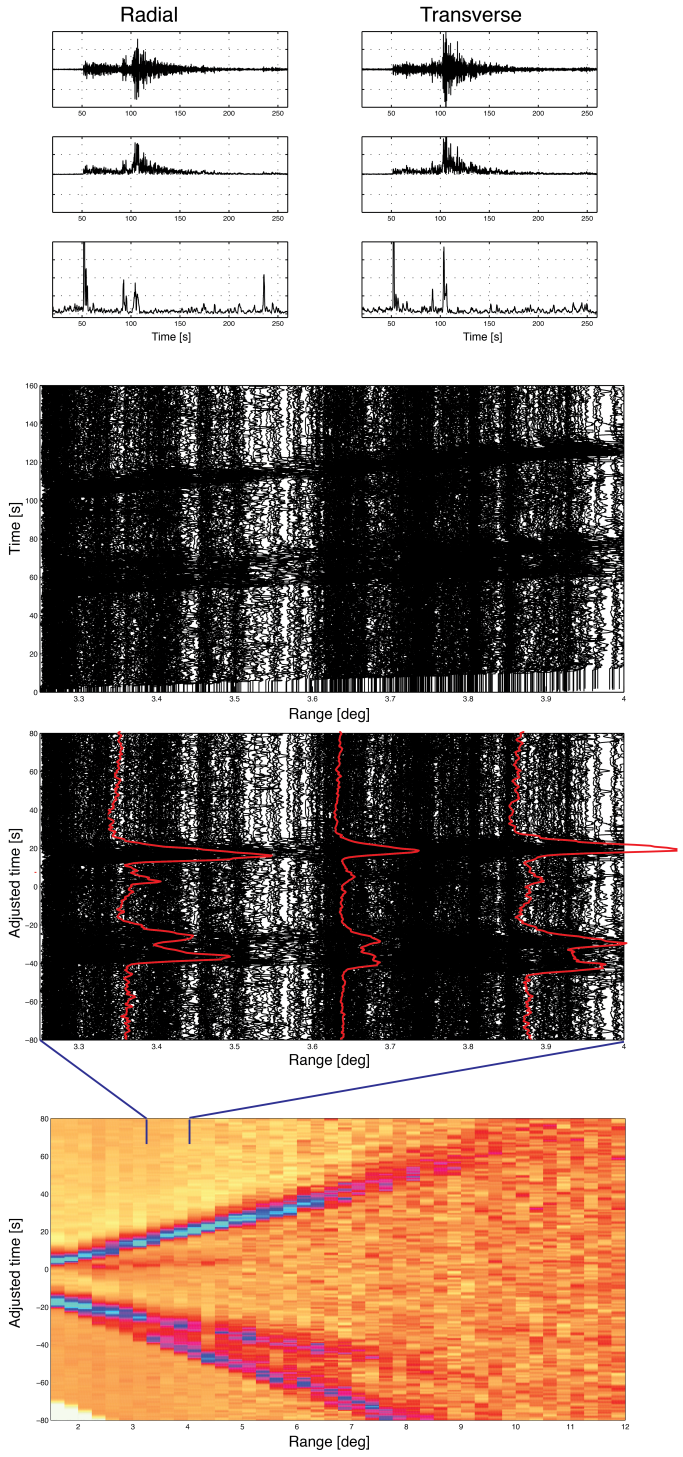

(1)
We collect all seismograms of a common mid-point cell and compute envelope and STA/LTA functions for each trace.

(2)
All STA/LTA (and envelope) functions of the cell are gathered. Here we just show all the transverse STA/LTA traces with epicentral distances between 3.25 and 4 degrees, but we process traces up to 12 degree range.

(3)
Next we estimate an average uppermost mantle velocity and intercept time for the cell location and adjust the timing of the seismograms accordingly. Sn should line up at time ~0.

Then we compute the mean value of each trace in every 0.5 s time bin and stack all the traces in every 0.25 degree distance bin. The stacked traces are shown in red.

(4)
Finally we display the whole stack as an image in order to highlight the phase arrivals.

We measure the RMS amplitude of Lg, Sn, and P-coda at various distances.

Figure 4.6: Supplementary Figure 1. Processing steps for the generation of STA/LTA stacks.

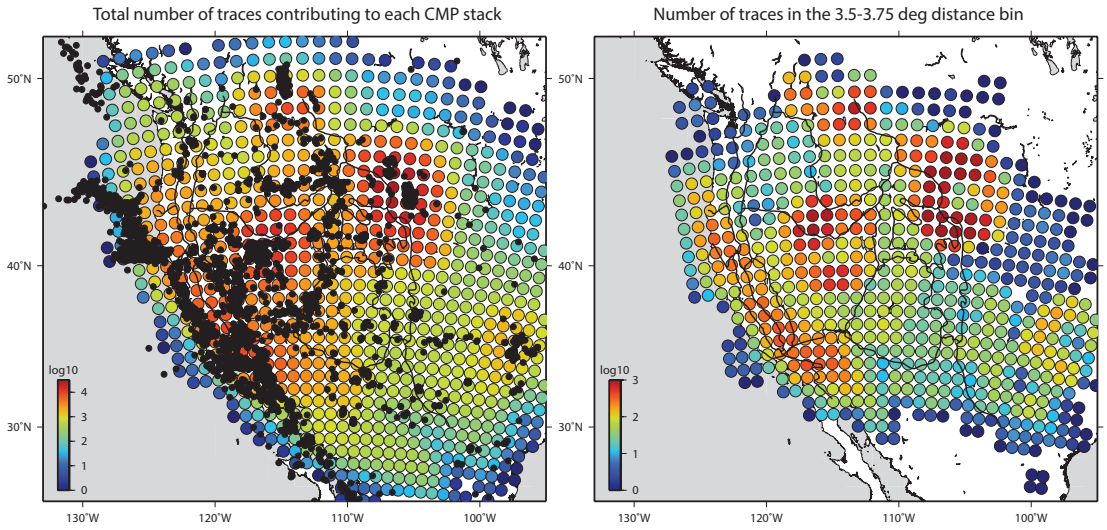

Figure 4.7: Supplementary Figure 2. (Left) Total number of seismograms contributing to each common mid-point stack. Events used are indicated by black dots. (Right) Number of seismograms in the 3.5°-3.75° bin at each cell location.

Chapter 5

Anisotropy and Vp/Vs in the uppermost mantle beneath the western United States from joint analysis of Pn and Sn phases

Pn and Sn phases are valuable for resolving velocity structure in the mantle lid, as they propagate horizontally right below the Moho. Relatively few Sn tomography attempts have been made compared to Pn, because Sn is often highly attenuated or buried in P-wave coda. USArray has greatly increased data coverage for regional phases, and both Pn and Sn are routinely picked by network analysts. Here we jointly invert Pn and Sn arrival-time residuals with a modified time-term analysis and a regularized tomography method and present new maps of crustal thickness, uppermost mantle P-velocity perturbations, Vp/Vs ratios, and azimuthal anisotropy strength and orientation beneath the western United States. The results indicate partially molten mantle below the Snake River Plain and the Colorado Plateau. The seismic structure of the top ∼40 km of the mantle below the Colorado Plateau differs from that seen at greater depths in other studies, such as surface-wave or teleseismic body-wave tomography, whereas the Snake River Plain anomaly just below the Moho is comparable to structures seen at about ∼200 km depth. Pn fast axes provide complementary information to SKS shear-wave splitting observations, and our analysis indicates that in several regions in the western United States the orientation of azimuthal anisotropy changes with depth in the upper

mantle. However, we have so far been unable to resolve shear-wave splitting directly in Sn waveforms, which seem to be dominated by Sn-SV energy.

5.1 Introduction

The North American lithosphere and upper mantle has attracted much recent attention, as the increased data coverage from USArray has allowed imaging its seismic structure on a regional scale. Seismic velocities in the upper mantle are generally lower in the tectonically active western United States and higher below the Great Plains province (Figure 5.1a), but many smaller-scale anomalies appear in recent tomographic maps, such as lithospheric drip features or downwellings imaged with body-wave tomography [e.g. *Obrebski et al.*, 2011; *Roth et al.*, 2008; *Schmandt and Humphreys*, 2010; *West et al.*, 2009]. In addition, complex patterns of azimuthal anisotropy have been imaged in great detail in both the crust and upper mantle in the western United States with new ambient noise tomography methods [e.g. *Lin and Ritzwoller*, 2011; *Lin et al.*, 2011; *Ritzwoller et al.*, 2011] and with shear-wave splitting analysis [e.g. *Liu*, 2009; *West et al.*, 2009]. Crustal thickness estimates have been made with various approaches on local and regional scales, including receiver function analysis [*Gilbert*, 2012; *Lowry and Perez-Gussinye*, 2011; *Levander et al.*, 2011] and Pn tomography [*Buehler and Shearer*, 2010]. Recently *Tape et al.* [2012] compiled a variety of studies to obtain a detailed Moho surface for California.

However, even with improved resolution, interpretation of imaged seismic anomalies remains challenging, as the seismic velocities are influenced by a variety of factors, including temperature, composition, the presence of partial melt or water, and, in some studies, unmodeled anisotropy [e.g. *Goes et al.*, 2000; *Perry et al.*, 2006]. In addition, surface-wave tomography averages over the crust and upper mantle, depending on frequency, and teleseismic body-wave tomography with near-vertical incidence angles typically has low lateral resolution in the lithosphere. Joint surface- and body-wave tomographies have been successful at mitigating the problem [*Obrebski et al.*, 2011]. Recently *Shen et al.* [2013] jointly inverted receiver functions and surface-wave dispersion to increase vertical resolution. Seismic velocity and anisotropy imaged with Pn and Sn waves, which are confined to the mantle lid, can provide effective additional depth constraints.

Pn and Sn are regional seismic phases that propagate horizontally in the uppermost

mantle just below the Moho and are the first-arriving P and S phases at regional distances. They are typically described as critically refracted or head-waves along the Moho, although effects from uppermost mantle velocity gradients, lateral velocity heterogeneities and Moho topography contribute to more complicated propagation characteristics [e.g. *Bakir and Nowack*, 2012]. However, *Langston* [1982] found that Pn can be well-modeled as a head-wave in the western United States. Since Pn and Sn tomographic studies are dependent on event-station distances between ∼2 and ∼14 degrees, depending on crustal thickness and mantle lid structure, USArray has greatly increased usable data outside the westernmost regions of North America, and permits imaging Pn and Sn velocity structure with good resolution on a regional scale.

Regional phases are challenging to analyze, especially in a tectonically active region like the western United States, since they are strongly affected by heterogeneities in the uppermost mantle and Sn is often highly attenuated [e.g. *Beghoul et al.*, 1993]. *Chulick and Mooney* [2002] compiled Pn and Sn studies for North America to produce contour maps of the seismic velocity in the uppermost mantle. They found only 114 Sn data points for the continent and could only produce a very rough Sn velocity map with generally lower velocities in the west, and higher velocity beneath the Great Plains. Therefore, the increased Sn observations with USArray are valuable to gain further insight into the seismic properties of the mantle lid. Often anomalous velocity structures of regional phases are interpreted with respect to the thermal structure of the lithosphere, as temperature seems to be the dominant factor influencing seismic velocities [*Goes et al.*, 2000]. Jointly analyzing Pn and Sn data, and imaging the P-to-S velocity ratio (Vp/Vs), can help identify regions where properties other than temperature influence seismic velocities, because the P and S waves generally have different sensitivities to the parameters that influence seismic velocities.

Anisotropy that is not accounted for in inversions can map into spurious velocity anomalies, for example, in regions with a dominant ray direction. It is therefore critical to include anisotropy in upper-mantle tomography. In addition, seismic anisotropy can be related to the mantle strain history [e.g. *Long and Becker*, 2010; *Park and Levin*, 2002; *Savage and Silver*, 1993], and it seems especially important to put Pn and Sn anisotropy models into the context of measurements from surface-wave tomography and shear-wave splitting, which have lower vertical resolution but little trade-off with lateral heterogeneities, in order to compare the anisotropic observations to predictions from

geodynamic models. We previously found that Pn anisotropy differs from recent shear-wave splitting results [*Buehler and Shearer*, 2010], suggesting that the distinct rotational fast axis around the Great Basin seen in splitting studies originates from sub-lithospheric mantle flow. To analyze the nature of uppermost mantle material more completely, it is useful to include shear wave arrivals. With Pn anisotropy alone we can only resolve three of the five parameters of the elastic tensor that describes a weakly hexagonal anisotropic material with a known horizontal symmetry axis, but with measurements of azimuthal velocity variations of Pn, Sn-SH, and Sn-SV velocities, it is possible, in theory, to estimate all five elastic parameters.

Only a few studies of uppermost mantle structure include the shear arrivals, even though Pn tomography exists for many regions, and usually they are addressed separately. Here we attempt joint Pn-Sn tomography for the western United States. We find some evidence for shear-wave splitting in the Sn waves, and waveform stacks generally show that Sn-SH arrives before Sn-SV at large distances, but we are not able to successfully automate the analysis or to more locally resolve shear-wave anisotropy. Still, we find useful signal in the Sn picks, and extend our previous studies that used Pn data alone [*Buehler and Shearer*, 2010, 2012] to image Vp/Vs anomalies and improve our understanding of the imaged Pn velocity anomalies. In addition, we gain further constraints on crustal thickness and velocity structure from the set of Sn time terms that account for the time the rays spend in the crust.

5.2 Data and Methods

5.2.1 Regional Travel Time Picks

We use the regional uppermost mantle Pn and Sn phases recorded at USArray stations at -135° to -97° longitude from April 2004 to June 2012 (Figure 5.1b). Sn is often inefficient in propagation or buried in P-wave coda, which makes picking difficult, and our attempt to use auto-picker picks to fill in data gaps was mostly unsuccessful. We found, however, a number of Sn array network facility (ANF) analyst picks in the USArray data set. Analysts at the ANF routinely pick first arrivals and sometimes also later phases. Figure 5.2 provides an overview of the available regional picks according to the assigned labels for the stations and recording times we use here. There is some reason to doubt the Sn picks, as the phase is highly attenuated on paths in the western

United States [*Beghoul et al.*, 1993]. However we visually inspected many seismograms and performed stacking analysis to identify regions that transmit Sn and found that the highly attenuating regions are similar in size to the low-velocity anomalies . In addition, separate Sn tomography with the ANF analyst picks shows similar large-scale features as imaged with Pn data (see below). This suggests that there is no reason to distrust that these picks measure useful Sn signal.

All the arrival-time picks that we are using here are available for download in monthly intervals at http://anf.ucsd.edu/tools/events/ (last accessed July 2013). We select earthquakes and quarry blasts from longitude -135°E to -90°E, and latitude 20° to 60°, and allow a maximum event depth of 30 km. We found that the ANF pick label is not always reliable and therefore restrict epicentral distances to be within 200 and 1400 km in order to avoid both crustal phases and rays sampling sub-mantle-lid regions, respectively. Looking at a reduced time-distance plot (Figure 5.3), the Pn picks form a straight line up to ∼1400 km but start to bend at longer ranges, indicating that these waves probably dive beneath the mantle lid. The Sn arrivals form a fairly straight line, but there are many fewer picks at larger ranges. Next, we proceed in iterative fashion to window the arrivals in space and time, and require all stations to have at least 5 records and all events to be recorded with picks by at least 5 stations (3 for Sn). In addition we discard picks with residuals larger than 3 seconds (4 for Sn) after a 1-D time-term fit. The final data set is indicated in red in Figure 5.3, and consists of ∼183,000 and ∼45,000 Pn and Sn picks, respectively, from 13,200 events recorded at 977 station locations.

5.2.2 Analysis of Sn Picks and Waveforms

Working with Sn is not only more challenging compared to Pn because of higher attenuation and typically lower signal-to noise ratios, but also because shear-wave behavior in anisotropic media is generally more complicated than that of compressional waves. However it is worth the effort, in theory, to incorporate both the P- and S-waves together in order to obtain a more complete picture of the anisotropy in the uppermost mantle and to compare observations to model predictions for an improved understanding of the mantle strain history.

Seismic anisotropy manifests itself in seismic velocities that vary with azimuth and in split shear-wave arrivals, and comparison of these anisotropic characteristics with elastic properties of upper-mantle material provides information on the fabric and deformation

of material at depth. Generally the 21 free parameters of the elastic tensor of a general anisotropic material cannot be resolved within the resolution of seismic observations. However, anisotropy of crust and mantle material is often well approximated to have hexagonal symmetry (rotational symmetry around a single axis). This simplifies the characterization of the material because the introduced symmetries reduce the number of free parameters of the elastic tensor from 21 to 5 when the orientation of the symmetry axis is known.

Moschetti et al. [2010a] estimated relatively strong positive ($V_{SH} > V_{SV}$) azimuthally-averaged radial anisotropy in the Basin and Range region in the uppermost mantle. We make similar path-averaged observations at large ranges in waveform stacks for the whole western United States region where we observe Sn-SH to arrive before Sn-SV. As previously discussed, Pn and surface-wave tomographies also show considerable azimuthal anisotropy. In order to achieve azimuthal velocity variations for horizontally propagating Pn and Sn waves, the axis of symmetry must be non-vertical and is usually assumed to be horizontal. In the upper mantle, anisotropy is thought to be mostly caused by lattice-preferred alignment of olivine crystals where the olivine a-axis aligns with the direction of mantle flow. This introduces a form of anisotropy that is well-modeled with hexagonal symmetry with a horizontal axis if the b- and c-axis are randomly aligned [e.g. *Christensen*, 1984; *Maupin and Park*, 2007].

To obtain wave speeds and polarizations of each quasi P- and the two quasi S-waves it is generally necessary to solve for the eigenvalues and vectors of the Christoffel equation, which gives the particle motion and velocities of plane waves in a medium with a given elasticity tensor for each propagation direction [e.g. *Babuska and Cara*, 1991]. It is simpler to study the azimuthal dependence on seismic velocities with approximations to the exact solution of the Christoffel equation, and for weakly anisotropic material, the anisotropy can be expressed as perturbations to the isotropic wave speeds [*Backus*, 1965; *Crampin*, 1981]. In a hexagonally symmetric material with a horizontal symmetry axis, the two quasi Sn waves are polarized SH and SV, and the azimuthal velocities variations can be expressed according to *Backus* [1965] as:

$$V_P^2 = A + B\cos 2\theta + C\cos 4\theta$$
$$V_{SV}^2 = D + E\cos 2\theta$$
$$V_{SH}^2 = C + D + E - C\cos 4\theta$$

where θ is the angle from the symmetry axis. A, B, C, D, and E, are related to the

coefficients of the elastic tensor, and knowledge of these five parameters is enough to describe a hexagonally symmetric anisotropy. According to these equations, we could recover all five parameters needed if we can separately measure the velocities of Sn-SH and Sn-SV, and if the azimuthal coverage is acceptable. We could then compare these observations with elastic tensors used to model uppermost mantle material in order to understand the tectonic forces that cause the alignment of the olivine crystals [e.g. *Shearer and Orcutt*, 1986]. This idealized model predicts that Sn should exhibit shear-wave splitting, with vertically-polarized Sn exhibiting a 2θ azimuthal dependence and horizontally-polarized Sn exhibiting a 4θ azimuthal dependence.

However, for reasons that we don't completely understand, this is not what we observe. Our Sn polarization analyses may be summarized as follows: First we tried to obtain separate SH and SV picks. Because the Sn picks from the ANF do not indicate their polarity, we attempted to pick, cross-correlate, and separately realign the radial and transverse components of the Sn waveforms. However, we achieved little success, as Sn is generally only weakly visible across the array and clean arrivals can only be observed for a few regions in the western United States. Polarization filtering based on particle motion linearity [e.g. *Jurkevics*, 1988] did not help, as it only improves the picking accuracy of the faster-traveling shear wave before the particle motion becomes elliptical.

Next we tried to focus on just a few localized regions with relatively uniform Pn-anisotropy to avoid path averaging of azimuthal variations. Figure 5.4a shows the measured azimuthal velocity variations for Pn and Sn on both the radial and transverse components for a station sub-array in California. The velocity and azimuth measurements are obtained as described in *Buehler and Shearer* [2012], by fitting inter-station differential times for the apparent velocity and direction of the incoming wavefront. However, velocity variations for both Sn-SH and Sn-SV show a similar 2θ pattern to that seen for Pn, and we find no evidence for 4θ oscillations or diminished anisotropy in the velocity of the transversely polarized wave. It is possible that SV energy is leaking onto the transverse component, or that the largest amplitude signal is not caused by material anisotropy, but by complexities of the Moho topography. A ridge-like Moho topography under the Sierra Nevada could possibly cause 2θ variations in apparent velocity and needs further investigation.

Figure 5.4b shows another station subarray example for northwestern Nevada, where Pn tomography and a surface-wave model [e.g. *Lin et al.*, 2011] indicate consistent

east-west to northeast-southwest fast axes, but Sn velocity measurements appear scattered without a clear azimuthal signal. In this case, the scatter probably arises from incoherent low-amplitude waveform cross-correlations that are prone to cycle skipping. In some cases, however, inspection of individual waveforms showed evidence for splitting in this region, which motivated us to try another approach. We attempted to predict the delay time between the two shear waves at individual stations given our Pn anisotropy results, and then to compare these predictions with the measured amount of delay from picks on both the transverse and radial component. However, this also did not yield coherent results. The low-amplitude arrivals are hard to pick consistently with autopickers and the character of the waveforms is quite variable across the western United States. The approaches mentioned here might work better in regions with clearer Sn arrivals, as for example in the Great Plains.

Although we currently cannot clearly resolve Sn anisotropy in the western United States, there appears to be useful signal in the Sn picks, as stand-alone Sn tomography (discussed below) following the approach by *Hearn* [1996] shows consistent large scale features similar to USArray Pn analysis for the same region [*Buehler and Shearer*, 2010]. Since we found 2θ variations, but no 4θ azimuthal changes, it is reasonable to assume that the analyst picks measure mostly Sn-SV arrival times.

5.2.3 Pn-Sn Joint Analysis

USArray Pn tomography alone reveals prominent uppermost mantle velocity features that correlate well with known active processes, as for example the large slow velocity anomaly in the Snake River Plain leading to the Yellowstone hotspot. Our goal here is to add the Sn arrival-time picks to constrain Vp/Vs structure, which should improve our understanding of imaged anomalies by identifying regions where properties other than temperature influence seismic velocities. Our strategy is as follows:

We first apply traditional modified time-term analysis [e.g. *Hearn*, 1996] to the Sn data alone to inspect the agreement between the Sn and Pn results and further assess the quality of the picks. We then continue with a joint Pn-Sn analysis, starting with a 1-D time-term analysis to determine the best-fitting average uppermost mantle Pn and Sn velocities and to obtain an estimate for lateral Moho depth and crustal Vp/Vs variations in the region. Next we perform point inversions to solve for the lateral Pn and Sn velocity perturbations, and finally add anisotropic model parameters to obtain

our preferred uppermost mantle models. We assess the model resolution and trade-off between the various model parameters with a series of synthetic checkerboard tests.

Initial Time-Term Model

Time-term modeling has been done for many years in refraction studies to obtain average regional uppermost mantle velocity and crustal thickness estimates [e.g. *Bath*, 1978]. Traditionally the head-wave along the Moho is described with three terms, accounting for the two crustal legs of the ray path near the station and event, and for the remaining path in the mantle. Here we apply the time-term method to obtain average Pn and Sn velocity, and an estimate for crustal thickness variations in the region. We then use the obtained residuals in the subsequent 2-D tomography to solve for lateral velocity perturbations and anisotropy. The Pn and Sn arrival times at station s from event e, t_{es}^{Pn} and t_{es}^{Sn} respectively, are expressed as:

$$t_{es}^{Pn} = \delta_{es} S_0^P + \tau_s^p + \tau_e^p$$
$$t_{es}^{Sn} = \delta_{es} S_0^S + \tau_s^s + \tau_e^s,$$

where δ_{es} is the epicentral distance, S_0 the average slowness below the Moho, and τ_s and τ_e the station and event time terms respectively. The time terms, which account for the time the ray spends in the crust, are a function of crustal thickness, and crustal and uppermost mantle velocities:

$$\tau_s = H \frac{\sqrt{1 - S_0^2 V_c^2}}{V_c}$$
$$\tau_e = (H - h) \frac{\sqrt{1 - S_0^2 V_c^2}}{V_c}$$

where H is the crustal thickness, h the hypocenter depth, and V_c the crustal velocity. We solve for the uppermost mantle velocities, and the station and event time terms in a least squares sense. The 1-D time term models fit the data much better than a simple straight line, especially since we are using both continental and off-shore earthquakes with considerable changes in crustal thickness. The best-fitting average velocities are 7.96 km/s and 4.51 km/s for Pn and Sn, respectively. Since hypocenter depths in catalogs generally are subject to large error, only τ_s parameters are used to analyze crustal structure. Using the resulting first-order estimate of the Moho topography and the

mean upper-mantle velocities, we calculate the locations of the Moho piercing points for approximate ray-tracing for the subsequent 2-D tomography, assuming the ray obeys Snell's law and a constant crustal velocity of 6.3 km/s, and without taking the dip of the Moho into account. Since the Pn time terms are better constrained than the Sn terms, we use the depth estimates from Pn alone to compute the ray path geometries for both Pn and Sn.

Linear regression to the Pn and Sn residuals can provide information on the ray path averaged change of S-wave velocity relative to P-wave velocity [e.g. *Schmandt and Humphreys*, 2010]. For a Poisson solid, a residual ratio of about 2.2 indicates normal thermal effects while a value near 4 suggests partial melting [e.g. *Ritzwoller et al.*, 1988]. We apply a total least squares fit to the Pn and Sn residuals obtained from the time-term analysis (Figure 5.5a) and obtain a slope of 3.02 with a bootstrap standard deviation of 0.07, indicating that factors other than temperature cause the velocity variations. For comparison, *Schmandt and Humphreys* [2010] found a residual ratio of 2.84 for the same region, based on teleseismic body-wave residuals from upper-mantle tomography.

Figure 5.5b displays the Pn and Sn residual density as a function of epicentral distance. The majority of the ray paths are shorter than 800 km. No systematic deviations from the 1-D time term fit are discernible apart from a slight curvature of the Pn residuals around 1200 km.

2D Joint Pn-Sn Tomography

Several approaches and algorithms to jointly invert for P- and S-wave velocities have been suggested [e.g. *Conder and Wiens*, 2006; *Thurber*, 1993; *Tryggvason*, 2002; *Zhang and Thurber*, 2003]. The USArray data set contains fewer Sn picks than Pn, and the Sn picks are generally of lower quality. We therefore prefer an algorithm that couples the Pn- and Sn-velocity inversion. However, our database generally does not have an Sn pick for every corresponding Pn arrival and vice versa, therefore we avoid methods based on P-S differential arrival times in order to keep as much data as possible. We follow *Conder and Wiens* [2006] and simultaneously solve for perturbations to the average Vp and Vp/Vs without the use of differential times, and describe the Pn and Sn residuals between event e and station s with the following equations:

$$\delta t_{es}^{Pn} = \Sigma \Delta_{esk} \delta s_k + \delta \tau_e^{Pn} + \delta \tau_s^{Pn}$$

$$\delta t_{es}^{Sn} = \Sigma \Delta_{esk} (\delta s_k R_0 + \gamma S_0^P \delta r_k) + \delta \tau_e^{Sn} + \delta \tau_s^{Sn},$$

where Δ_{esk} is the distance the ray travels in the cell k, δs_k and δr_k the slowness and Vp/Vs perturbation in cell k, and S_0 and R_0 the average uppermost mantle P-wave slowness and Vp/Vs ratio. *Conder and Wiens* [2006] noted the importance of considering the difference in magnitude between the average slowness S_0 and Vp/Vs ratio R_0, which can cause problems in ill-posed inversions, which is typically the case in seismic tomographies with limited ray coverage. To fix this problem they suggest using a weighting parameter γ for the Vp/Vs derivatives to equalize the emphasis on the model parameters. In addition, we apply Tikhonov regularization to stabilize the resulting system $d = Gm$ by adding both smoothing and damping constraints for the δs_k and δr_k parameters, and solve it in a least squares sense with a conjugate gradient solver. We run inversions for several different regularization parameters to obtain trade-off curves and various models with both synthetic and real data.

Anisotropy can significantly influence the observed seismic velocities, and if not accounted for it could translate to wrongly mapped structures, especially in regions with a dominant ray path direction. We follow *Hearn* [1996] and add anisotropic parameters to the Pn equation according to the derivations by *Backus* [1965], described above, for a modified time term inversion:

$$\delta t_{es}^{Pn} = \Sigma\Delta_{esk}(\delta s_k + B1_k \cos 2\phi_{esk} + B2_k \sin 2\phi_{esk}) + \delta\tau_e^{Pn} + \delta\tau_s^{Pn}$$
$$\delta t_{es}^{Sn} = \Sigma\Delta_{esk}(\delta s_k R_0 + \gamma S_0^P \delta r_k) + \delta\tau_e^{Sn} + \delta\tau_s^{Sn}$$

where ϕ_{esk} is the back-azimuth in cell k. As in Pn-only tomography [*Buehler and Shearer*, 2010], we neglect any possible 4ϕ Pn azimuthal variations because previous studies of mantle anisotropy have generally found the 2ϕ terms to dominate [e.g. *Raitt et al.*, 1969; *Christensen*, 1984]. For completeness we prefer to add anisotropic parameters to the Sn picks as well, assuming they measure SV energy, which seems reasonable since we did not find any evidence for 4ϕ velocity variations:

$$\delta t_{es}^{Pn} = \Sigma\Delta_{esk}(\delta s_k + B1_k \cos 2\phi_{esk} + B2_k \sin 2\phi_{esk}) + \delta\tau_e^{Pn} + \delta\tau_s^{Pn}$$
$$\delta t_{es}^{Sn} = \Sigma\Delta_{esk}(\delta s_k R_0 + \gamma S_0^P \delta r_k + E1_k \cos 2\phi_{esk} + E2_k \sin 2\phi_{esk}) + \delta\tau_e^{Sn} + \delta\tau_s^{Sn}$$

Diaz et al. [2013] reported increased continuity and sharpness for their imaged Sn perturbations with the inclusion of anisotropic parameters, but also caution against strong interpretation of the Sn results. We believe the inclusion of anisotropic parameter to describe Sn makes sense, since we found azimuthal velocity dependence for localized

regions. Assuming hexagonal symmetry with a horizontal symmetry axis, the P- and SV-wave anisotropy is coupled as the wave travels fastest in the same direction. Since uppermost mantle anisotropy is typically well modeled with hexagonal symmetry, we require the Pn and Sn fast axis to point in the same direction in our tomography. To satisfy this constraint, the ratio of the $B1/B2$ and $E1/E2$ parameters need to be equal in each cell: $E1_k = \kappa B1_k$ and $E2_k = \kappa B2_k$:

$$\delta t_{es}^{Pn} = \Sigma\Delta_{esk}(\delta s_k + B1_k \cos 2\phi_{esk} + B2_k \sin 2\phi_{esk}) + \delta\tau_e^{Pn} + \delta\tau_s^{Pn}$$
$$\delta t_{es}^{Sn} = \Sigma\Delta_{esk}(\delta s_k R_0 + \gamma S_0^P \delta r_k + \kappa B1_k \cos 2\phi_{esk} + \kappa B2_k \sin 2\phi_{esk}) + \delta\tau_e^{Sn} + \delta\tau_s^{Sn}$$

Unfortunately this constraint makes the system more complex, since we we neither know κ nor the anisotropic parameters B1 or B2. To simplify the problem, it seems reasonable to assume that κ is constant for all the cells to avoid adding too many model parameters. For equal P- and S- anisotropy in percent, defined as $[V_{max} - V_{min}]/V_{average}$), κ corresponds to the velocity ratio R. Note that κ equals zero for no azimuthal shear-velocity variations. Observations and laboratory experiments provide guidance for reasonable κ values. Generally, it is not simple to determine the relationship between the amount of P and S anisotropy in rocks [*Levin and Park*, 1998], but P anisotropy is generally observed to be stronger than S anisotropy in the upper mantle, although estimates span a fairly large range [e.g. *Ismail and Mainprice*, 1998; *Babuska and Cara*, 1991]. *Keith and Crampin* [1977] provide elastic tensor components for uppermost mantle material with 6.59% azimuthal anisotropy for horizontally propagating SV polarized waves, and 13% for P-waves. Determining the optimal κ value based on data misfit criteria is complicated by the regularization we apply in our inversions. Checkerboard tests (see below) for inversions with damping show that recovered anisotropy amplitudes are generally underestimated, and this would artificially increase the value of κ. Omitting any damping constraints but keeping Laplacian smoothing, we find the data misfit to be smallest for a Pn to Sn anisotropy ratio of $\sim$1.4.

5.2.4 Data Coverage and Resolution Tests

Azimuthal coverage is key in analyzing anisotropy because only in azimuthally well-sampled regions can anisotropy be distinguished from isotropic anomalies. Figure 5.6 shows the azimuthal ray coverage with pie wedges for both Pn and Sn in 2 by 2 degree cells (this is larger than the 0.25 degree cells used in tomography, but gives enough space

for plotting). Azimuthal coverage is good in the westernmost States and the Basin and Range province. The color scale in Figure 5.6 indicates the ray count. Pn rays sample the model region well except for small areas at the edge of the model. Sn ray coverage is lower east of longitude $110°W$, probably partly because the catalog is not complete and also because of fewer natural sources in this region.

Tests with synthetic data are useful to show which parts of the model structure are resolvable for big problems where it is difficult to compute the generalized inverse. This assumes that the simplified model parametrization adequately describes the real wave propagation. Figure 5.7 shows the output of two checkerboard tests with sinusoidal velocity perturbations with a half wave-length of 2° for Sn ray paths only. The top row is output from synthetic data generated with isotropic perturbations only. We used the same station and event distribution as for the real observations, and let the velocity vary between ±5%. We added normally distributed noise with a standard deviation of 0.9 s to the synthetic picks (the median analyst-assigned error to the Sn picks in the USArray database is 0.87s). In the bottom row the input contains both isotropic and anisotropic perturbations of ±5%, with north-south east-west alternating fast axes in adjacent tiles. These Sn tomography maps from synthetic data show that ray coverage should be good enough, assuming mostly SV energy, to resolve azimuthal velocity dependence in California and Nevada.

Next we show two synthetic tests for the joint Pn-Sn inversion. For the top row in Figure 5.8, we generate data with 5% Pn anisotropy, and ±3% Vp and Vp/Vs perturbations in adjacent 2° cells. We add random noise with 0.5 s standard deviation. For the second example we only use ±3% isotropic Pn-velocity perturbations, to assess the amount of leakage into the other parameters (this will generally depend on the choice of regularization parameters). Pn azimuthal ray coverage is not ideal everywhere, but good enough to resolve the Pn fast directions for a large region. The anisotropy amplitudes are less well recovered outside the Basin and Range province and California. It seems unavoidable to have leakage between the model parameters for reasonable regularization. For purely isotropic input, there is leakage into both the anisotropic and Vp/Vs parameters. Anisotropic leakage is largest at the corner of slow and fast isotropic perturbations, indicating that isotropic anomalies might introduce artificial anisotropy at their edges.

5.3 Results and Discussion

5.3.1 Separate Sn Tomography

We preformed separate Sn tomography mainly to test the viability of the Sn picks. Not including small-scale active source studies, the only other attempt on Sn tomography in the western United States to our knowledge was conducted by *Nolet et al.* [1998]. However, the study was pre-USArray, using only about 3500 Sn picks, which limited the model resolution. Our isotropic Sn velocities are plotted in Figure 5.9a, together with the results from separate Pn tomography for comparison in Figure 5.9b. Generally, the large-scale Sn anomalies are in good agreement with the ones from a purely Pn inversion. This shows that the Sn picks contain useful signal despite their greater scatter.

The largest differences between our Pn and Sn tomography maps are the larger Sn low-velocity anomalies seen beneath the Colorado Plateau and central Wyoming. The shear-velocity map at Moho + 4 km (upper mantle) depth from the ambient noise data of *Bensen et al.* [2009] shows a similar strong low-velocity zone for much of Utah and northern Arizona, without any corresponding low-velocity anomalies at Moho - 4 km (lower crust) depth or at 80 km depth for this region. *Steck et al.* [2011] also measure higher-than-average crustal Sg velocities for the Colorado Plateau. It appears that the jump in shear velocity across the Moho below the Colorado Plateau is relatively small.

Although looking at the fast directions obtained from Sn tomography alone (Figure 5.9c) can help to understand the nature and quality of the Sn picks, interpretations should be made with caution. *Diaz et al.* [2013] performed Sn tomography for the Euro-Mediterranean region and found sharper velocity perturbations with better lateral continuity when anisotropic terms are included in the inversions, even where it appears that Sn anisotropy is badly resolved and the Pn and Sn fast directions generally don't agree (compare Figure 5.9c with 5.9d). Similarly, we find that adding anisotropic parameters to the Sn inversion produces more focused isotropic anomalies.

5.3.2 Joint Tomography Results

Vp and Vp/Vs Structure

The images in Figure 5.10 show the isotropic Pn velocities and Vp/Vs ratio for the three different inversion schemes. The inclusion of anisotropic parameters for Sn does not significantly lower the data variance (Table 5.1). Judging by the tomographic

maps and data fit, there is either no significant shear anisotropy for most regions below the western United States, or the error of the shear-wave picks is too large to resolve the relatively small anisotropic signal, or the assumption of hexagonal symmetry with a horizontal symmetry axis is not valid. Since Pn and surface-wave tomographies show a heterogeneous but similar anisotropic structure below the western United States it is likely that there is too much scatter in the Sn picks to detect anisotropy. Nevertheless, the inclusion of both Pn and Sn anisotropy, with consistent fast directions, sharpens the image. This is our preferred model, not only because of the more focused anomalies, but because it results from an inversion approach that is most consistent with anisotropic observations and aligned olivine models.

One of the most prominent low-velocity anomalies in the uppermost mantle beneath the western United States is located below the Snake River Plain. This anomaly appears to range vertically from the Moho to about ∼200 km depth [*Schmandt and Humphreys*, 2010; *Tian and Zhao*, 2012]. The Vp/Vs in this region is high (∼1.8). These observations are in agreement with a partially molten upper mantle below the Yellowstone hotspot track because the existence of partial melt or fluids in the uppermost mantle should affect the shear-wave velocity more drastically than the compressional velocity [e.g. *Takei*, 2002].

The other two large high Vp/Vs anomalies are situated in central Wyoming and below the bulk of the Colorado Plateau. Since the ray paths that cover Wyoming are mostly from low-magnitude quarry blasts, we will not focus on this structure. The high Vp/Vs anomaly below the Colorado Plateau is interesting as it is in contrast with Pn and other body-wave velocities measured in this region, which are typically lower in the southwest and higher in the northeast [*Obrebski et al.*, 2011; *Schmandt and Humphreys*, 2010]. Comparison of our uppermost mantle Vp/Vs map to the images at 90 km depth by *Schmandt and Humphreys* [2010], which show average to high P and S velocities for most of the Colorado Plateau, suggests significant changes in shear-velocity structure in the top 50 km of the mantle. *Levander et al.* [2011] presented an additional Vp/Vs map at 80 km depth beneath the Colorado Plateau from a similar body-wave tomography study as in *Schmandt and Humphreys* [2010], which shows low shear-wave velocities and high Vp/Vs beneath the periphery of the plateau surrounding a higher-velocity core. They interpret this seismically imaged core as a lithospheric drip, which delaminates from the base of the lower crust of the Colorado Plateau. If the lithospheric drip has

detached completely from the base, and asthenospheric material has taken the space of the removed lithosphere, it would make sense to observe a different seismic structure in the top kilometers of the mantle with generally high Vp/Vs. This argument however is in contrast with the relatively high Pn velocities in the northeastern section below the Colorado Plateau, unless we assume that the lithosphere below this northeasternmost region is intact (in agreement with the sketch by *Levander et al.* [2011]), and that the shear anomaly is somewhat smeared out because of lower ray coverage further east.

Regions with low Vp/Vs anomalies typically are more complicated to explain. Figure 5.10 shows very low Pn velocities and low Vp/Vs below the Sierra Nevada for all the models, but the anomaly appears more pronounced if we account for anisotropy. This low P-velocity anomaly is consistent with the older Pn study by *Hearn* [1996], but appears to be confined to the very top of the mantle below the Sierra Nevada, and tomography slices from *Schmandt and Humphreys* [2010] and *Tian and Zhao* [2012] at 90 km and 65 km depth respectively show high-velocity anomalies associated with the Juan de Fuca slab in this region. *Jones et al.* [1994] suggested that the uppermost mantle below the Sierra Nevada is unusually warm. Studies of xenoliths indicate that mantle lid beneath the Sierra Nevada has been removed since ca. 10 Ma, and seismic analysis suggests that the removed material is descending deeper into the mantle west of the range (e.g., *Saleeby and Foster* [2004]). Upwelling of hot asthenospheric material would explain the very low uppermost mantle Pn velocities. However, the Sn anomaly is much less strong, and the observation of low Vp/Vs is puzzling as higher values would generally be expected in such a regime. A change in composition, such as enrichment in orthopyroxene in the upper mantle [*Soustelle and Tommasi*, 2010] or the presence of pore fluids [*Takei*, 2002] could lead to locally lower Vp/Vs. Since the Farallon Plate subduction beneath the western United States is believed to have experienced a period of flat subduction during the Laramide orogeny, it is interesting to note that these characteristics—low P-velocity and low Vp/Vs—are similar to the recent observations by *Wagner et al.* [2006] for the upper mantle above the flat slab subduction in Chile and Argentina, but differ from seismic properties of subduction zones with steeper slabs.

Anisotropy

Figure 5.11a shows the fast direction we obtain from a Pn-Sn joint inversion that only allows the Pn velocity to vary with azimuth. These Pn anisotropic modeling

results generally show a quite complex image but don't deviate much from our previous results with Pn data alone that are discussed in [*Buehler and Shearer*, 2010]. The main anisotropic features include the SW-NE fast axis in northwestern Nevada, east-west anisotropy off the coast of northern California and Oregon, and mostly fault-parallel fast axes in central California. The fault-parallel fast axis indicates that the anisotropy in this region is caused by shearing along the plate boundary, but similar to *Hearn* [1996] we find that the fast axis is not parallel to the plate boundary in all of southern California, but is east-west in the Mojave Desert. *Hearn* [1996] suggests north-south compression in southern California for the possible cause of the perpendicular east-west anisotropic direction. The strong anisotropy off coastal Oregon could be correlated with the subduction zone. However, large isotropic anomalies can also be observed in this area, which could indicate a modeling artifact since azimuthal coverage in these cells is limited.

Apart from sharpening the Vp/Vs anomalies, the inclusion of Sn anisotropic parameters has overall only minor effects, and the fast directions are mostly constrained by the larger number of Pn data for P to S anisotropy ratios larger than 1. In Figure 5.11b we display the fast directions as obtained from an inversion that includes Sn anisotropy, with a prescribed Pn to Sn anisotropy ratio of 1, which is probably larger than expected, but serves as an end-member for comparison to fast directions from Pn data only. Most notably, the inclusion of Sn requires stronger anisotropy off the western coast. Azimuthal coverage in this region, however, is bad, and Sn tomography shows patches of strong isotropic anomalies that typically are associated with an increase in leakage between model parameters as indicated by the checkerboard tests. In regions where Pn anisotropy is well resolved, such as California and northeastern Nevada, it appears that the inclusion of Sn anisotropy equalizes the anisotropy amplitude.

Crustal Thickness and Vp/Vs Structure

The major part of the signal in the station time terms can be explained with changes in crustal thickness, and a first-order estimate of the Moho depth of the region is easily obtained by assuming a constant crustal velocity. Each thickness measurement represents an average over a cone defined by the ray incident angles and Moho depth. Event time terms are generally not used as they are subject to large error because of often poorly-constrained hypocenter depths. The assumption of constant crustal velocity, however, does not appear very realistic, and recent research confirms that the crustal

velocity in the western United States is very heterogeneous, both laterally and vertically [e.g. *Moschetti et al.*, 2010b; *Steck et al.*, 2011]. With both Pn and Sn time terms it is possible to gain insight into both crustal thickness and vertically averaged crustal velocities [e.g. *Haines*, 1980], although they cannot be interpreted unambiguously without any independent constraints. However, the relationship between crustal thickness and the crustal P- or S-velocity is close to linear, and the crustal Vp/Vs relatively insensitive to small changes in thickness.

Since the Pn and Sn station time terms have zero mean (set as a constraint in the inversion process because of the tradeoff between the station and event terms), we first estimate the time contribution from the average crustal thickness and velocity structure in the region in order to obtain absolute times. We accomplish this by fitting a straight line to time-distance points of shallow continental earthquakes to measure the intercept time for both Pn and Sn data. We then add half of that intercept time to the relative station time terms. The intercept times suggest average crustal P- and S- velocities of 6.07 km/s and 3.48 km/s for an average crustal thickness of 35 km, and 6.39 km/s and 3.68 km/s for a 40 km crust, respectively. Values between these two estimates seem most likely. For comparison, *Chulick and Mooney* [2002] found an average crustal thickness for the North American continent of 36.72 km with average P- and S-velocities of 6.29 km/s and 3.65 km/s. Recent USArray receiver-function studies [*Gilbert*, 2012; *Levander et al.*, 2011; *Lowry and Perez-Gussinye*, 2011] seem to show average crustal thickness values between ∼38-40 km. We proceed with assuming an average crustal thickness of 38.5 km with corresponding mean crustal P- and S-velocities of 6.30 km/s and 3.61 km/s respectively.

Next we calculate crustal thickness separately as inferred from the Pn and Sn time terms, assuming these homogeneous crustal velocities. Figure 5.12a shows the crustal thickness estimates below each receiver (after correcting for station elevations). These Moho depth estimates show a relatively smooth image even though no regularization is applied to the time terms in the tomography. The crust gradually thickens from the southern Basin and Range across the Colorado Plateau to a maximum below the Wyoming Basin and the southern Rocky Mountains. The map also shows thin crust for the central Basin and Range compared to deeper Moho depths below the western mountain ranges. Crustal P-velocity in the western United States is not constant, however, and introduces errors in regions of crustal velocity anomalies. In Figure 5.12b we show the crustal thicknesses inferred from Pn time terms using the laterally-varying vertically-averaged

crustal velocities compiled by *Chulick and Mooney* [2002]. The lower-than-average velocities for most of the western and southern margin reduces the crustal thickness estimates for these regions. On the other hand, the higher crustal velocities below the Great Plains increase the corresponding Moho depths. Note that the low values at the northeastern model boundary are associated with larger errors and don't provide an reliable picture of crustal thickness for this region.

Figure 5.12c shows the inferred crustal thickness with a constant crustal S-velocity of 3.61 km/s. The Sn time terms show larger scatter, but overall exhibit similar features to the Pn station terms. It is not expected that the Pn and Sn maps agree in detail, as it is likely that the Vp/Vs ratio in the crust is not constant. Thus differences in the Pn and Sn thickness maps indicate lateral Vp/Vs variations. It is also important to remember that the Sn terms are generally associated with larger errors, especially east of longitude 110° W, and that the time terms average over azimuth. These factors account for some of the observed differences, especially at stations in the east with few Sn arrivals.

Figure 5.12d shows the crustal Vp/Vs at each station location as inferred from the Pn and Sn time terms, adjusted to absolute times as described above, and using the crustal thickness displayed in Figure5.12b. The ratio spans a fairly large range from ∼1.55 to ∼2.15 with 94% of the model points falling between 1.6 and 1.9. The variations of the Pn and Sn terms indicate higher crustal velocity ratios in the southern Basin and Range Province and southern California. Other regions of high Vp/Vs include the crust of the Columbia Plateau, and much of the Great Basin, especially the section south of the Snake River Plain and west of the Colorado Plateau. We generally observe low values east of the Basin and Range, prominently in the southwest and northeast of the Colorado Plateau. The easternmost tip of the Snake River Plain is associated with low Vp/Vs, but the ratio is generally higher for the central portion.

Crustal thickness estimates from receiver function analysis are based on the difference in arrival times between the direct and converted wave at the crust-mantle boundary and are used to infer both crustal thickness and Vp/Vs. They generally suffer from a velocity-thickness trade-off as well, and comparisons between models can provide additional insight on the most likely Moho depth. *Gilbert* [2012], *Levander et al.* [2011] and *Lowry and Perez-Gussinye* [2011] present crustal thickness estimates from receiver functions at USArray stations with different methods and a priori assumptions. Overall, the crustal thickness estimates from receiver functions and Pn station terms look similar,

but there are discrepancies in some regions.

Generally, our crustal thickness estimates from the Pn time terms are larger than receiver-function results along the western margin. This is especially so if we assume a constant crustal velocity in the time-term analysis, and leads to thickness estimates that are about 10 km thicker than the ones measured using receiver functions by *Gilbert* [2012] below many stations along the coast of California, southern Oregon, and Washington. Using lower crustal velocities in this region, as compiled by *Chulick and Mooney* [2002], produces thinner crust, which largely agrees with the receiver-function thickness estimates of *Lowry and Perez-Gussinye* [2011] along the coast of California and Oregon, but which remain somewhat thicker than those of *Gilbert* [2012]. The thicker crust required to explain the station time terms along the coast of Washington could be a result of complications with the plate boundary since many Pn ray paths are incident from offshore.

For the Basin and Range and Snake River Plain provinces the receiver function and Pn crustal thicknesses are mostly consistent, and show an northward increase in Moho depth. Our thickness below the Snake River Plain ranges from about 32 to 40 km, roughly similar to the values obtained by *Lowry and Perez-Gussinye* [2011]. *Levander et al.* [2011] show a crust about 40 km thick below the Snake River Plain from Ps receiver functions, but only about 35 km thick from Sp receiver functions. The study by *Gilbert* [2012] shows the thickest Snake River Plain crust with Moho depths exceeding 40 km. These higher values for the crustal thickness of the Snake River Plain could result from the assumption of constant Vp/Vs, as the Snake River Plain generally seems to be associated with a higher-than-average ratio, as indicated by *Lowry and Perez-Gussinye* [2011] and, less significantly, by our Vp/Vs map.

All of the above-mentioned studies agree that the Moho below the southern Basin and Range is thin, bordered by the thicker crust of the Colorado Plateau and the Great Plains. However, resolving details of the crustal thickness of the Colorado Plateau has proven as problematic as the velocity structure of the upper mantle, as the Moho depth estimates are generally inconsistent between studies, even though the crust generally appears undeformed and tomographic images show mostly laterally-constant crustal velocities throughout the Plateau [e.g. *Moschetti et al.*, 2010b; *Steck et al.*, 2011]. *Gilbert* [2012] discussed the difficulty of obtaining accurate receiver-function measurements below the Colorado Plateau because of the presence of high-velocity layers in the lower crust,

which decrease the velocity contrast across the Moho. The various crustal thickness studies show some of the biggest differences in this province: *Lowry and Perez-Gussinye* [2011] found consistently thick crust throughout the Plateau exceeding 40 km except for small patches of slightly thinner crust in the center. The Colorado Plateau crust seen by *Gilbert* [2012] generally exceeds ∼42 km but shows greater variability, with very thick crust around 50 km in the southwest and along the northeastern border. We also observe an increase in thickness in the southwestern part of the Plateau, the absolute values however are ∼10 km lower than the estimates by *Gilbert* [2012]. *Levander et al.* [2011] found a thickness of ∼50 km in the north and east of the Plateau thinning to about 35 km at the southern and western boundary. Our Moho depth generally increases towards the northeast as well but is shallower overall.

Our Vp/Vs estimates are generally lower for the Colorado Plateau than the values of *Lowry and Perez-Gussinye* [2011], but the overall structure with lower values at the margin and higher Vp/Vs in the center is similar. Crustal Vp/Vs estimates are often subject to relatively large errors. Differences in Pn and Sn ray paths, crustal anisotropy, and azimuthal averaging, for example, could contribute to errors in Vp/Vs estimates. Waves used for receiver function analysis have almost vertical incidence and therefore optimal lateral resolution. However, they often poorly constrain the Vp/Vs ratio; *Lowry and Perez-Gussinye* [2011] include constraints from gravity to reduce uncertainty. It is therefore not surprising that the Vp/Vs map shows some scatter, and that there are differences between receiver function and time-term estimates. Consistencies include high Vp/Vs in the crust of the Columbia Plateau, Snake River Plain, the center of the Colorado Plateau and the southern Basin and Range, as well as low Vp/Vs near the eastern Sierra Nevada, the margins of the Colorado Plateau, and the crust of the Rocky Mountains. In the northern Basin and Range, we obtain low crustal Vp/Vs for a relatively narrow region in central Nevada, surrounded in the east and west by high ratios. This structure is very different from the Vp/Vs values estimates by *Lowry and Perez-Gussinye* [2011] whose map shows low values in central and eastern Nevada. It is not yet clear what causes these differences, as the crustal thickness in this region appears to be well constrained and no strong velocity anomaly in the uppermost mantle can be observed. Combined analysis of crustal refraction data, as explored with USArray data by *Steck et al.* [2011], might provide further insight.

5.4 Conclusions

USArray has greatly improved regional data coverage, and despite a very heterogeneous uppermost mantle there is enough quality Sn data to image isotropic Vp/Vs structure in the mantle lid. However, the Sn waveforms are often highly attenuated and emergent and incoherent between stations, which makes accurate picking on two components very difficult. In California, where data coverage generally is best, we found 2θ azimuthal variations for both Sn-SH and Sn-SV which we can't convincingly explain. Nevertheless, we favor a joint inversion that includes anisotropic parameters for both Sn and Pn, with fast axes in the same direction as expected for a hexagonally symmetric material with horizontal symmetry axis. Such an inversion seems to sharpen the isotropic anomalies compared to an isotropic tomography. We identify large fast Vp/Vs anomalies below the Snake River Plain and the Colorado Plateau. Comparing our results to other studies, we find the Snake River Plain anomaly appears consistently from the Moho to depths of about 200 km, whereas the mantle lithosphere below the Colorado Plateau seems to be very heterogeneous. The very low Pn velocities below the Sierra Nevada coincide with a low Vp/Vs anomaly, and can possibly be explained with compositional changes. The Moho depth estimates generally agree with crustal thickness studies from receiver functions, although we find a shallower Moho below the Colorado Plateau.

Acknowledgments

Many thanks to Luciana Astiz for helping with the Antelope system, and the ANF seismic analysts and staff for providing the data. Chapter 5, in full, has been submitted for publication in Journal of Geophysical Research: Buehler, J. S. and P. M. Shearer, Anisotropy and Vp/Vs in the uppermost mantle beneath the western United States from joint analysis of Pn and Sn phases, Journal of Geophysical Research, submitted, 2013. The dissertation author was the primary investigator and author of this paper.

References

Babuska, V., and M. Cara (1991), *Seismic anisotropy in the Earth*, vol. 10, Springer.

Backus, G. E. (1965), Possible forms of seismic anisotropy of the uppermost mantle under oceans, *J. Geophys. Res.*, *70*(14), 3429–3439.

Bakir, A., and R. Nowack (2012), Modeling Seismic Attributes of Pn Waves using the Spectral-Element Method, *Pure and Applied Geophysics*, *169*(9), 1539–1556–.

Bath, M. (1978), An analysis of the time term method in refraction seismology, *Tectonophysics*, *51*(3–4), 155–169.

Beghoul, N., M. Barazangi, and B. L. Isacks (1993), Lithospheric structure of Tibet and western North America: Mechanisms of uplift and a comparative study, *J. Geophys. Res.*, *98*(B2), 1997–2016.

Bensen, G., M. Ritzwoller, and Y. Yang (2009), A 3D shear velocity model of the crust and uppermost mantle beneath the United States from ambient seismic noise, *Geophysical Journal International*, *177*(3), 1177–1196.

Buehler, J. S., and P. M. Shearer (2010), Pn tomography of the western United States using USArray, *J. Geophys. Res.*, *115*(B9), B09,315–.

Buehler, J. S., and P. M. Shearer (2012), Localized imaging of the uppermost mantle with USArray Pn data, *J. Geophys. Res.*, *117*(B9), B09,305–.

Christensen, N. I. (1984), The magnitude, symmetry and origin of upper mantle anisotropy based on fabric analyses of ultramafic tectonites, *Geophysical Journal Of The Royal Astronomical Society*, *76*(1), 89–111.

Chulick, G. S., and W. D. Mooney (2002), Seismic Structure of the Crust and Uppermost Mantle of North America and Adjacent Oceanic Basins: A Synthesis, *Bulletin of the Seismological Society of America*, *92*(6), 2478–2492, doi:10.1785/0120010188.

Conder, J. A., and D. A. Wiens (2006), Seismic structure beneath the Tonga arc and Lau back-arc basin determined from joint Vp, Vp/Vs tomography, *Geochemistry Geophysics Geosystems*, *7*, Q03,018, doi:10.1029/2005GC001113.

Crampin, S. (1981), A review of wave motion in anisotropic and cracked elastic-media, *Wave motion*, *3*(4), 343–391.

Diaz, J., A. Gil, and J. Gallart (2013), Uppermost mantle seismic velocity and anisotropy in the Euro-Mediterranean region from Pn and Sn tomography, *Geophysical Journal International*, *192*(1), 310–325, doi:10.1093/gji/ggs016.

Gilbert, H. (2012), Crustal structure and signatures of recent tectonism as influenced by ancient terranes in the western United States, *Geosphere*, *8*(1), 141–157.

Goes, S., R. Govers, and P. Vacher (2000), Shallow mantle temperatures under Europe from P and S wave tomography, *J. Geophys. Res.*, *105*(B5), 11,153–11,169.

Haines, A. (1980), Differences in time terms between new zealand seismograph stations and implications for crustal structure, *New Zealand Journal of Geology and Geophysics*, *23*(5-6), 541–549.

Hearn, T. M. (1996), Anisotropic Pn tomography in the western United States, *Journal Of Geophysical Research-Solid Earth*, *101*(B4), 8403–8414.

Ismail, W. B., and D. Mainprice (1998), An olivine fabric database: an overview of upper mantle fabrics and seismic anisotropy, *Tectonophysics*, *296*(1–2), 145–157.

Jones, C. H., H. Kanamori, and S. W. Roecker (1994), Missing roots and mantle and drips: Regional Pn and teleseismic arrival times in the southern Sierra Nevada and vicinity, California, *J. Geophys. Res.*, *99*(B3), 4567–4601.

Jurkevics, A. (1988), Polarization analysis of three-component array data, *Bulletin of the Seismological Society of America*, *78*(5), 1725–1743.

Keith, C. M., and S. Crampin (1977), Seismic body waves in anisotropic media: synthetic seismograms, *Geophysical Journal of the Royal Astronomical Society*, *49*(1), 225–243.

Langston, C. A. (1982), Aspects of Pn and Pg propagation at regional distances, *Bulletin of the Seismological Society of America*, *72*(2), 457–471.

Levander, A., B. Schmandt, M. S. Miller, K. Liu, K. E. Karlstrom, R. S. Crow, C.-T. A. Lee, and E. D. Humphreys (2011), Continuing Colorado plateau uplift by delamination-style convective lithospheric downwelling, *Nature*, *472*(7344), 461–465.

Levin, V., and J. Park (1998), P-SH Conversions in Layered Media with Hexagonally Symmetric Anisotropy: A CookBook, in *Pageoph Topical Volumes*, edited by J. Plomerova, R. Liebermann, and V. Babuska, pp. 669–697–, Birkhaeuser Basel.

Lin, F.-C., and M. H. Ritzwoller (2011), Helmholtz surface wave tomography for isotropic and azimuthally anisotropic structure, *Geophysical Journal International*, *186*(3), 1104–1120.

Lin, F.-C., M. H. Ritzwoller, Y. Yang, M. P. Moschetti, and M. J. Fouch (2011), Complex and variable crustal and uppermost mantle seismic anisotropy in the western United States, *Nature Geosci*, *4*(1), 55–61.

Liu, K. H. (2009), NA-SWS-1.1: A uniform database of teleseismic shear wave splitting measurements for North America, *Geochem. Geophys. Geosyst.*, *10*.

Long, M. D., and T. W. Becker (2010), Mantle dynamics and seismic anisotropy, *Earth and Planetary Science Letters*, *297*(334), 341–354.

Lowry, A. R., and M. Perez-Gussinye (2011), The role of crustal quartz in controlling cordilleran deformation, *Nature*, *471*(7338), 353–357.

Maupin, V., and J. Park (2007), Theory and observations–wave propagation in anisotropic media, *Seismology and the Structure of the Earth. Treatise on Geophysics*, *1*, 289–321.

Moschetti, M. P., M. H. Ritzwoller, F. Lin, and Y. Yang (2010a), Seismic evidence for widespread western-US deep-crustal deformation caused by extension, *Nature*, *464*(7290), 885–889.

Moschetti, M. P., M. H. Ritzwoller, F.-C. Lin, and Y. Yang (2010b), Crustal shear wave velocity structure of the western united states inferred from ambient seismic noise and earthquake data, *J. Geophys. Res.*, *115*(B10), B10,306–.

Nolet, G., C. Coutlee, and R. Clouser (1998), Sn velocities in western and eastern North America, *Geophys. Res. Lett.*, *25*(10), 1557–1560.

Obrebski, M., R. M. Allen, F. Pollitz, and S.-H. Hung (2011), Lithosphere-asthenosphere interaction beneath the western United States from the joint inversion of body-wave traveltimes and surface-wave phase velocities, *Geophysical Journal International*, *185*(2), 1003–1021.

Park, J., and V. Levin (2002), Seismic Anisotropy: Tracing Plate Dynamics in the Mantle, *Science*, *296*(5567), 485–489, doi:10.1126/science.1067319.

Perry, H. K. C., C. Jaupart, J. . C. Mareschal, and N. M. Shapiro (2006), Upper mantle velocity-temperature conversion and composition determined from seismic refraction and heat flow, *Journal of Geophysical Research-Part B-Solid Earth*, p. 14 pp.

Raitt, R. W., G. G. Shor, T. J. G. Francis, and G. B. Morris (1969), Anisotropy of Pacific upper mantle, *Journal Of Geophysical Research*, *74*(12), 3095–&.

Ritzwoller, M., G. Masters, and F. Gilbert (1988), Constraining aspherical structure with low-degree interaction coefficients: Application to uncoupled multiplets, *J. Geophys. Res.*, *93*(B6), 6369–6396.

Ritzwoller, M. H., F.-C. Lin, and W. Shen (2011), Ambient noise tomography with a large seismic array, *Comptes Rendus Geoscience*, *343*(8-9), 558–570.

Roth, J. B., M. J. Fouch, D. E. James, and R. W. Carlson (2008), Three-dimensional seismic velocity structure of the northwestern United States, *Geophysical Research Letters*, *35*(15).

Saleeby, J., and Z. Foster (2004), Topographic response to mantle lithosphere removal in the southern Sierra Nevada region, California, *Geology*, *32*(3), 245–248.

Savage, M. K., and P. G. Silver (1993), Mantle deformation and tectonics: constraints from seismic anisotropy in the western United States, *Physics of the Earth and Planetary Interiors*, *78*(334), 207–227.

Schmandt, B., and E. Humphreys (2010), Complex subduction and small-scale convection revealed by body-wave tomography of the western United States upper mantle, *Earth and Planetary Science Letters*, *297*(334), 435–445.

Shearer, P., and J. Orcutt (1986), Compressional and shear wave anisotropy in the oceanic lithosphere-the Ngendei seismic refraction experiment, *Geophysical Journal International*, *87*(3), 967–1003.

Shen, W., M. H. Ritzwoller, and V. Schulte-Pelkum (2013), A 3-D model of the crust and uppermost mantle beneath the Central and Western US by joint inversion of receiver functions and surface wave dispersion, *J. Geophys. Res. Solid Earth*, *118*(1), 262–276.

Soustelle, V., and A. Tommasi (2010), Seismic properties of the supra-subduction mantle: Constraints from peridotite xenoliths from the Avacha volcano, southern Kamchatka, *Geophys. Res. Lett.*, *37*(13), L13,307–.

Steck, L. K., M. L. Begnaud, S. Phillips, and R. Stead (2011), Tomography of crustal P and S travel times across the western United States, *J. Geophys. Res.*, *116*(B11), B11,304–.

Takei, Y. (2002), Effect of pore geometry on VP/VS: From equilibrium geometry to crack, *J.-Geophys.-Res.*, *107*(B2), ECV 6–1–ECV 6–12.

Tape, C., A. Plesch, J. H. Shaw, and H. Gilbert (2012), Estimating a Continuous Moho Surface for the California Unified Velocity Model, *Seismological Research Letters*, *83*(4), 728–735, doi:10.1785/0220110118.

Thurber, C. (1993), Local earthquake tomography: velocities and Vp/Vs-theory, in *Seismic Tomography: Theory and practice*, edited by H. Iyer and K. Hirahara, pp. 563–583, Chapman and Hall, London.

Tian, Y., and D. Zhao (2012), P-wave tomography of the western united states: Insight into the yellowstone hotspot and the juan de fuca slab, *Physics of the Earth and Planetary Interiors*, *200–201*(0), 72–84.

Tryggvason, A. e. a. (2002), Three-dimensional imaging of the P- and S-wave velocity structure and earthquake locations beneath Southwest Iceland, *Geophysical Journal International*, *151*(3), 848–866.

Wagner, L. S., S. Beck, G. Zandt, and M. N. Ducea (2006), Depleted lithosphere, cold, trapped asthenosphere, and frozen melt puddles above the flat slab in central Chile and Argentina, *Earth and Planetary Science Letters*, *245*(12), 289–301.

West, J. D., M. J. Fouch, J. B. Roth, and L. T. Elkins-Tanton (2009), Vertical mantle flow associated with a lithospheric drip beneath the Great Basin, *Nature Geoscience*, *2*(6), 439–444.

Zhang, H., and C. H. Thurber (2003), Double-Difference Tomography: The Method and Its Application to the Hayward Fault, California, *Bulletin of the Seismological Society of America*, *93*(5), 1875–1889, doi:10.1785/0120020190.

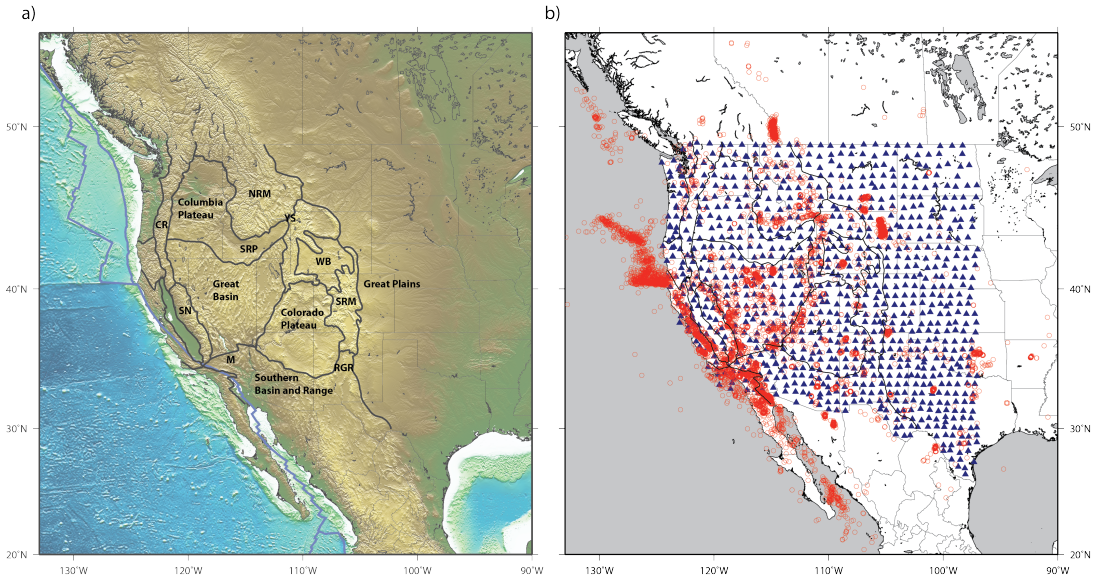

Figure 5.1: a) Overview map of study region with physiographical provinces indicated by black lines and names. The abbreviations are in place for the Cascade Range (CR), Sierra Nevada (SN), Mojave (M), Snake River Plain. (SRP), Northern Rocky Mountains (NRM), Yellow Stone (YS), Wyoming Basin (WB), Southern Rocky Mountains (SRM), and Rio Grande Rift (RGR). b) USArray transportable array stations (blue triangles) and events (red crosses) used in this study.

Table 5.1: Root mean squared errors for the various models.

	RMSE [s]	
fitting method	*Pn*	*Sn*
straight line fit	1.49	2.46
1D time term	0.67	0.91
2D isotropic standalone Sn		0.84
2D anisotropic standalone Sn		0.81
2D anisotropic standalone Pn	0.57	
2D isotropic joint	0.60	0.84
2D joint, with Pn anisotropy only	0.57	0.84
2D joint, with equal Pn and Sn anisotropy	0.57	0.82
2D joint, with Pn/Sn anisotropy = 2	0.57	0.83
mean (median) analyst assigned picking error [s]	0.54 (0.42)	1.10 (0.87)

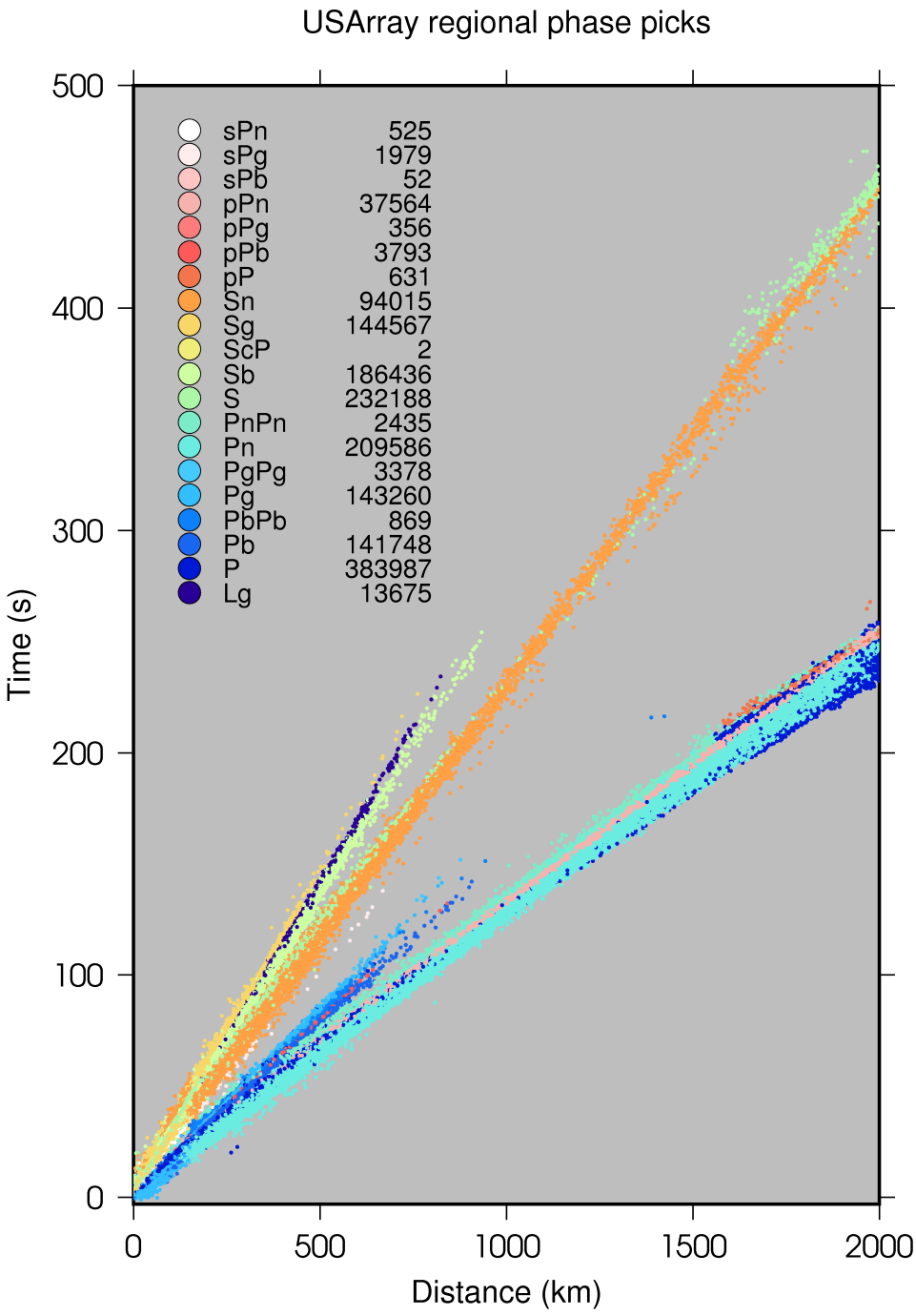

Figure 5.2: Regional phase picks in the USArray data set recorded at stations with longitude >97°W between April 2004 and June 2010. Number of picks according to the ANF tables is listed.

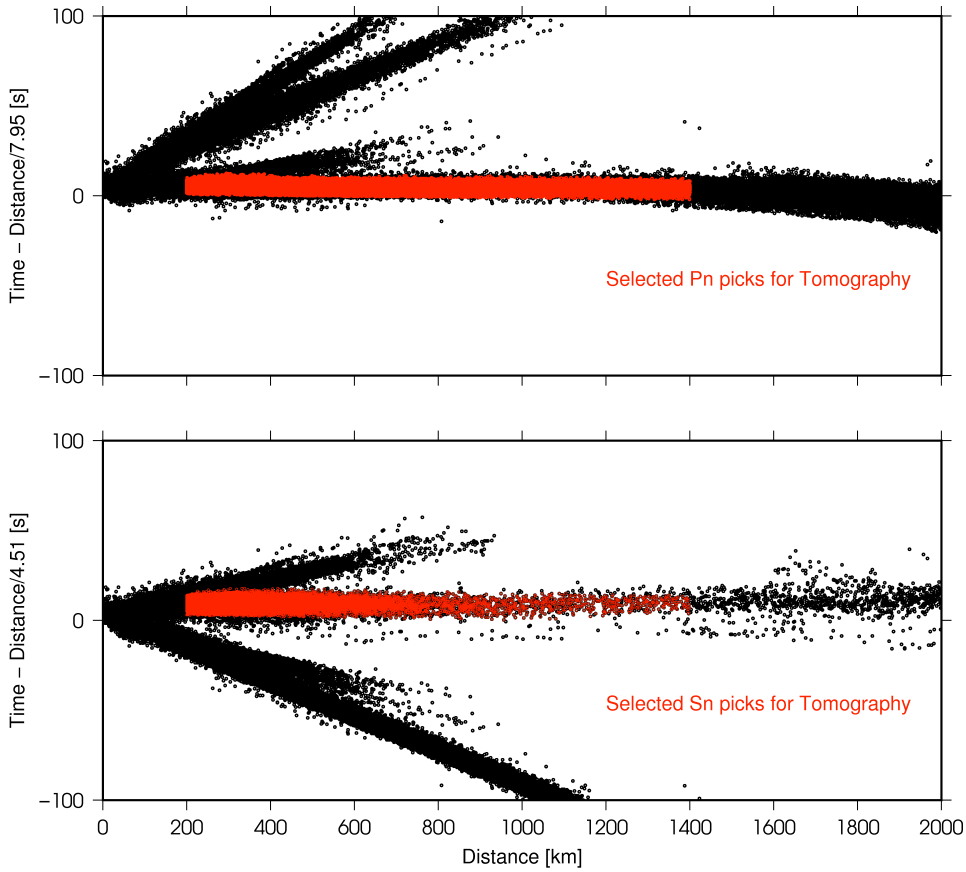

Figure 5.3: Time-distance plots of the regional arrival time picks and our windowed Pn (top) and Sn(bottom) picks that we are using in the tomography.

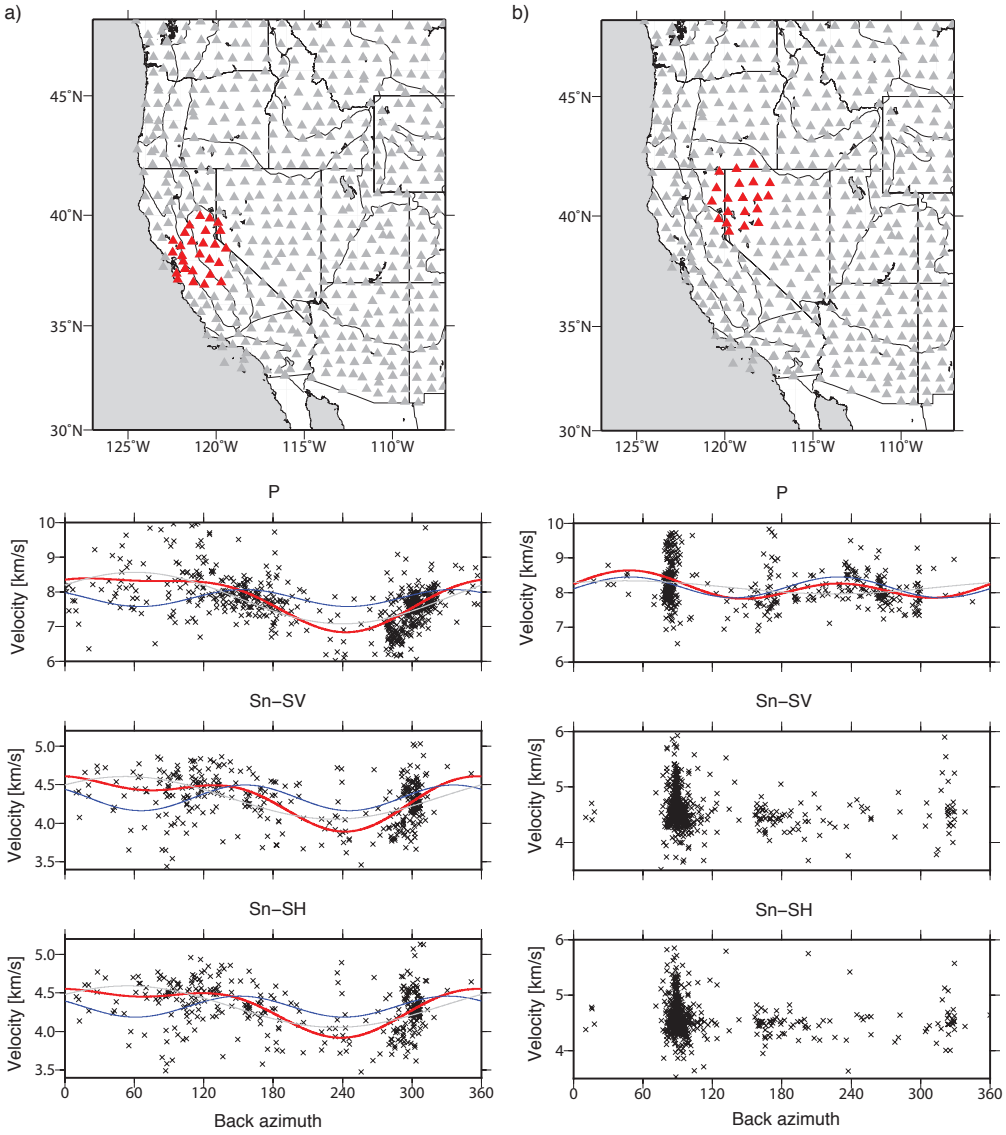

Figure 5.4: Azimuthal velocity variations for two regions for P, Sn-SV, and Sn-SH as measured at the stations indicated in red. a) An example were we observe similar azimuthal variations for both Sn-SH and Sn-SV. b) Velocity measurements for this sub-array are scattered, indicating that the Sn amplitude in this region is too weak for good inter-station cross-correlations, and no pattern is visible. The measurements are fitted with a curve, $Vapp = A + [B\sin\phi + C\cos\phi] + [D\sin 2\phi + E\cos 2\phi]$, shown in red. The 1ϕ contribution that accounts for Moho dip is shown in grey, and the 2ϕ signal accounting for azimuthal anisotropy is shown in blue.

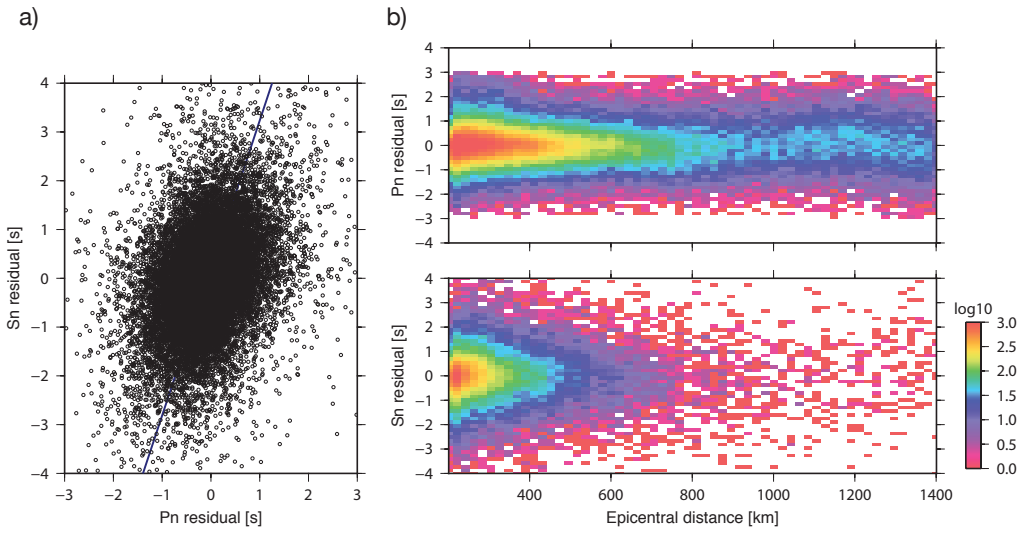

Figure 5.5: a) Pn and Sn residual plot for common station and events. The line from a total least squares fit has a slope of 3.02 with a standard deviation of 0.07 from bootstrap re-sampling. b) Pn (top) and Sn (bottom) residual density plot, showing the residual count in 0.1 s x 20 km intervals.

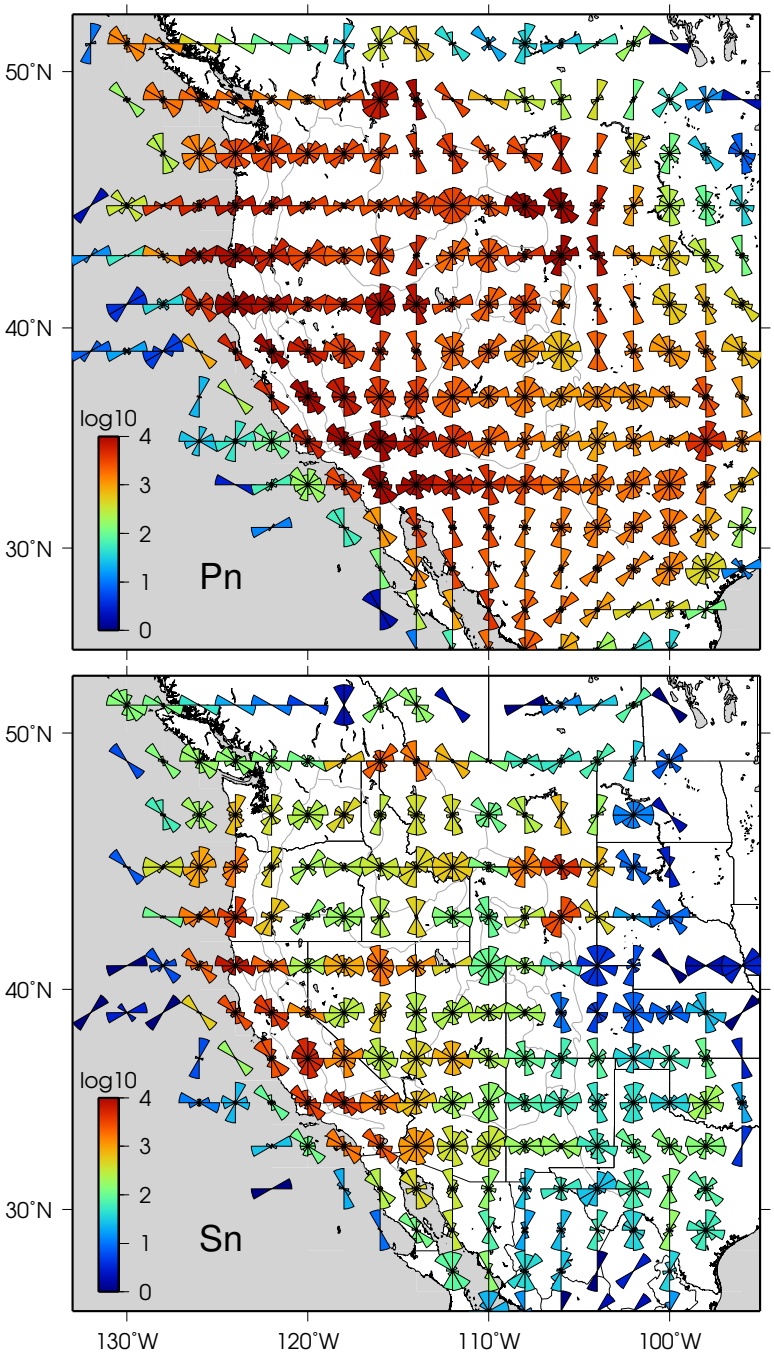

Figure 5.6: Azimuthal coverage for Pn (top) and Sn (bottom) displayed with pie wedges. The color scale shows the ray count.

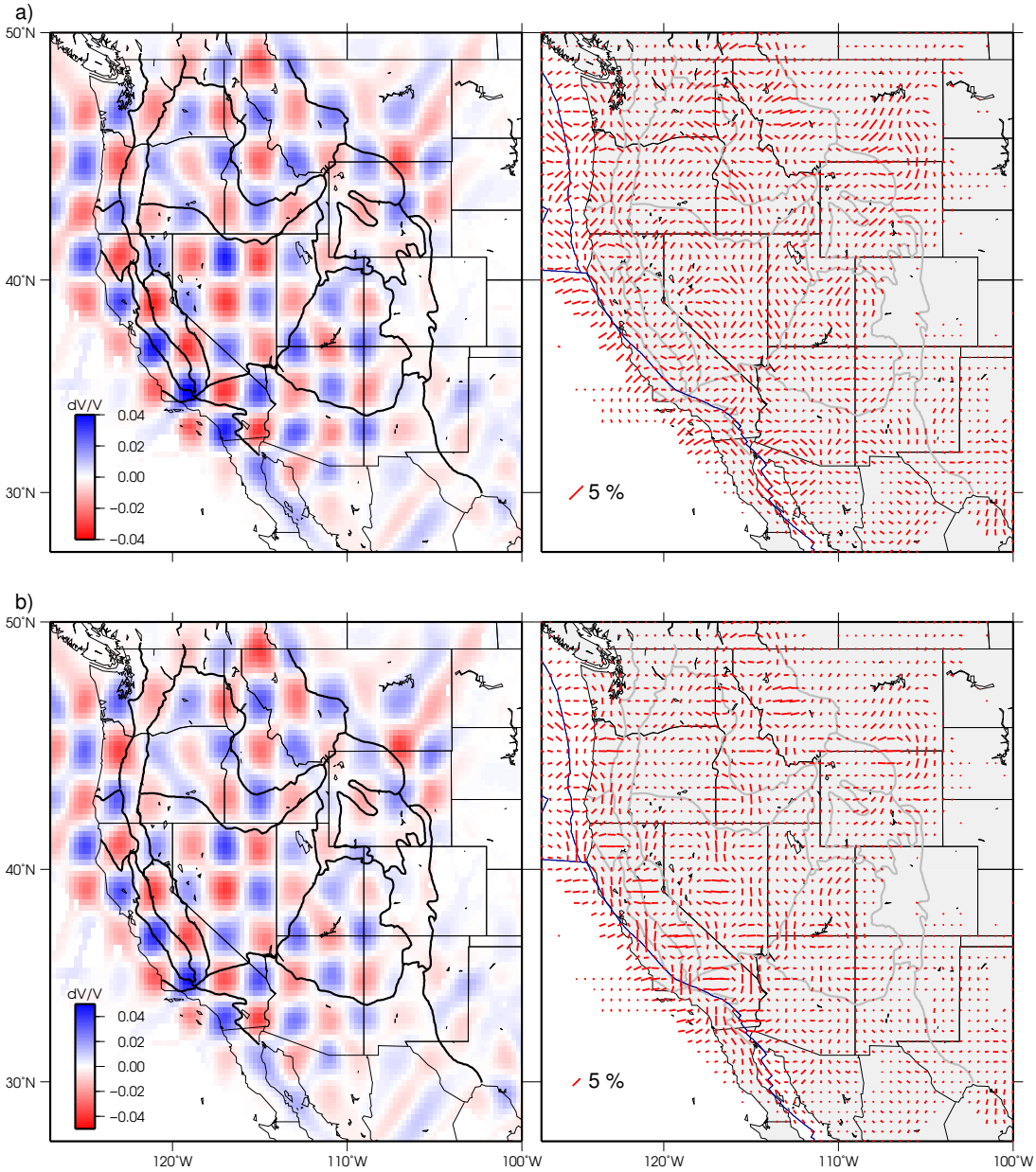

Figure 5.7: Synthetic checkerboard test with Sn data only. a) The recovered models from a test with ±5% isotropic perturbations only. b) Recovered maps from a test that includes both isotropic and anisotropic perturbations.

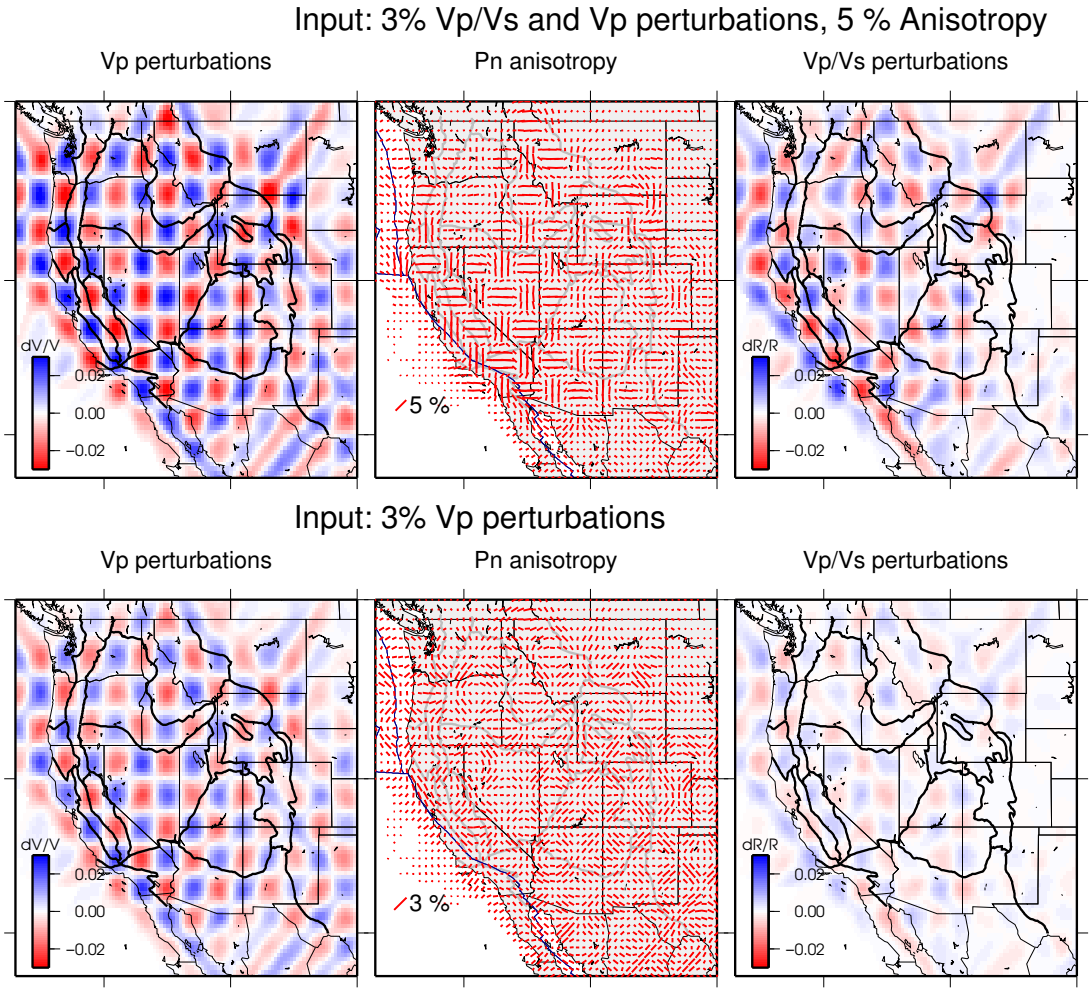

Figure 5.8: Checkerboard tests for the joint inversion. The top row shows recovered models from synthetic data with 5% Pn anisotropy, and ±3% Vp and Vp/Vs perturbations in adjacent 2^o cells. Random noise with 0.5 s standard deviation was added. In the bottom row we used only ±3% isotropic P-velocity perturbations, to assess the amount of leakage into the other parameters.

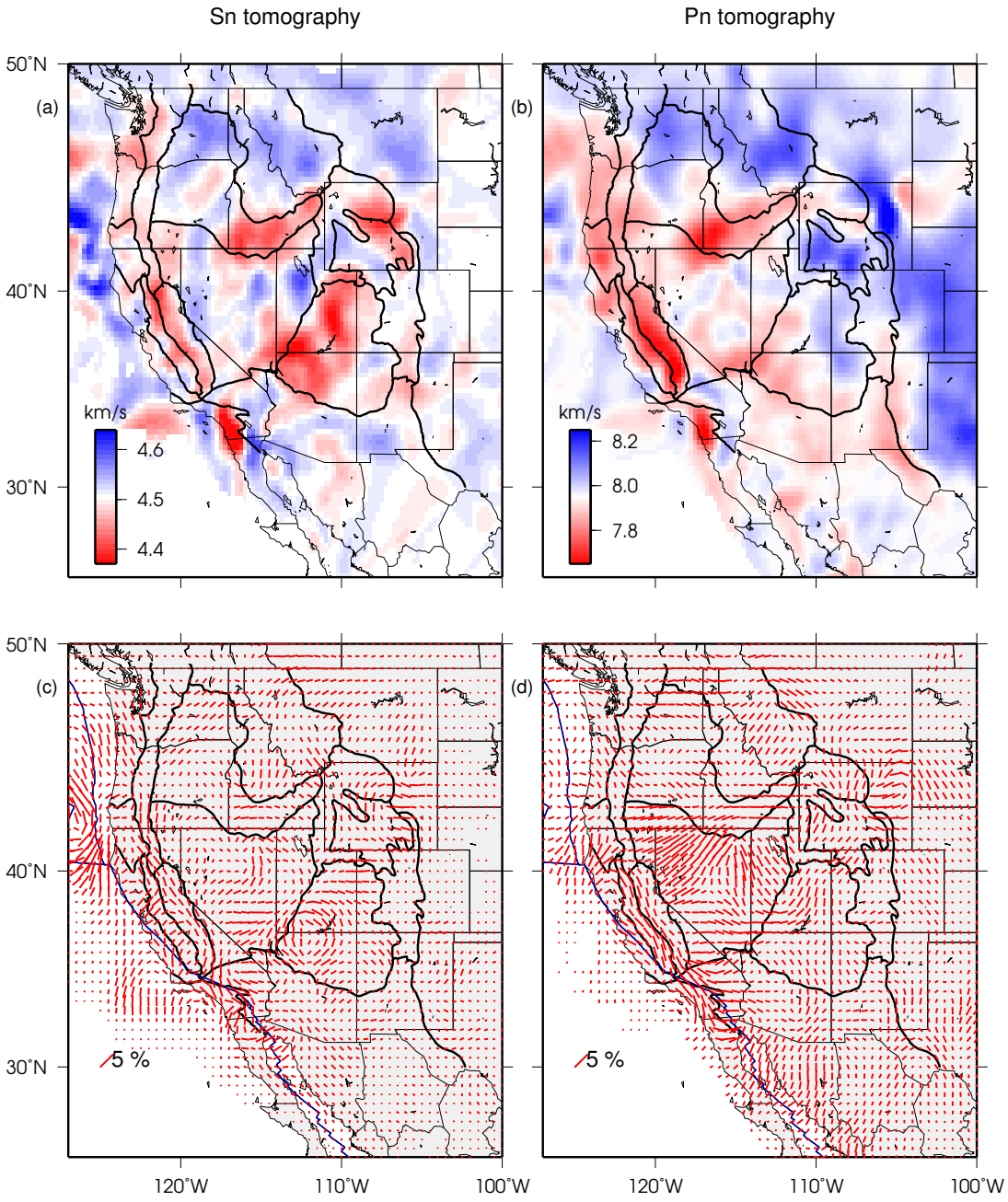

Figure 5.9: Comparison of tomography results for separate anisotropic Sn (left column) and Pn (right column) inversions. a) Shows the retrieved isotropic Sn velocities, and c) the corresponding fast directions. b) and d) show the equivalent maps for Pn.

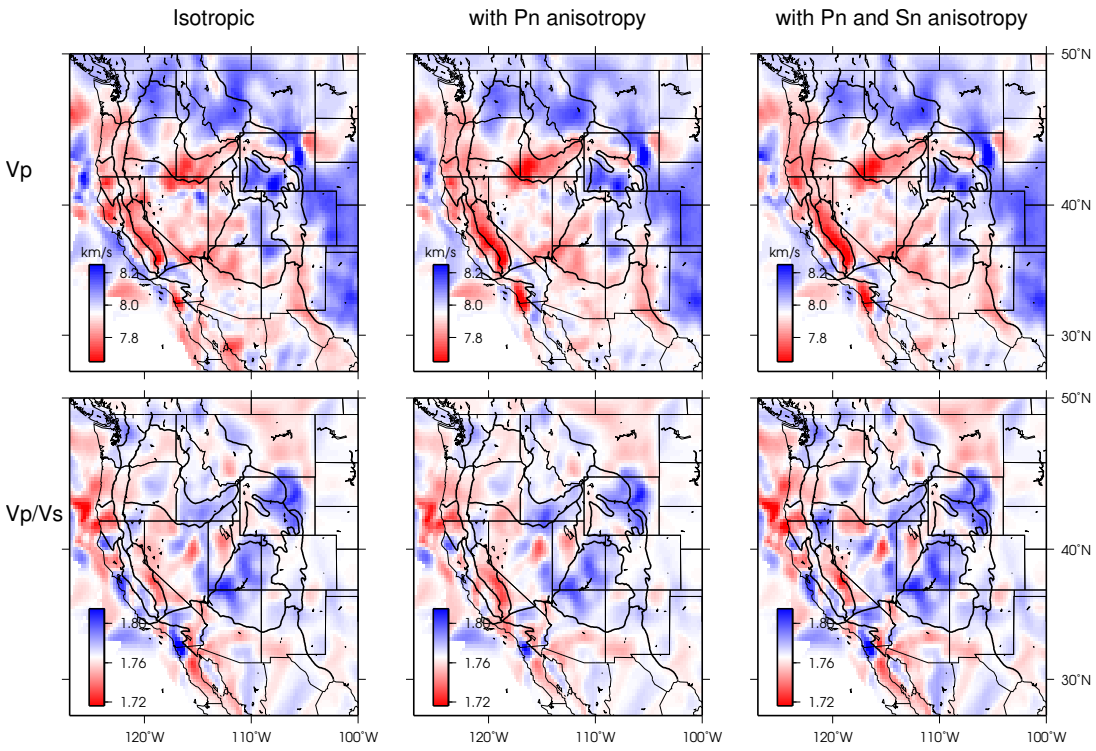

Figure 5.10: Vp and Vp/Vs from joint Pn-Sn tomography. The model in the leftmost column contains no anisotropic parameters. Pn anisotropy is added in the center, and the model on the right contains both Pn and Sn anisotropy of equal magnitude.

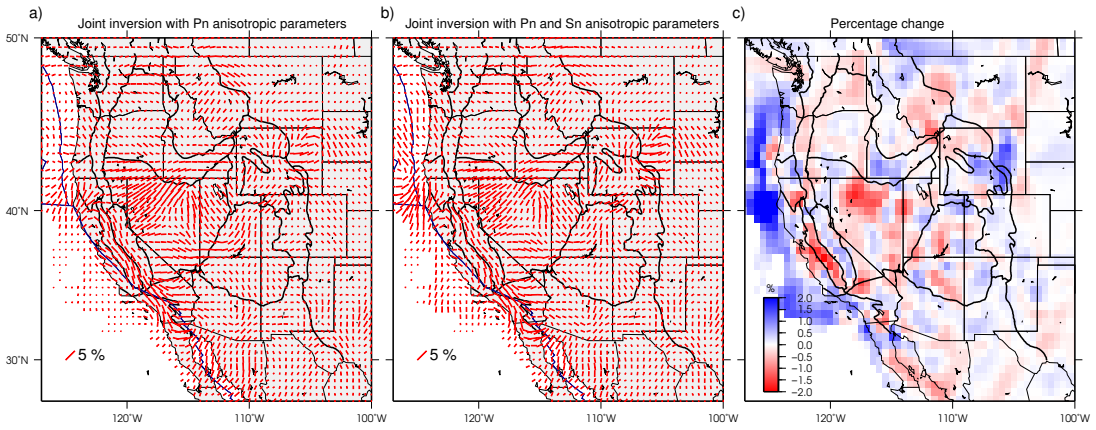

Figure 5.11: Fast axis obtained from a) an inversion that only accounts for Pn anisotropy, and b) from an inversion that includes Sn anisotropy with equal strength. c) Shows the change in percentage between a) and b).

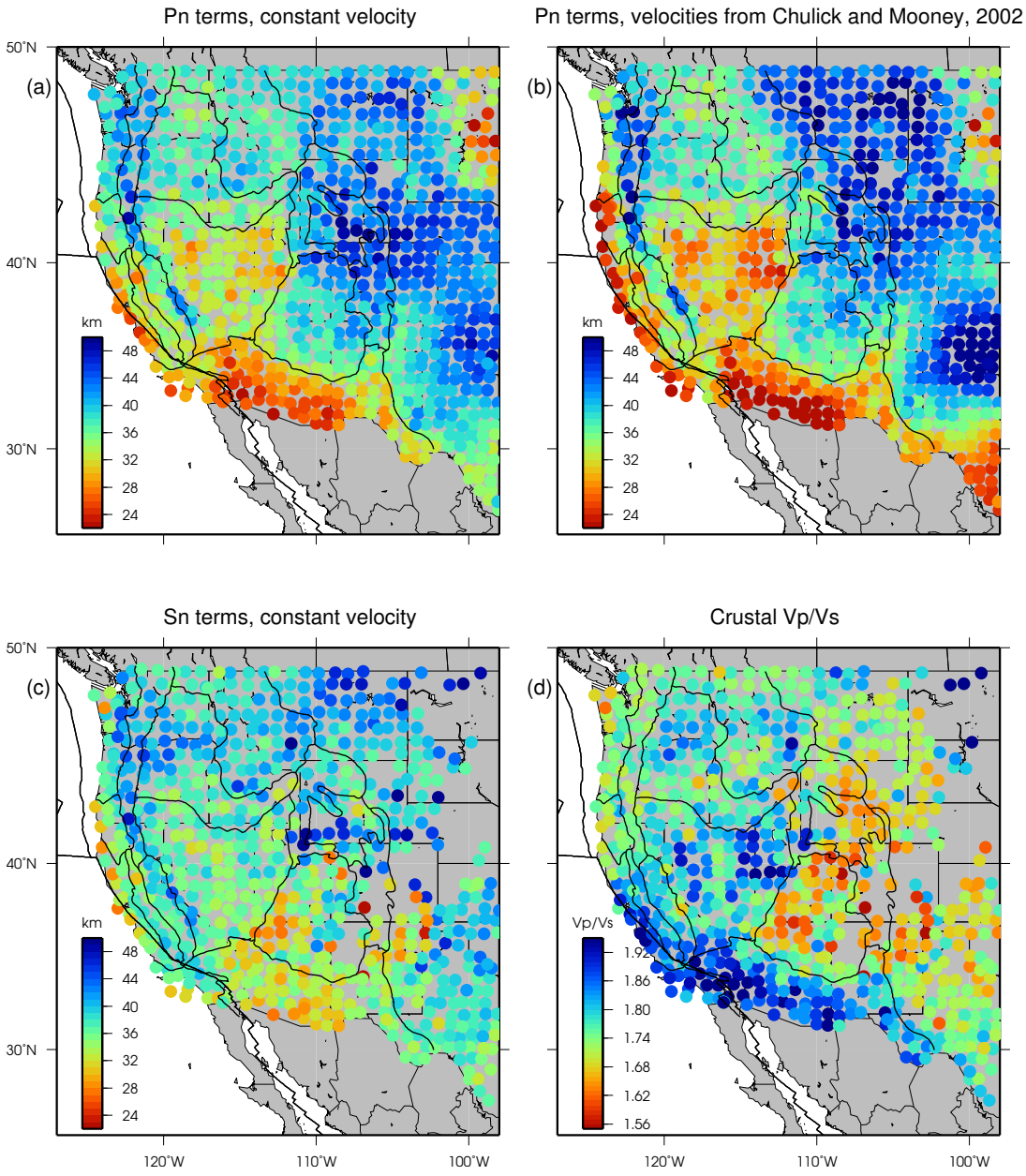

Figure 5.12: Crustal thickness and Vp/Vs estimates from Pn and Sn station time terms. a) Crustal thickness estimates from Pn station terms with the assumption of a constant crustal velocity. b) Same as a), but with lateral varying crustal P-velocities from *Chulick and Mooney* [2002]. c) Crustal thickness estimates from Sn terms with a constant crustal S-velocity. d) Vertically averaged crustal Vp/Vs from Pn and Sn time terms.